

Multicellular Agent-Based Models of Angiogenesis Evaluate Endothelial Cell Signaling and  
the Role of Pericytes in Vascular Network Patterning

---

A Dissertation

Presented to  
the faculty of the School of Engineering and Applied Science  
University of Virginia

---

in partial fulfillment  
of the requirements for the degree

Doctor of Philosophy

by

Joseph Walpole

May

2015

APPROVAL SHEET

The dissertation  
is submitted in partial fulfillment of the requirements  
for the degree of  
Doctor of Philosophy

**Joseph Walpole**

---

AUTHOR

The dissertation has been read and approved by the examining committee:

**Shayn Peirce-Cottler**

---

Advisor

**Kevin Janes**

---

**Feilim Mac Gabhann**

---

**Coleen McNamara**

---

**Jason Papin**

---

Accepted for the School of Engineering and Applied Science:



Dean, School of Engineering and Applied Science

May  
2015

# DEDICATION

The road to a PhD is paved with failure.

You could have said that to me when I was applying to graduate schools and I most certainly would not have understood what it meant. In my mind, failure was what happened when you did something *wrong*. The struggle to get past this narrow thought process was probably the most challenging task ever set before me as student. Every failed experiment, every erroneous hypothesis, every bit of red ink on a manuscript revision – these are not things that were done *wrong*, they are the learning experiences that teach us something new and allow us to grow.

Shayn – this is the greatest thing you have taught me. Both by example and by flat out telling me to my face, you taught me that fearing failure was the only way to actually go wrong. Fear of failure stifled my curiosity, pinned me in place, and caused me to stagnate in self-doubt while I searched for a “correct” answer that did not actually exist. You took me, with care and patience, from my greatest disappointments to where I am now – proud and thrilled to be a scientist. Not least of all, you have been a true friend. We have shared laughs and spent countless hours discussing everything *BUT* science. I don’t know how many half hour meetings turned into three-hour summits, but I do know that both of our planners would be more accurate if we multiplied scheduled meeting times by a factor of six. Thank you for your guidance, friendship, and ceaseless encouragement.

Assisting Shayn to guide me down this winding road was a fantastic advising committee that has challenged me to grow as a scientific investigator. Jason, your ability to ask the obvious question that no one else thought to ask has always impressed me, and your levity amid even the most serious scientific debate is a truly enviable trait. Kevin, your words of advice – to treat hypotheses as a series of columns I should try to topple rather than reinforce – have stuck with me since the thesis proposal. Feilim, you have been a mentor, a friend, and now a committee member; in all these roles you have inspired me to try harder and strive for excellence. Coleen, you have endured my obsession with computational methods and kept me grounded in the physiology that is the *actual* reason why we study biology in the first place. You have all been invaluable, and I sincerely thank you for believing in me.

Unofficially, my friends, colleagues, and collaborators from Chapel Hill have mentored me and helped to get my first real project off the ground. Vicki and John, without your help I’m not sure where I would be today. Also, thanks for inviting me to the cool kids table while we were at NAVBO.

In the trenches alongside me were my friends and fellow graduate students. Members of the Peirce lab, past and present, were always willing to lend a hand or assist with an experiment. Scott, Kyle, Molly, Bruce, Bryan, and Jason – you all had a hand in my success and I can only hope that I have reciprocated. Anthony, our lab manager and second-in-command, you kept the ship afloat despite all our best efforts to try and sink her. And my MSTP colleagues, especially Dave and Jim, I’m glad that no matter where we are (BBQ, brewery, beach, camping, etc.) we can spontaneously start a scientific debate (much to the chagrin of our wives).

My family still doesn’t know exactly what it is that I do, but that has never stopped them from telling me how proud they are of everything I’ve done. They don’t need to know the details of my experiments to hear the disappointment or excitement in my voice. They have supported my dreams and enabled me to go down a truly privileged path. Perhaps the best way to thank them is an assurance: don’t worry; one day I’ll get a real job.

To my wife, Alexis, who will wish that I just referred to her as “Lex” because she doesn’t like when I introduce her as “Alexis” – thank you for, well, *everything else*. You uprooted your life for me to pursue graduate school, following me to Charlottesville before we were even engaged. You have kept me sane despite my best efforts to the contrary. From proofreading my work to quizzing me before exams, you have always encouraged me to succeed. Thank you for being bright, strong, courageous, and confident all those times when I couldn’t be. Also, thank you for kicking me in the shin when I’ve been talking too much and should really wrap things up.

The road to a PhD is paved with opportunity.

# ABSTRACT

Angiogenesis – the formation of new capillary vessels from a preexisting microvascular network – is a concerted cellular process driven by endothelial cell proliferation and migration. Chemotactic cues through the vascular endothelial growth factor (VEGF) pathway combined with intercellular signaling via Notch1-DLL4 are a canonical driving force behind this patterning process. Despite having identified these two fundamental signaling pathways in angiogenesis, we do not yet understand how these signals propagate through multicellular networks and ultimately give rise to geometric pattern diversity. Further, even less is known about the interplay between pericytes, the support cells that enwrap all capillaries, and endothelial cells during angiogenesis. Despite playing a pivotal role in capillary health, we still do not know the extent to which pericytes modulate endothelial cell behaviors or interface with VEGF and Notch1 signaling in vascular networks.

This body of work addresses these questions sequentially through a bottom-up computational modeling approach in combination with *in vitro* and *in vivo* experimental assays. Using agent-based models (ABMs), I have demonstrated that the Notch1-DLL4 signaling axis combined with VEGF receptor binding is sufficient to accurately predict the frequency and location of angiogenic endothelial sprouting events. This computational modeling approach is novel in its use of time course imaging to inform initial simulated endothelial cell positions and locations of subsequent sprouting events. By comparing experimental outcomes with predictions made by the ABM, I was able to directly and independently determine the accuracy of the ABM in predicting the number of capillary sprouting events and their locations during angiogenesis in an embryoid body tissue culture environment.

As an extension of this work, I developed a second ABM of retinal angiogenesis that incorporates pericytes while maintaining endothelial intercellular signaling through Notch1-DLL4 and chemotactic cuing through VEGF receptor binding. Through quantitative analysis of geometric network

properties compared to those of the mouse retinal vasculature, I demonstrated that simulated retinal vascular networks with pericytes produced more physiologically accurate geometries than those generated with endothelial cells alone. Further, these simulations suggested that pericytes act as buffers to endothelial signaling and, as a result, significantly affect vascular network geometries in the developing retina, a novel mechanistic hypothesis that warrants additional experimental investigation.

Through the combined use of ABM and experimental assays of angiogenesis, I have explored how intracellular signaling and multi-cellular interactions integrate to produce emergent patterning of geometrically-heterogeneous and dynamic networks of blood vessels. In so doing, my work has generated a novel biological hypothesis and contributed new computational approaches for multi-cell modeling and model validation.

# TABLE OF CONTENTS

<b>DEDICATION</b>	<b>III</b>
<b>ABSTRACT</b>	<b>V</b>
<b>TABLE OF CONTENTS</b>	<b>VII</b>
<b>LISTS OF FIGURES, TABLES, AND EQUATIONS</b>	<b>X</b>
<b>CHAPTER 1</b>	
<b>INTRODUCTION</b>	<b>3</b>
<b>BACKGROUND</b>	<b>4</b>
ENDOTHELIAL SIGNALING PATHWAYS	5
A ROLE FOR PERICYTES IN ANGIOGENESIS	6
AGENT-BASED MODELING OF ANGIOGENESIS	7
<b>OVERVIEW OF DISSERTATION – INTEGRATING COMPUTATIONAL, IN VITRO, AND IN VIVO STUDIES</b>	<b>8</b>
REVIEWING CURRENT METHODS	8
MODELING IN VITRO ENDOTHELIAL CELL BEHAVIOR	9
EXPLORING IN VIVO SYSTEMS AND PERICYTE BEHAVIOR	10
DISCUSSION OF CURRENT WORK AND FUTURE DIRECTIONS	11
<b>CHAPTER 2</b>	
<b>MULTISCALE COMPUTATIONAL MODELS OF COMPLEX BIOLOGICAL SYSTEMS</b>	<b>12</b>
<b>ABSTRACT</b>	<b>13</b>
<b>INTRODUCTION</b>	<b>14</b>
<b>CURRENT MULTISCALE MODELING EFFORTS</b>	<b>17</b>
SCALES OF BIOLOGY: WHAT ARE WE MODELING?	18
MODELS WITHIN MODELS: THAT WHICH COMPRISES A MULTISCALE SYSTEM	20
SELECTING A COMPUTATIONAL METHOD BASED ON FUNCTION AND SPATIAL RESOLUTION	24
<b>VERIFICATION AND VALIDATION OF MULTISCALE MODELS</b>	<b>28</b>
VALIDATING ACROSS MULTIPLE SCALES	28
INDIVIDUAL VERIFICATION VS. COMPLETE MULTISCALE VERIFICATION	29
<b>BIOLOGICAL INSIGHT FROM MODELS</b>	<b>31</b>
MEASURING THE UNMEASURABLE	31
THE VIRTUAL BENCH: <i>IN SILICO</i> PERTURBATIONS	32
<b>LOOKING FORWARD</b>	<b>34</b>
<b>SUMMARY POINTS</b>	<b>36</b>
<b>FUTURE ISSUES</b>	<b>37</b>
<b>ACKNOWLEDGEMENTS</b>	<b>37</b>

<b>CHAPTER 3</b>	
<b>AGENT-BASED MODEL OF ANGIOGENESIS SIMULATES</b>	
<b>CAPILLARY SPROUT INITIATION IN MULTICELLULAR NETWORKS</b>	<b>38</b>
<b>ABSTRACT</b>	<b>39</b>
<b>INTRODUCTION</b>	<b>40</b>
<b>EXPERIMENTAL</b>	<b>44</b>
EMBRYOID BODY EXPERIMENTS	44
AGENT BASED MODEL	44
<b>RESULTS</b>	<b>51</b>
<b>CONCLUSIONS</b>	<b>57</b>
<b>ACKNOWLEDGEMENTS</b>	<b>60</b>
<b>CHAPTER 4</b>	
<b>COMPUTATIONAL MODEL OF RETINAL ANGIOGENESIS SIMULATES RETINAL VASCULAR</b>	
<b>NETWORK MORPHOLOGY AS A FUNCTION OF PERICYTE COVERAGE.</b>	<b>61</b>
<b>ABSTRACT</b>	<b>62</b>
<b>INTRODUCTION</b>	<b>63</b>
<b>METHODS</b>	<b>65</b>
RETINAL DISSECTION AND IMMUNOHISTOCHEMISTRY	65
MINKOWSKI ANALYSIS	66
ABM TEMPORAL AND SPATIAL CONSTRAINTS	67
ASTROCYTE TEMPLATE GENERATION	68
CELL TYPES AND INITIAL CONDITIONS	69
RECEPTOR BINDING	69
INTERCELLULAR SIGNALING	71
SIMULATED CELL BEHAVIORS	72
<b>RESULTS</b>	<b>74</b>
ABM ASTROCYTE TEMPLATE	74
NETWORK MORPHOLOGY CHARACTERIZATION	76
PERICYTES PRODUCE NETWORKS WITH GREATER BRANCHING AND LARGER LOOPS	78
<b>DISCUSSION</b>	<b>81</b>
<b>ACKNOWLEDGEMENTS</b>	<b>84</b>
<b>CHAPTER 5</b>	
<b>DISCUSSION AND FUTURE DIRECTIONS</b>	<b>85</b>
<b>SYNTHESIS</b>	ERROR! BOOKMARK NOT DEFINED.
<b>CONTRIBUTIONS AND EXTENDED APPLICATIONS</b>	<b>89</b>
SPATIALLY ACCURATE MODEL OF ENDOTHELIAL TIP CELL BEHAVIOR	89
DIRECTLY MATCHING BIOLOGICAL DATA AND USING STOCHASTIC SURROGATES FOR VALIDATION	89
FIRST ABM OF RETINAL ANGIOGENESIS INCORPORATING PERICYTES	90
QUANTITATIVE COMPARISONS BETWEEN ABM AND RETINAL VASCULAR NETWORKS	90
PERICYTES AS BUFFERS FOR ENDOTHELIAL NOTCH1-DLL4 SIGNALING	92
<b>FUTURE DIRECTIONS</b>	<b>93</b>
EXTENDING ABMS TO STUDY ADDITIONAL STAGES OF ANGIOGENIC SPROUTING	93
INCORPORATING TRUE MULTISCALE SIMULATIONS OF ANGIOGENESIS	93
EXPLORING THE EFFECTS OF PERICYTES ON NOTCH1-DLL4 SIGNALING IN ENDOTHELIAL CELLS	95
<b>CONCLUSION</b>	<b>99</b>

<b>REFERENCES</b>	<b>101</b>
<b>APPENDICES</b>	<b>115</b>
<b>APPENDIX I: REPLACING THE BAR GRAPH</b>	<b>116</b>
<b>APPENDIX II: VIRTUAL WOUNDS: COMPUTERS PROBE HEALING</b>	<b>119</b>
VIRTUAL WOUND MODEL NETLOGO CODE	121
<b>Appendix III: NetLogo Code for Embryoid Body Model</b>	<b>125</b>
<b>Appendix IV: Netlogo Code for Retinal Angiogenesis Model</b>	<b>140</b>

# LISTS OF FIGURES, TABLES, AND EQUATIONS

## FIGURES

Figure 1.1: Notch1-DLL4 and VEGF Signaling Pathways.....	6
Figure 2.1: Diabetic Retinopathy as a Case Study in Multiscale Pathophysiology.....	16
Figure 2.2: Multiscale Model Taxonomy .....	18
Figure 2.3: Clustergram of multiscale models as a function of biological discipline and spatial resolution.....	19
Figure 2.4: Map of Modeling Techniques by Scale .....	25
Figure 3.1: Construction of ABM from experimental time-lapse movies.....	46
Figure 3.2: ABM workflow. ....	46
Figure 3.3: Parameterization and validation of ABM based on a diverse population of EB Movies.....	52
Figure 3.4: Comparing ABM and Monte Carlo predictions of sprout initiation locations.....	54
Figure 3.5: Parameter optimization using genetic algorithm to improve performance index.....	56
Figure 4.1: Image processing workflow for retinal Minkowski analysis.....	67
Figure 4.2: Retinal ABM Process Diagram .....	73
Figure 4.3: Development of retinal ABM astrocyte template .....	75
Figure 4.4: ABM Minkowski functionals compared to P3 Retina ECs. ....	77
Figure 4.5: AMB Simulations with PCs outperform all other simulations for generating EC networks with geometries similar to those found in P3 Retinas.....	79
Figure 5.1: Multiscale modeling using ABM of tip cell selection for endothelial cell placement. ....	95
Figure 5.2: Sample heatmaps of signaling molecules generated by the retinal angiogenesis ABM. ....	96
Figure I.1: Challenges displaying big data sets .....	117
Figure I.2: Lightning Plot design.....	118
Figure II.1 Virtual wound model .....	120

## TABLES

Table 3.1: Embryoid Body ABM Parameter Values .....	45
Table 4.1: Retinal Development ABM Parameter Values.....	69

## EQUATIONS

(3.1) DLL4 production and degradation .....	47
(3.2) Receptor production rates.....	47
(3.3) Genetic algorithm optimization function.....	50
(4.1) VEGFR2 forward reaction rate .....	70
(4.2) VEGFR1 forward reaction rate .....	70
(4.3) VEGFR2 reverse reaction rate.....	70
(4.4) VEGFR1 reverse reaction rate .....	70
(4.5) Probability of binding VEGFR2 .....	70
(4.6) Probability of binding VEGFR1 .....	70
(4.7) Stochastic binding conditions for VEGFR1 and VEGFR2 .....	70
(4.9) Insertion rate of VEGFR2 .....	71
(4.10) Modified insertion rate of VEGFR2 .....	71
(4.11) Stochastic insertion and internalization conditions for VEGFR2.....	71
(4.12) Notch1 activity as a function of DLL4.....	72

**MULTICELLULAR AGENT-BASED MODELS OF  
ANGIOGENESIS EVALUATE ENDOTHELIAL CELL  
SIGNALING AND THE ROLE OF PERICYTES IN  
VASCULAR NETWORK PATTERNING**

By Joseph Brian Walpole

“I have to say that those who have a modicum of scientific training tend to go the extra mile. For many, such thinking is second nature. This might not necessarily come from their scientific training *per se* (beware causality), but possibly from the fact that people who have decided at some point to devote themselves to scientific research tend to have an ingrained intellectual curiosity and a natural tendency for such introspection.”

-Nassim Nicholas Taleb, *Foiled By Randomness*

# CHAPTER 1: INTRODUCTION

All tissues of the body rely on an uninterrupted supply of blood flow to maintain homeostasis and prevent tissue necrosis due to metabolic deregulation. The blood vessels that conduct blood throughout these tissues are comprised of a finite number of cellular components – endothelial cells that line the blood vessel lumen and perivascular cells that support the blood vessel through chemical and mechanical means. Despite being derived from the same fundamental cells, vascular networks have unique, tissue-specific geometries that arise during development. In observing these vascular networks, I have often asked myself the simple question: how did this specific network geometry form? In this thesis I present a body of work that addresses this question using computational modeling as a method of hypothesis testing and generation.

In seeking highly quantitative methods for analyzing the network dynamics of intercellular signaling, computational modeling was a natural approach. A computational model allows me to test a minimum set of endothelial cell and pericyte behaviors while simultaneously monitoring the signaling state and magnitude of every cell in the simulation. In particular, agent-based models (ABMs) excel at simulating the behaviors of individual cells and allowing for emergent phenomena to arise as a result of intercellular interactions. Without *a priori* behavioral rules for network-level signaling and organization, ABMs can generate spontaneous complex cellular networks that are a function of a finite set of cellular-level behaviors. In this way, ABMs allow for systematic testing of simplified cellular behaviors while still producing complex network-level outputs.

I have developed two ABMs of angiogenesis to evaluate the formation of vascular networks as a function of endothelial cell signaling and pericyte coverage. Specifically, I have (1) used a combination of stochastic and deterministic approaches to assess angiogenic sprout initiation as a function of Notch1-DLL4 signaling in multicellular endothelial networks, and (2) used quantitative geometric analysis to

assess the function of pericyte coverage by directly contrasting ABM simulations of retinal angiogenesis with developing mouse retinal vascular networks.

Herein, I demonstrate that an ABM incorporating Notch1-DLL4 and vascular endothelial growth factor (VEGF) signaling is capable of predating the frequency and location of angiogenic sprout initiation in multicellular networks with physiologically defined geometries. Further, my ABM of retinal vascular angiogenesis has generated a novel hypothesis for pericytes as “buffers” to endothelial intercellular signaling. The geometric properties of endothelial networks generated by the ABM most closely matched images of murine retinal vascular networks in simulations that incorporated pericytes as passive entities (i.e. without direct control over endothelial signaling) – simulations with only endothelial cells generated more dense, less branched networks that did not mimic physiologic geometric properties.

These combined experimental and ABM studies contribute to a growing field of computational systems biology in which simulations provide accelerated hypothesis generation and testing. Indeed, my work has both generated and tested new hypotheses in the field of vascular biology. Beyond the niche of endothelial cell and pericyte interactions, this extends the broader study of multi-cell self-assembly paradigms in biology using bottom-up modeling approaches.

## **BACKGROUND**

Angiogenesis, the formation of new blood vessels from an existing vascular network, is necessary for the growth, development, and repair of all tissues (Eilken and Adams 2010). Pathologies of the microvasculature are intimately tied to angiogenesis where proliferative diseases (diabetic retinopathy, vascular malignancies, endometriosis) inappropriately engage angiogenic pathways, leading to inappropriate growth of immature vessels (Ferrara 2005, Ejaz, Chekarova et al. 2008, Hammes, Feng et al. 2011, Bandello, Lattanzio et al. 2013). Because angiogenesis is an incompletely understood complex

system, single-target therapeutic approaches, such as Vascular Endothelial Growth Factor (VEGF) gene therapy and blocking antibodies, have had mixed results in the clinical setting (Stewart, Kutryk et al. 2009, Mac Gabhann, Annex et al. 2010).

Angiogenesis is a concerted multicellular event coordinated by endothelial cells and perivascular support cells (pericytes) that can be spatiotemporally subdivided into three main stages: (1) vessel activation, (2) sprout extension/guidance, and (3) anastomosis (Chappell, Wiley et al. 2011, Peirce-Cottler, Mac Gabhann et al. 2012). The first two stages require phenotypic switching of quiescent endothelial cells into a migratory phenotype, dubbed the tip cell (Potente, Gerhardt et al. 2011). These tip cells then respond to soluble growth factor cues such as VEGF to guide a developing endothelial stalk that will potentially lumenize and form a new, patent blood vessel (Xu and Cleaver 2011). Two parallel pathways have been implicated in this process: endothelial-endothelial (EC-EC) lateral inhibition via Notch1-Delta Like Ligand 4 (DLL4) signaling and heterotypic intercellular communication through pericyte-endothelial (PC-EC) adhesions (Paik, Skoura et al. 2004, Tillet, Vittet et al. 2005, Derycke, Morbidelli et al. 2006, Hellstrom, Phng et al. 2007, Simonavicius, Ashenden et al. 2012, Pedrosa, Trindade et al. 2015). Prior investigations of sprouting angiogenesis have primarily focused on endothelial cell behaviors, leaving many unanswered questions regarding the contribution of other cells types, such as pericytes, to both physiologic and pathologic vessel growth (Dulmovits and Herman 2012).

### **Endothelial signaling pathways**

Although there are myriad signaling pathways that converge to regulate angiogenesis, I have chosen to focus on the canonical Notch1-DLL4 signaling axis that is directly integrated with VEGF and VEGF receptor (VEGFR) dynamics (Figure 1.1) (Hellstrom, Phng et al. 2007). Notch1 is a transmembrane protein whose extracellular domain is capable of binding multiple ligands in several different configurations (Benedito, Roca et al. 2009, Sprinzak, Lakhanpal et al. 2010, Pedrosa, Trindade et al.

2015). Ligand of delta-like ligand 4 (DLL4) in trans-configuration (i.e. intercellularly) activates the receptor and releases the Notch intracellular domain (NICD) that localizes to the nucleus and acts as a transcription factor, reducing the expression of VEGFR2 (Leslie, Ariza-McNaughton et al. 2007). Because VEGFR2 is upstream of DLL4 expression, this ultimately forms a reinforcing feedback loop in which an endothelial cell with high levels of VEGFR2 phosphorylation can limit the VEGFR2 expression in its neighboring cells, generating a so-called “salt and pepper” pattern of DLL4 expression (Bentley, Gerhardt et al. 2008, Bentley, Mariggi et al. 2009, Jakobsson, Franco et al. 2010). Finally, these pathways are fundamental to angiogenesis as disruption of any of their constituents causes profound disruption of blood vessel networks (Noguera-Troise, Daly et al. 2006, Hofmann and Luisa Iruela-Arispe 2007, Chappell, Wiley et al. 2011, Wiley, Kim et al. 2011, Louvi and Artavanis-Tsakonas 2012).

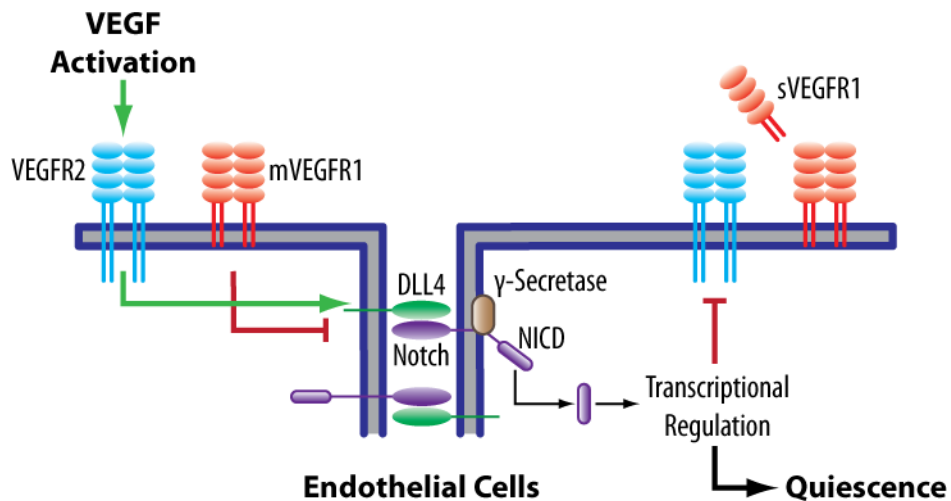


**FIGURE 1.1: NOTCH1-DLL4 AND VEGF SIGNALING PATHWAYS.**

The ABM simulations in this thesis both incorporate Notch1-DLL4 signaling and VEGF/VEGFR binding to inform endothelial cell behaviors. In this example of neighboring endothelial cells, the left cell has become activated through phosphorylation of VEGFR2, increasing DLL4 expression. Notch1 signaling in the right cell causes transcriptional regulation to reduce VEGFR2 expression, leading to a more quiescent phenotype. Membrane and soluble forms of VEGFR1 (m and s, respectively) act as decoy receptors that can competitively inhibit VEGF-VEGFR2 binding.

### **A role for pericytes in angiogenesis**

Pericytes are a phenotypically diverse set of cells that encircle blood vessels and make direct connections through the basement membrane to endothelial cells (Sims 1986, Kelly-Goss, Sweat et al.

2013). Functioning as support cells, pericytes can exert mechanical stabilization of blood vessels (potentially altering capillary flow patterns) and may assist in guidance of extravasated leukocytes (Lee, Zeiger et al. 2010, Stark, Eckart et al. 2013). Loss of pericyte coverage is associated with proliferative vascular diseases, resulting in increased endothelial sprouting and formation of poorly organized vascular networks (Bjarnegard, Enge et al. 2004, Ejaz, Chekarova et al. 2008, Motiejunaite and Kazlauskas 2008, Armulik, Genové et al. 2011). Additionally, pericytes may directly interact with Notch1-DLL4 signaling – Pedrossa et al. demonstrate a loss of pericyte coverage in DLL4 KO with associated increase in vascular permeability (Pedrosa, Trindade et al. 2015).

Despite having a clear functional impact on maintenance of vascular integrity and endothelial cell health, a mechanistic role for pericytes during angiogenesis remains elusive. Particularly in the retina, where pericytes cover almost 100% of capillary area and are directly associated with the angiogenic front during development (Frank, Dutta et al. 1987, Frank, Turczyn et al. 1990), there is a clear need for understanding their function as regulators of endothelial cell behavior during angiogenesis at a mechanistic level.

### **Agent-based modeling of angiogenesis**

While cutting-edge imaging has begun to provide new insight into these fundamental questions, computational modeling offers a powerful alternative approach to hypothesis testing. Computational modeling has been leveraged in endothelial biology to produce significant advances in our understanding of complex Notch1 ligand intercellular signaling during sprouting angiogenesis, providing new hypotheses for patterning and tip cell selection (Bentley, Gerhardt et al. 2008, Jakobsson, Franco et al. 2010, Artel, Mehdizadeh et al. 2011, Hashambhoy, Chappell et al. 2011, Carlier, Geris et al. 2012, Bentley, Franco et al. 2014). ABM techniques are specifically useful as they allow for emergence of

patterning phenomena using rule-based behaviors on the cellular scale that are agnostic to network-scale events.

There are a limited number of ABM simulations of angiogenesis incorporating pericytes (or a general “mural cell” population) and endothelial cells. Kleinstreuer et al. developed a model of liver vasculogenesis (de novo formation of blood vessels) with angiogenic components using a Cellular Potts Model (aka Glazier-Graner-Hogeweg model) approach that uses energy minimization equations to inform stochastic cellular behaviors (Kleinstreuer, Dix et al. 2013). Their success with incorporating pericytes has inspired my ABM of retinal angiogenesis, though I have adopted an alternative to the energy minimization techniques of Cellular Potts models.

## **OVERVIEW OF DISSERTATION – INTEGRATING COMPUTATIONAL, IN VITRO, AND IN VIVO STUDIES**

### **Reviewing current methods**

This document is divided into chapters that catalogue my investigation of ABM techniques to study angiogenesis and vascular network patterning. Chapter 1 reviews multiscale computational modeling in biological systems, not strictly limited to ABMs or to vascular biology. This highlights the challenges associated with modeling across spatial and temporal scales, while suggesting potential methods to overcome these challenges. In particular, the discussion of stochastic and deterministic modeling is relevant to future chapters that leverage the contrast between these techniques to garner greater understanding of endothelial cell biology. The section on multiscale model validation is also important as it highlights some challenges that I faced in validating my own ABMs, such as the selection of proper biological endpoints.

## **Modeling in vitro endothelial cell behavior**

Chapter 2 focuses exclusively on the role of endothelial cells in the patterning of *in vitro* vascular networks. This first foray into multi-agent cellular modeling uses sequential imaging data of embryoid bodies collected by the Bautch Laboratory (University of North Carolina, Chapel Hill) to inform both the initial and final endothelial cell locations in the ABM – the former are used as initial conditions, while the latter provide validation data for the frequency of endothelial cell extension. Combining high-resolution confocal imaging and ABM simulations allows for direct comparison between the computational model output and the biological system it is simulating. This unique 1:1 mapping of endothelial cell position and angiogenic sprout initiation is a novel contribution to the field of vascular biology and more broadly to the development of ABM validation strategies.

A key feature of this work is the analysis of endothelial sprout localization. Demonstrating the accuracy of endothelial sprout frequency was trivial as the biological data was readily available for a concrete comparison. However, determining if the ABM could accurately predict the location of endothelial sprouts provided a challenge – we knew if the locations were accurate, but there was no gold standard measure of inaccuracy. For example, it was not clear if a specific true positive prediction rate was representative of a “good” model prediction. Incorporating a Monte Carlo analysis of purely stochastic cell behavior allowed for a meaningful comparison: is the rule-based ABM better than random chance at predicting *where* endothelial sprouts occur. Ultimately, the ABM demonstrated better predictive power than the Monte Carlo, suggesting that the Notch1 signaling network implementation was indeed sufficient for basic endothelial network patterning. To our knowledge, this work is the first to use Monte Carlo simulations as a benchmark comparator for ABM predictions, as was essential for my model validation strategy.

### **Exploring in vivo systems and pericyte behavior**

As noted, computational modeling efforts to date have not explored the behavior of perivascular cells in retinal angiogenesis. Based on the ABM simulations in Chapter 2, I extended my work to explore the impact of pericytes on vascular network formation in the murine retina. This represents two advances: first, moving towards a more physiological relevant biological model and, second, incorporating the effects of pericytes on endothelial behaviors in the retina. Chapter 3 describes this most recent work and the investigation into quantitative imaging analysis using Minkowski functionals.

Again, the question of model validation is important, and finding a truly accurate quantitative measure of model performance is paramount. The Minkowski functionals are a relatively new tool for studying vascular network geometry and are ideal for studying computational systems. Through measuring binary image parameters (area, perimeter, and Euler characteristic) as a function of image dilation, the Minkowski functionals provide a “fingerprint” of network geometries that can be compared across length scales and imaging modalities. This new ABM of retinal angiogenesis uses the Minkowski functionals to instantiate accurate astrocyte cell networks as initial conditions in the ABM, while also testing the accuracy of predicted endothelial network geometries.

Pericytes are incorporated into the ABM as motile cells that actively wrap endothelial cells without directly modulating cell signaling. Because the function of pericytes on endothelial cell behavior remains unclear I felt it best to first investigate their function simple as a signaling buffer by proposing and testing the hypothesis that pericytes contribute to overall vascular network patterning through the interruption of EC-EC connections.

## **Discussion of current work and future directions**

Finally, I discuss the synthesis of these contributions and potential new avenues of investigation based on my findings. Much has been written about angiogenesis to date, yet still several fundamental questions remain unanswered: what is the role of pericytes during angiogenic sprouting? Is the endothelial cell network geometry purely a function of EC-EC signaling? Are proliferative angiogenic pathologies due to deregulation of endothelial cells, pericytes, or both? Chapter 4 discusses my contribution to these fundamental questions and suggests the logical next experiments to continue this work.

In the context of this evolving field, computational modeling is beginning to flourish as a method for expanding our knowledge and positing new hypotheses. Truly, biomedical engineering offers the tools necessary for advancing fundamental scientific inquiry – not as a singular method, rather as a manner of thought that might conduct research forward through informed computational investigation in a close marriage with experimental studies.

# CHAPTER 2

## MULTISCALE COMPUTATIONAL MODELS OF COMPLEX BIOLOGICAL SYSTEMS

Acknowledgements: Jason A. Papin<sup>\*</sup>, Shayn M. Peirce<sup>\*</sup>

<sup>\*</sup>University of Virginia

The text included in this chapter has been published here:

Walpole J, Papin JA, Peirce SM. Multiscale computational models of complex biological systems. Annual Review Biomed Eng 2013;15:137-54.

## **ABSTRACT**

Integration of data across spatial, temporal, and functional scales is a primary focus of biomedical engineering efforts. The advent of powerful computing platforms, coupled with quantitative data from high-throughput experimental platforms, has allowed multiscale modeling to expand as a means to more comprehensively investigate biological phenomena in experimentally relevant ways. This review aims to highlight recently published multiscale models of biological systems while using their successes to propose the best practices for future model development. We demonstrate that coupling continuous and discrete systems best captures biological information across spatial scales by selecting modeling techniques that are suited to the task. Further, we suggest how to best leverage these multiscale models to gain insight into biological systems using quantitative, biomedical engineering methods to analyze data in non-intuitive ways. These topics are discussed with a focus on the future of the field, the current challenges encountered, and opportunities yet to be realized.

## INTRODUCTION

Biological systems are inherently complex in nature; they are comprised of multiple functional networks that operate across diverse temporal and spatial domains to sustain an organism's growth, development, and reproductive potential. These so-called "multiscale" systems extend from the most basic of amino acid substitutions that alter protein function to concerted multicellular signaling cascades regulating hormone release throughout an entire lifetime. Computational models are uniquely positioned to capture the connectivity between these divergent scales of biological function as they can bridge the gap in understanding between isolated in vitro experiments and whole-organism in vivo models.

While seemingly transparent, a careful definition of multiscale should be explored as it can very quickly spiral into the realm of catch-all scientific jargon. Fundamentally, a multiscale model must **explicitly** account for more than one level of resolution across measurable domains of time, space, and/or function. To clarify, many models of physical systems **implicitly** account for multiple spatial scales by simplifying their boundary conditions into "black boxes" where assumptions about other spatial or temporal domains are summarized by governing equations. Further, explicitly modeled tiers of resolution must also provide additional information that could not be obtained by independently exploring a single scale in isolation.

The classic engineering exercise of heat transfer through an insulated rod is an excellent case study in implicit multiscale modeling. Whether solved using continuous PDEs or a discrete finite element approach, all solutions to this problem rely on carefully defining spatial boundary conditions, the fundamental laws of thermodynamics of a closed system, and material properties such as a thermal conductivity coefficient. Using these tools, engineering students unwittingly wrangle molecular motion at the femtometer scale to reliably predict the distribution of temperatures across an idealized one-dimensional landscape measured in meters. However, were we to explicitly account for the motion of each molecule of metal in the rod would we gain any additional information about the system (assuming

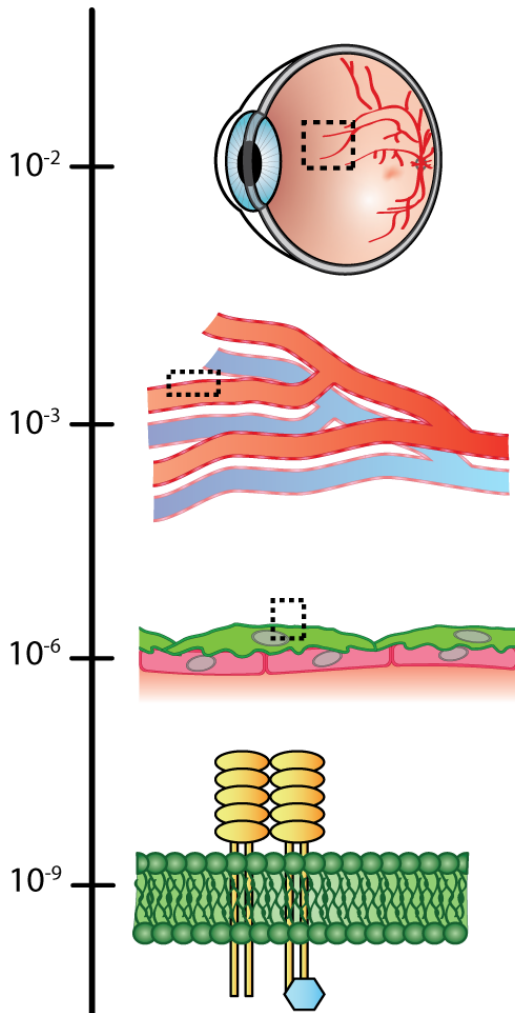
that this were not a computational intractable challenge)? In this case, the governing equations of thermodynamics sufficiently capture the probabilistic distributions of molecules without requiring explicit representation in the model.

Ultimately, this model system is explicitly analyzed at the scale of the rod while implicitly accessing information about molecular thermal motion using established equations of thermodynamics. However, as a “Law of Biological Systems” has yet to be codified into governing equations, the biomedical scientist lacks the means to accurately make assumptions across multiple tiers of measurable resolution. This challenge is further compounded by the complex nature of the system that is being investigated; that is to say, components of biological systems act differently in isolation than they do when integrated into the larger machinery of a living organism.

To further illustrate the need for explicit multiscale models in biology, let us consider the multiple levels of spatial, temporal, and functional scale that are known to operate in the pathophysiology of diabetic retinopathy (Figure 2.1). At its most advanced stage, proliferative diabetic retinopathy can result in blindness due to retinal detachment at the macroscopic level. This event, however, is preceded by years of tissue damage caused by microvascular hemorrhage and fibrovascular remodeling of the retinal basement membrane. These defects in the vessel wall are the result of pericyte (abluminal vascular support cell) apoptosis, leading to aberrant vessel growth and increased vessel permeability throughout the retina. Finally, pericyte apoptosis occurs due to reduction of PDGF receptor survival signaling mediated by activation of PKC-delta and downstream phosphatases in the setting of chronic hyperglycemia (Frank 2004, Geraldles, Hiraoka-Yamamoto et al. 2009).

At what tier of resolution is the most information available for understanding the underlying mechanisms of this complex disease? Conversely, is there a tier of resolution that offers the least understanding of the disease? The debatable answers to these questions have driven model building for decades as investigators attempt to develop the highest information yield from their intellectual

## Spatial Scale (m)



## Pathophysiology

At the organ level, **retinal detachment** can occur due to fibrosis of the basement membrane. Though taking only hours to days for complete detachment and **blindness**, this level of damage is end-stage; after years of fibrovascular remodeling, the retina is mechanically evulsed from the underlying tissue.

Tissue level changes of the **microvasculature** reveal **micro-hemorrhages** as a result of vessel wall disruption. In proliferative disease, **neovascularization** is apparent in the periretinal vascular beds. These are the earliest clinical signs and are pathognomonic of the disease. Disregulation of vessel permeability can lead to **macular edema** and vessel dilatation.

Vessel instability can be directly attributed to **apoptotic cell death** of pericytes and **uncoordinated proliferation** of endothelial cells. These changes occur throughout the course of the disease and are relevant both on short- and long-term time resolutions.

Pericyte apoptosis is triggered due to **dephosphorylation** of PDGF receptors, resulting in reduced survival signaling. This disruption is caused by PKC-delta activation and downstream phosphatase activity. These effects can be measured within **days of exposure to hyperglycemia** and are often persistent and irreversible. A similar mechanism is responsible for endothelial proliferation.

## Measurement Techniques

This is a **macroscopic** event that is most easily observed using a standard ophthalmoscope.

Microscopic flame hemorrhages may be present on ophthalmoscopic exam. In addition, **cotton-wool spots** are often apparent due to local ischemic injury. Definitive measurements of permeability can be completed with **fundoscopic exam** and **fluorescein angiography**.

Pericyte drop out is typically measured microscopically using **immunohistochemical staining** of excised tissues. These observations can be made in murine models of diabetic retinopathy and are commonly studied as indicators of therapeutic efficacy.

Measurements of intracellular signalling are carried out using conventional **molecular biology techniques** such as immunoblotting, in situ hybridization, immunohistochemistry, and immunoprecipitation. **In vitro** assays and **in vivo** models provide tissue samples for analysis.

**FIGURE 2.1: DIABETIC RETINOPATHY AS A CASE STUDY IN MULTISCALE PATHOPHYSIOLOGY.**

A detailed look at how the pathogenesis of diabetic retinopathy is a function of multiple spatial scales across biology.

investments in computational modeling approaches. More recently however, investigators are turning

to multiscale modeling techniques to generate detailed information about complex biological systems.

In these multiscale models, perturbations to fine-grained parameters (e.g. protein modifications) can

generate observable and measurable changes to coarse-grained outputs (e.g. tissue patterning), and

vice versa. This integration across functional, spatial, and temporal scales in biological systems

introduces a powerful tool for capturing and analyzing biological information that is inaccessible to other modeling and experimental techniques.

Herein we describe a meta-analysis of multiscale modeling, focusing foremost on recent publications from the biomedical engineering community. First, we will describe the tiers of biological resolution that have been modeled and the computational techniques leveraged to obtain insightful conclusions. Focus will shift to a discussion of best practices in model verification and validation as we discuss challenges unique to multiscale modeling. Once we have covered the questions and tools used to answer them, we will expand on how multiscale models capture biologically relevant data that may be inaccessible using conventional wet laboratory techniques. Finally, we will look to the future of the field and pose a set of specific landmarks that, if accomplished, may provide even greater insight into the form and function of complex biological systems.

## **CURRENT MULTISCALE MODELING EFFORTS**

Although computational models take many shapes and forms, we propose a simple taxonomy for defining characteristic styles that will serve to define multiscale models for illustrative purposes (Figure 2.2). These “types” of models are neither absolute nor comprehensive; rather, this taxonomy provides a simple reference that will allow for criteria-based discussion of the examples used herein. Type 1 models are iterative approaches in which data from a single scale of simulation is fed into the next tier of resolution. Outputs at each tier are available, however they do not necessarily inform events at previously simulated tiers of resolution. Type 2 approaches rely on independently simulating each scale of resolution to generate outputs for other simulations. In this way, information is passed between tiers of resolution in discrete packets of inputs/output data. Finally, Type 3 approaches use simulations run in parallel with constant communication between tiers of resolution. This approach can also be viewed as a

way for a low-resolution simulation to control and receive information from many simulations at higher resolution.

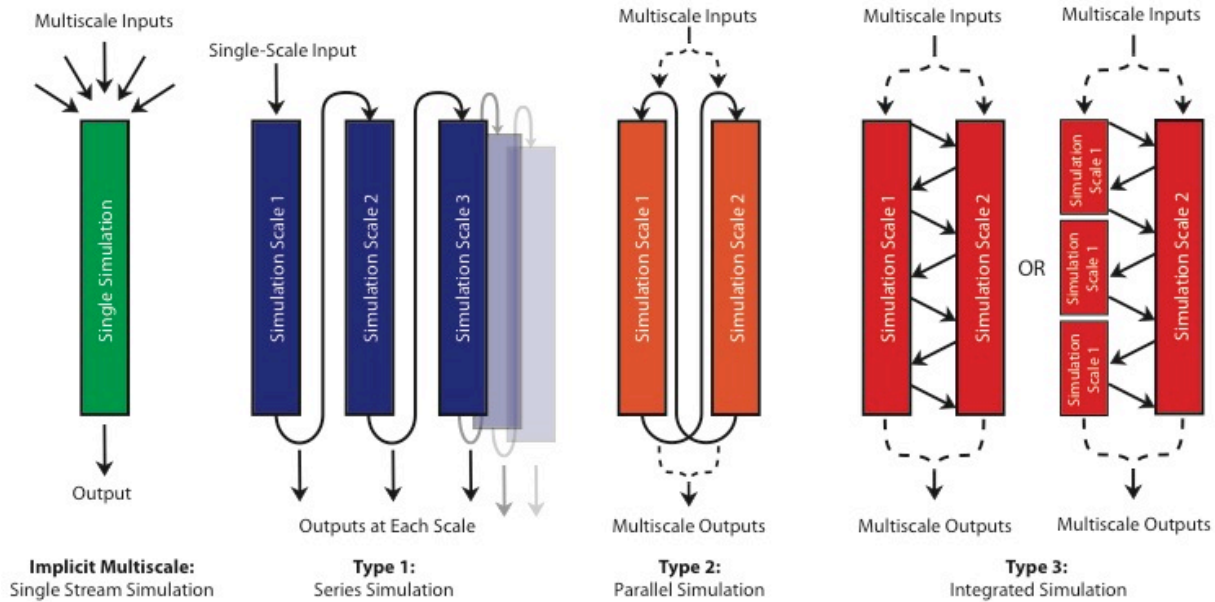


**FIGURE 2.2: MULTISCALE MODEL TAXONOMY**

A proposed system of nomenclature for categorizing the techniques used to generate multiscale models for the purposes of this manuscript.

### Scales of Biology: What Are We Modeling?

Multiscale models are pervasive in the biological sciences, covering many tiers of resolution and many disciplines. Using a selection of literature from the last decade we have highlighted and clustered broad biomedical disciplines based on the levels of spatial resolution they are investigating with multiscale models (Figure 2.3). A clear trend is shown in which metabolomics and genomics research are clustered separately as they are uniquely focused on sub-cellular resolutions (Cosgrove, Alexopoulos et al. 2009, Seok, Xiao et al. 2009, Barua, Kim et al. 2010, Milne, Eddy et al. 2011, Modi, Camacho et al. 2011). Further, studies of tissue mechanics and disciplines interested in cellular trafficking (i.e. cancer and immunology) display the most work at the organ and multisystem scales (Caputo and Hammer 2009, Pospieszalska, Zarbock et al. 2009, Sander, Stylianopoulos et al. 2009, Shirinifard, Gens et al. 2009, Adra,

Sun et al. 2010, Brown, Price et al. 2011, Eissing, Kuepfer et al. 2011, Folcik, Broderick et al. 2011, Scheff, Mavroudis et al. 2011, Sharafi, Ames et al. 2011, Fallahi-Sichani, Kirschner et al. 2012).

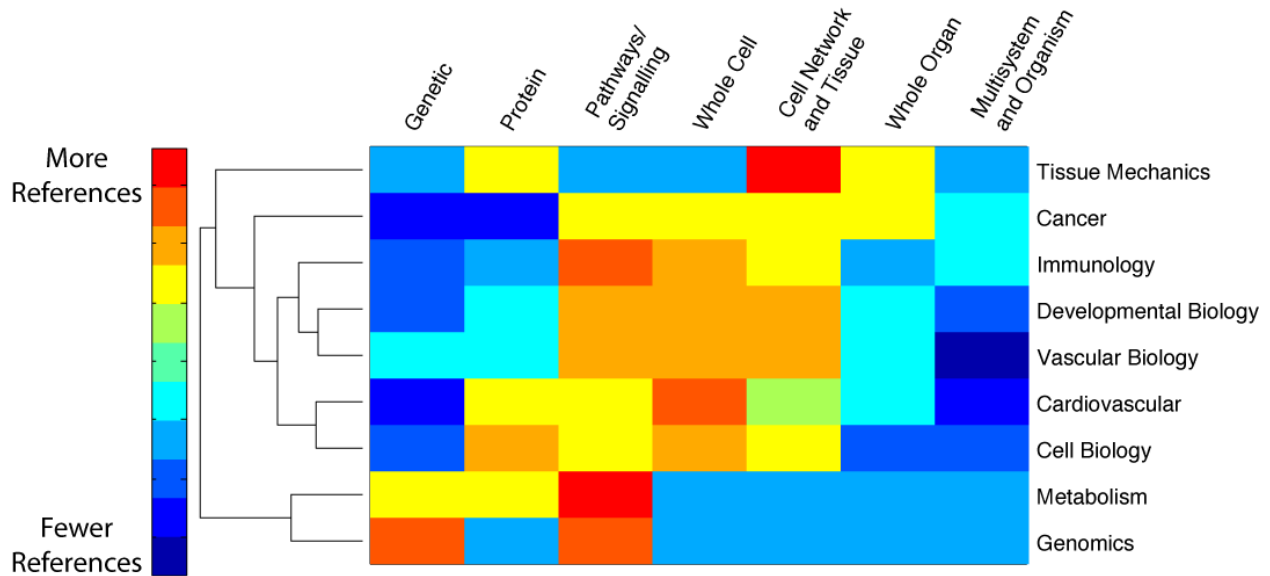


**FIGURE 2.3: CLUSTERGRAM OF MULTISCALE MODELS AS A FUNCTION OF BIOLOGICAL DISCIPLINE AND SPATIAL RESOLUTION.**

Each publication was scored as containing (1) or not containing (0) a biological scale within the described multiscale model. For each discipline, the Boolean values were summed and then normalized to the total number of publications within that category, such that the weighted heatmap is scaled from 0 to 1. For example: of the 7 publications in Vascular Biology, 5 involved Whole Cell components, resulting in a weighted score of  $5/7 = 0.71$ . A total of 39 publications were included in this analysis.

As might be expected, much effort is focused on the interrogation of biology at many resolutions, from signaling networks (i.e. subcellular simulations where proteins are not explicitly modeled) through to cell networks (i.e. tissue-level simulations comprising more than a single cell). In particular, the fields of cell biology, developmental biology, vascular biology, and cardiovascular research all share a very similar pattern of work at these tiers (von Dassow, Meir et al. 2000, Meir, Munro et al. 2002, N'Dri, Shyy et al. 2003, Longo, Peirce et al. 2004, Bailey, Thorne et al. 2007, Tomlin and Axelrod 2007, Grima 2008, Newman, Christley et al. 2008, Schmidt, Papin et al. 2009, Bauer, Jackson et al. 2010, Brodland, Chen et al. 2010, Das, Lauffenburger et al. 2010, Friedl and Wolf 2010, Sample and Shvartsman 2010, Silva and Rudy 2010, Aguado-Sierra, Krishnamurthy et al. 2011, Greenstein and

Winslow 2011, Hashambhoy, Chappell et al. 2011, Holland, Krainak et al. 2011, Liu, Qutub et al. 2011, Moreno, Zhu et al. 2011, Thorne, Hayenga et al. 2011, Vempati, Popel et al. 2011, Causey, Cowin et al. 2012). A common theme among these fields is a desire to understand how subcellular networks may influence tissue-level patterning through the actions of individual cells.

Of course, it should be emphasized that these are trends from a subset of papers that have been broadly classified based on the field of biological research and the explicitly modeled tiers of resolution. This meta-analysis is also purely an evaluation of the **quantity** of publications in a given field and not the **quality** of the models being developed. Clearly, other disciplines are also using multiscale modeling to their advantage; even the disciplines shown contain researchers whose work does not neatly conform to the selected scales. This meta-analysis does, however, demonstrate a clear trend in the literature, which may allow us to glean some insight into current gaps in computational coverage within our disciplines of interest.

Most importantly, this analysis demonstrates that a major goal of the field is yet to be realized: no single comprehensive “gene-to-organism” multiscale model has been developed. Based on our observations there are many open avenues of research within each of the listed disciplines where multiscale efforts are either sparsely represented or completely nonexistent. This deficit is not a shortcoming, but rather an opportunity to push the boundaries of knowledge in these biomedical investigations using multiscale modeling as a platform for high-throughput, high-yield hypothesis generation and testing.

### **Models Within Models: That Which Comprises A Multiscale System**

All modeling methodologies have strengths and weaknesses with regards to their ease and fidelity of capturing biological system dynamics. Typically, these techniques are broadly classified into **continuous** and **discrete** modeling strategies based on how the solution space is acquired. Additional classification

into **deterministic** and **stochastic** models is an alternative method that divides systems based on whether they contain a degree of “randomness” that allows for multiple solutions to the same initial conditions. Importantly, while not an exhaustive list, the modeling techniques presented here are all taken from published multiscale models; these examples are already validated against experimental data and, therefore, serve as a foundation for future computational efforts.

Continuous modeling strategies include using systems of ordinary differential equations (ODEs) and partial differential equations (PDEs) to solve for steady state solutions. Solutions to these continuous systems are deterministic as they obey the Picard-Lindelöf Existence and Uniqueness Theorem (Coddington and Levinson 1955). Because numerical tools for solving PDEs such as Finite Element and Finite Volume methods rely on reduction to a system of ODEs, the assumption of uniqueness still holds despite their ability to contain stochastic elements.

Generally, systems of ODEs using the law of Mass Action Kinetics are leveraged to represent chemical reactions within the cytosol and nucleus of the cell (Adra, Sun et al. 2010, Greenstein and Winslow 2011, Laise, Di Patti et al. 2011, Quo, Moffitt et al. 2011, Scheff, Mavroudis et al. 2011, Fallahi-Sichani, Flynn et al. 2012, Fallahi-Sichani, Kirschner et al. 2012). As the kinetics of molecular binding, conformational switching, and diffusion are often occurring over very small time scales the assumption of steady state in the overall model architecture (which may be discretized into hours, days, weeks, etc.) is typically valid. Sun et al. (Sun, Adra et al. 2009) employed a Type 3 approach using a system of ODEs executed with the COMplex PATHways Simulator (COMPASI) to explicitly model TGF- $\beta$ 1 function in a multiscale model of epidermal wound healing. Using this technique they expanded on a previous single-scale model and were able to decouple the pro-migratory and anti-proliferative effects of TGF- $\beta$ 1 on various cell types in an *in silico* skin wound closure model over time. Analogous reasoning and techniques are also used for analysis of metabolic and signaling networks in which a steady state flux is

desired for informing higher tiers of function (Barua, Kim et al. 2010, Haggart, Bartell et al. 2011, Milne, Eddy et al. 2011, Modi, Camacho et al. 2011, Quo, Moffitt et al. 2011).

Models of reaction diffusion kinetics are also typically modeled in continuous time and are often used to represent intra- and extracellular molecular binding and diffusion (Sample and Shvartsman 2010, Hashambhoy, Chappell et al. 2011, Liu, Qutub et al. 2011, Vempati, Popel et al. 2011, Tveito, Lines et al. 2012). These models differ from previous diffusion/pathway models as they typically rely on systems of PDEs that are then solved using numerical approaches. Broadly speaking, finite element methods (and related finite volume methods) are also uniquely suited for monitoring geometrically-constrained properties such as cell surface interfaces and mechanical properties of tissues across all scales (Du, O'Grady et al. 2010, Goktepe, Abilez et al. 2010, Liu, Qutub et al. 2011, Sharafi, Ames et al. 2011, Zahedmanesh and Lally 2011, Zhang and Gan 2011, Thompson, Gayzik et al. 2012). Aguado-Sierra et al. (Aguado-Sierra, Krishnamurthy et al. 2011) generated a patient-specific three-dimensional model of heart failure in which a finite element mesh was fitted to echocardiographs and mechanical parameters were directly estimated from a combination of MR and cardiac ultrasound (modified Type 2 approach). This work highlights the clinical value of computational models by using patient data to generate electrical conduction and mechanical contractility maps with the potential to inform interventional decisions as processing cost and time decrease. Note that these approaches are a hybrid of continuous and discrete strategies as finite element methods rely on discretization of continuous equations to generate numerical solutions for otherwise irreducible PDEs.

Discrete stochastic modeling techniques are a heterogeneous group of computational foundations that rely on non-deterministic solutions to generate constrained distributions of outputs. These techniques include methods such as Markov Chains, whose probabilistic transition matrices are suited to biological systems whose functions can be discretized into independent states. Along with the related class of discrete state-based Boolean Networks, these techniques have modeled receptor

activation states (e.g. cardiomyocyte ion channels), compartmentalized signaling networks, and functional protein conformations (Bauer, Jackson et al. 2010, Das, Lauffenburger et al. 2010, Silva and Rudy 2010, Greenstein and Winslow 2011, Moreno, Zhu et al. 2011, Trayanova and Rice 2011). Barua et al. (Barua, Kim et al. 2010) have recently developed an algorithm, *GeneForce*, to explore the Boolean rules in metabolic signaling networks and correct for inconsistencies between experimental results and model predictions. The model “forces” an optimized output by allowing for a set degree of rule violation; these perturbations to the original rule set revealed incorrectly silenced gene transcription which, when correct, allowed for agreement with experimental results. This Type 3 approach generated as much as an 8% improvement in model predictive accuracy and was applied to well curated metabolome libraries for organisms such as *E. coli*. From a multiscale perspective, this model identifies genetic-level phenomena that impact metabolomic signaling outputs.

Recently, Agent Based Modeling (ABM) has become a very popular and powerful tool for representing discrete stochastic biological processes as either compartmentalized or spatially defined models. These models include geometries in one-, two-, and three-dimensional configurations and may be scaled such that each fundamental agent is as large (groups of organisms) or as small (sub-cellular membrane components) as is desired. Zahedmanesh et al. (Zahedmanesh and Lally 2011) incorporated a lattice-free ABM with a finite element approach to explore the effects of porosity, compliance, cyclic strain, and flow-induced shear stress on tissue engineered blood vessels (Type 2 approach). This investigation was able to explore how these complex and non-intuitive parameters combined to affect development of intimal hyperplasia over time with potential to make predictions across time scales that cannot be investigated using in vitro techniques. Owing to their diversity of scale, AMBs have been used to describe multicellular processes including tissue electrical conduction, cell trafficking, tissue mechanics, immunomodulation, arterial remodeling, inflammation and many others (Bentley, Gerhardt et al. 2008, Adra, Sun et al. 2010, Das, Lauffenburger et al. 2010, Artel, Mehdizadeh et al. 2011, Brown,

Price et al. 2011, Folcik, Broderick et al. 2011, Liu, Qutub et al. 2011, Thorne, Hayenga et al. 2011, Fallahi-Sichani, Flynn et al. 2012).

### **Selecting a Computational Method Based on Function and Spatial Resolution**

The computational techniques presented in the previous section were selected as examples currently being employed in multiscale models. We classified the techniques into continuous-deterministic and discrete-stochastic (with some exceptions and hybrids), while highlighting specific spatial and temporal domains that these models are suited to represent. This classification forms the basis for a discussion of how multiscale models can be designed by selecting the best computational techniques for the task rather than forcing a modeling technique to approximate a system for which it is poorly suited. To this end, we propose some guidelines for how these individual techniques can be combined across scales (Figure 2.4).

As a class of modeling techniques, network analyses include discrete state-based techniques (e.g. Markov chains, Boolean networks) as well as continuous systems biology approaches (e.g. Flux Balance Analysis). These methods are well suited to modeling the smallest tiers of resolution: genomic, proteomic, and metabolomic. Note that these are different scales of network connectivity and represent their own tiers of resolution. Genomic data is spatially compartmentalized to the nucleus and is temporally independent of proteomic concentrations and posttranslational modification. Similarly, events occurring at the metabolic scale, while dependent on proteomic data, integrate multiple proteins and their relative concentrations and localizations. As such, these sub-cellular regimes, while biochemically codependent, are independent modules for simulation.

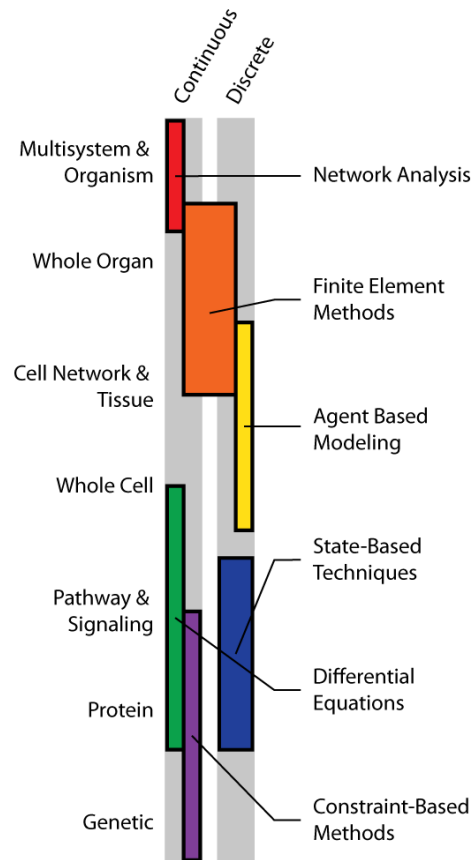


**FIGURE 2.4: MAP OF MODELING TECHNIQUES BY SCALE**

Conceptual map of modeling techniques divided into continuous and discrete categories across spatial scales for which they are most suited.

Recently demonstrated by Milne and colleagues (Milne, Eddy et al. 2011), construction of a composite Gene-Protein-Reaction (GPR) model to simulate regulation of butanol production as a function of growth conditions (e.g. growth medium, atmosphere) supported the hypothesis that *Clostridium beijerinckii* was an ideal candidate for biofuel applications. The *i*CM925 model contained 925 genes coding for 938 reactions involving 881 metabolites – approximately 18% of the protein coding genome of *C. beijerinckii*. This level of detail and network annotation for a relatively understudied organism was captured and analyzed with linear algebraic equations defined by a homogenous ODE constrained with mass balance principals. Simply put, a vast amount of multiscale data (genetic

expression and metabolomic network connectivity) was integrated using a single computational technique through a Type 1 approach.

In the sub-cellular regime, continuous-deterministic systems of ODEs and PDEs are also ideal for monitoring concentrations of signaling molecules in both the intra- and extracellular domains. These systems are often less comprehensive than the previously described network analyses due to the paucity of relevant kinetic parameters; however, they excel at explicitly accounting for binding kinetics and monitoring rates of reactions as a function of time. Sample et al. (Sample and Shvartsman 2010) demonstrate the use of these continuum approaches to solve for gradients of morphogens within the developing *Drosophila* embryo. In their model, solving for compartment-dependent degradation rates was integral to understanding nuclear-cytoplasmic shuttling of morphogens, which are responsible for long-range patterning (hybrid of Type 1 and Type 2 approaches). Although only focusing on a single protein, this technique expands the resolution from purely intracellular reactions to subcellular components with intercellular interactions.

At this point, many of the internal cellular components (i.e. genome, proteome, and signaling networks) have been explicitly accounted for; the next tier of resolution, the whole cell, now requires additional consideration as the functions of interest are again interwoven with the scale of investigation. Here, the cell may be viewed as a mechanical entity with discretized membrane segments and interconnected cytoskeletal components or it may be viewed as itself being the smallest component of the system. This biological scale is a natural transition point where both continuum and discrete modeling approaches have been successful, and it falls to the investigator to make the final decision guided by the hypothesis to be tested. Practically, if the cell is the largest entity in the system (i.e. only a single cell is being modeled) a more fine-grained approach is necessary. The converse is also true: if the cell is part of a larger tissue network it must be more coarsely resolved to allow for observations to be feasible given limited computing resources.

For the sake of simplicity we will consider that the cell is itself a transition state between the sub-cellular and super-cellular domains (this notably excludes mechanical analyses of single cells which are often performed at the whole-cell level). Such a view favors a discrete-stochastic approach to cell behavior as this captures a degree of biological noise and allows for easy representation in physical space. ABMs are well suited to this task as they can be specifically adapted to represent cells as either single- or multi-agent entities within the system. Bentley et al. (Bentley, Gerhardt et al. 2008) chose the later approach and represented a capillary as a linear array of ten endothelial cells, each comprised of 1288 membrane agents. This representation was necessary as their analysis required discrete membrane localization of receptors, as well as detailed filopodial sprouting within a three dimensional extracellular space (Type 1 approach). Bailey et al. (Bailey, Thorne et al. 2007) opted on the former approach, representing each endothelial cell in the network as a single agent to generate a larger microvascular system (Type 1 approach). Again, this selection was reasonable based on the analysis at hand: leukocyte extravasation as a function of adhesion molecule expression in a tissue bed.

Tiers of resolution beyond the cell network and tissue level, as demonstrated in Figure 2.3, remain largely unexplored as components of multiscale models. This focus may be due to technical limitations such that computational power is not yet available to track discretized agents throughout an entire organism. Larger, whole-organ models do exist and typically adopt a finite element approach where each cell is represented as part of the discretized mesh. Moreno and colleagues (Moreno, Zhu et al. 2011) were very successful with this technique, using a finite element approach to analyze the effects of antiarrhythmic pharmaceuticals on cardiac conduction through a fully rendered three-dimensional human heart (several Type 1 iterations). This model stands out particularly, because the smallest explicitly resolved element was the well-studied cardiomyocyte sodium channel. This voltage-gated channel was modeled using Markov states that were altered in the presence of various inhibitors. Most notably, cardiotoxic concentrations of antiarrhythmics could not be predicted at the single-cell scale;

however, when cells operating with the same parameters were linked into a network (and ultimately a complete tissue), the model very closely matched clinically observed data.

To summarize: function and spatial resolution beget modeling technique. Based on our current understanding and computational limitations it is necessary to view some biological processes as continuous equations and others as discrete states. As we ascend from sub- to super-cellular resolutions, continuous models that were once exceptionally accurate begin to lose resolving power. Conversely, discrete models are often computationally expensive and become most useful at lower resolution for cell networks and tissues where cells are easily viewed as individual modules. Yet larger systems may require a return to network approaches to account for spatial distances and boundaries between organ systems that are too large to be explicitly modeled at the cellular level.

## **VERIFICATION AND VALIDATION OF MULTISCALE MODELS**

### **Validating Across Multiple Scales**

As with all computational models, multiscale approaches must be rigorously tested against independent data sets for proper validation prior to use as experimental constructs. Recently, Qu and colleagues (Qu, Garfinkel et al. 2011) have reviewed how information is translated between scales of models and highlighted several of the challenges associated with validation across tiers of resolution. A key observation from this review is that inherently noisy stochastic systems and noiseless deterministic systems can generate dramatically different outputs when used to model the same biological phenomena (Keizer's Paradox). Furthermore, adding noise to a previously noiseless system by combining deterministic and stochastic models may increase the likelihood of phase transitions, increasing the number of stable solutions. These additional solutions may be biologically relevant; however, they may also become problematic as their addition could be viewed as incongruence between continuous and discrete systems.

Ultimately, this challenge reduces to the simple fact that we lack the computational resources to explicitly model every protein in a living organism simultaneously. Multiscale models must rely on techniques such as those mentioned above (selecting appropriately resolvable approaches based on function and spatial scale; using integrative systems biology) to capture accurate and robust information from each tier of resolution. It stands to reason that by linking potentially divergent modeling techniques we may introduce inconsistencies into our multiscale systems. To reach model agreement (both inter-model agreement and agreement with biological experiments), we must decide on a validation strategy that is both theoretically sound and computationally practical.

### **Individual Verification vs. Complete Multiscale Verification**

Multiscale models often originate by linking individual models from two different scales to generate a composite system. In the cases where each tier of a model has been independently published they must, by definition, be validated at the single-scale level before validating at the multiscale level. Our lab has, in collaboration with others, followed this strategy to generate Type 2 multiscale models from successfully implemented single-scale models (Valentin and Humphrey 2009, Valentin and Humphrey 2009, Thorne, Hayenga et al. 2011). In this particular example, the multiscale model captured continuum elements (extracellular matrix composition, fluid dynamics, etc.) as well as discrete elements (mechanical properties as determined by cell number and orientation) to generate a blood vessel wall for measuring adaptation to chronic hypertension.

As explored by Hayenga and colleagues (Hayenga, Thorne et al. 2011), prior to generating a comprehensive model, the continuum and discrete systems shared common outputs that were independently validated. Importantly, despite sharing independently validated outputs, the models were not in complete agreement as they drew on data from different scales. The discrete agent based model was generated from cell-level data acquired primarily from reduced in vitro systems that no

longer maintained systems-level responses. Conversely, the continuous constrained mixture model was based on tissue-level data from studies of tissue parameters in which different systems-level responses were potentially still intact. Disagreement between the models presented a significant challenge, as neither was, strictly speaking, incorrect.

Ultimately, to reconcile these differences between scales and allow for comprehensive model validation, agreement on shared variables was required. As such, each model was deemed equally “unreliable” for the purposes of weighting parameters for a genetic algorithm approach to parameter estimation. Agreement between the continuous and the discrete models was achieved for shared parameters, allowing for validation of independent terms using a shared data set.

Fedosov et al. (Fedosov, Lei et al. 2011) describe a multiscale model of erythrocyte membrane mechanics in the context of malaria infection and how changes in material properties and cell geometry impact bulk blood viscosity (Type 1 approach). In this example, validation was performed at the cellular level using optical-tweezer and optical magnetic twisting cytometry to measure deformability of erythrocytes during different stages of malaria parasite development. Bulk blood viscosity was validated against a separate data set to demonstrate that each tier of model resolution independently achieved agreement with biologically relevant data sets. In order to perform these validations, previously dimensionless particle models had to be scaled using erythrocyte diameter as a reference length. This example highlights how careful selection of units and appropriate parameter selection is necessary to achieve multiscale validation.

Multiscale models are subject to scrutiny at both individual and integrated tiers of resolution. To appropriately parameterize a model and achieve validation, it is necessary to ensure that each module or computational technique is itself in agreement with biological data before advancing to a complete multiscale simulation. Further validation of the multiscale model is required to test the reliability of data transfer between computational scales such that crosstalk between continuous and discrete systems

does not introduce artifacts or discrepancies. As with all modeling efforts, thorough and thoughtful validation is key to achieving acceptance in the biological community; the predictive power of a model is dependent on the rigor of this validation.

## **BIOLOGICAL INSIGHT FROM MODELS**

### **Measuring the Unmeasurable**

Most modeling endeavors begin with a hypothesis that cannot be easily tested using even the most cutting edge experimental assays. Tracking individual macrophages in real time in vivo, measuring chemokine concentration gradients throughout an entire tissue region, determining frequency responses to mechanical stimuli in the human ear, observing capillary and lymphatic filling as a function of muscle contraction, quantifying the effects of drug therapy on granuloma formation over the course of 300 days with receptor-level resolution – these are just a few examples of recent investigations that would not otherwise be possible without multiscale modeling approaches (Bailey, Thorne et al. 2007, Vempati, Popel et al. 2011, Zhang and Gan 2011, Causey, Cowin et al. 2012, Fallahi-Sichani, Flynn et al. 2012). Multiscale models are capable of quantifying any explicitly implemented variable as an output across all tiers of resolution.

In addition to quantifying individual variables with relative ease, multiscale models also allow for simultaneous observation of multiple parameters across resolution domains. Tracking multiple variables across a range of parameter values allows for construction of valuable phase planes to describe systems-level behaviors (Bentley, Gerhardt et al. 2008, Sample and Shvartsman 2010, Moreno, Zhu et al. 2011, Fallahi-Sichani, Kirschner et al. 2012). Bifurcations in these phase plane analyses offer insights into system stability and potential interventional targets that may yield higher likelihoods of maintaining transitions from one equilibrium state of a biological system to another. For example, Kim et al. (Kim and Maly 2009) explored reorientation of individual CD8<sup>+</sup> T-killer lymphocytes in the two-dimensional

parameter space defined by microtubule length and initial centrosome orientation relative to a target cell (Type 2 approach). This analysis reveals complex relationships between the parameters, suggesting certain combinations that would render the T-killer unable to properly orient itself for productive cytolytic activity. Such incompatible orientations could not be predicted by either parameter alone, emphasizing the need for more rigorous analysis.

Similarly, as in Holland et al. (Holland, Krainak et al. 2011), acquiring large sums of data across multiple scales of resolution allows for more informed selection of reducible components within complex systems (Type 2 approach). Using a graphical approach in a normalized phase plane to study the kinetics of  $\beta$ -adrenergic signaling, this investigation demonstrates a method to identify reactions that can reasonably be reduced reasonably to steady-state when evaluating system dynamics. Each reaction trajectory in the system was compared relative to steady-state values: trajectories in the phase plane with greater deviations from steady-state had larger hysteresis loops and could be identified as necessary for capturing dynamics of system behaviors.

These examples highlight how traditional engineering approaches to capturing system behaviors can be applied to biological systems. However, as these approaches generally require large sums of quantitative data to be useful, traditional wet lab experiments are not easily translated to these analysis techniques. Computational models, in particular multiscale models, offer an alternative source of data that can be acquired across many parameter values in a high throughput manner. As experimental methodologies develop, these predictions can themselves be independently validated or they may provide insight into unexplored hypotheses that can be tested immediately.

### **The Virtual Bench: *in silico* Perturbations**

Beyond simply capturing otherwise inaccessible measurements with high resolution across large changes in scale, multiscale modeling allows for precise manipulation of network variables to isolate

true effects from experimental artifacts. Even the most precise RNA interference strategies (including small interfering, short hairpin, and micro RNA) are capable of producing off-target effects either directly (e.g. silencing alternative binding sites) or indirectly (e.g. diminution of native RNA translation), resulting in confounding or erroneous observations (Singh, Narang et al. 2011). This statement does not imply that models are error-free; models simply are capable of isolating perturbations as defined by the user's constraints without concern of unknown interactions.

Thus, at first glance multiscale modeling offers the unique advantage of being able to make perturbations across any tier of resolution. This is potentially very powerful as it allows for not only knockdown and overexpression experiments, but also very precise changes to the degree of expression of a single gene or set of genes. This control, quite simply, is not possible with current microbiology techniques. While not a replacement for experimental investigation, these approaches can serve to contextualized data and reconcile discrepancies that may be caused by off-target effects. Further, computational methods may also refine experimental approaches by surveying all possible perturbations to narrow the scope of experimental interrogation.

As an example, Fallahi-Sichani and colleagues (Fallahi-Sichani, Flynn et al. 2012, Fallahi-Sichani, Kirschner et al. 2012) have described the effect of modifying NF- $\kappa$ B signaling mechanisms at the level of transcript stability with implications of temporal variables (e.g. degradation rate, activation rate) affecting the outcomes of *Mycobacterium tuberculosis* infection (Type 2 approach). In this work, pharmaceutical therapies were applied using a system of ODEs to capture intracellular signaling pathways while cellular behaviors were executed as a discrete probabilistic agent based model at the tissue level scale. This union of subcellular pathway manipulation and multicellular function allows for direct investigation of pharmaceutical intervention on a relevant pathophysiological outcome that would otherwise be unobtainable by modeling an individual tier of resolution.

Alternatively, for systems being modeled with a top-down approach, more general questions can be answered by completely removing subsystems from multiscale models. In these cases **functional** impairments are evaluated as opposed to specific physiological interventions. Using this approach, Shirinifard and colleagues (Shirinifard, Gens et al. 2009) demonstrated unique growth patterns in avascular tumors by removing the capability for angiogenic growth from their multiscale model of solid tumors. Insights from such a broad phenotype perturbation (i.e. complete abrogation of angiogenesis rather than impairment of a single component in the pathway with downstream effects) allow for investigations into the minimal functions necessary for individual system behaviors.

Further, the concept of *in silico* perturbations can be extended as a direct analogy to bench work – with the exception that it can be executed at high throughput with low resource allocation. More so than modeling at a single resolution, multiscale models can be directly mapped to biological assays for both experimental validation and hypothesis testing. For some of these cases, multiscale models have proven predictive for optimizing biopolymer scaffolds based on altering material properties to investigate extracellular matrix mechanotransduction and cell seeding (Sander, Stylianopoulos et al. 2009, Artel, Mehdizadeh et al. 2011, Zahedmanesh and Lally 2011). Here, small parameter changes that could easily be completed with computational iteration would require extensive material cost and time commitment to generate comparable data sets.

## **LOOKING FORWARD**

Throughout this review we have highlighted the currently available computational tools for multiscale modeling and the best practices for their implementation. As shown in Figure 2.3, many disciplines of biological research have yet to fully leverage the power of multiscale modeling across more than a few tiers of resolution. That being said, examples do exist that span the spectrum from the most fundamental genetic modifications to organ-level perturbations. Combining these tools across all of

these scales simultaneously may seem at this point an intractably difficult problem; however, some preliminary efforts are already emerging.

The Physiome Projects are a collection of biological databases, mathematical models, and utilities being gathered with a singular purpose: integration (Bassingthwaight and Chizeck 2008, Bassingthwaight 2010). Models from every spatial, temporal, and functional scale are being curated as individual modules such that they can be preserved for integration into larger, multiscale simulations. The efforts of this project are ongoing as it recognizes that, primarily due to computational limitations, a single, whole organism model that explicitly incorporates all tiers of biological resolution has yet to be realized. As we have noted earlier, the majority of information is concentrated near the cellular level with decreasing availability of models and data at the genetic and whole organism levels. This ongoing effort shows much promise as a means to begin generating larger multiscale models from validated, optimized modules that have been assembled with integration in mind.

Beyond implementing better and more comprehensive multiscale models, the future of the field also holds potential to advance other recently accelerating fields of biomedical engineering. In particular, efforts in synthetic biology are using multiscale data and analysis to inform design optimization and control systems theory of novel biological systems. In a recent publication, Nawroth and colleagues (Nawroth, Lee et al. 2012) describe the design, development, and implementation of a synthetic jellyfish capable of self-propulsion dubbed the “Medusoid.” They describe the reverse engineering process as occurring over several orders of space and time in order to capture the necessary information to generate synthetic muscle fibers capable of productive, concerted contraction. Callura et al. (Callura, Cantor et al. 2012) are similarly beginning to use multiscale approaches as they scale up from a single gene to a composite “genetic switchboard.” Capable of regulating four metabolic genes in *E. coli*, this synthetic regulatory system reliably shunted flux through different carbon-utilizing pathways as measured by mRNA levels and direct quantification of metabolites. This effort demonstrates in a strictly

in vitro sense how multiscale theory can be applied to better understand and engineer biological systems.

Multiscale modeling, above all, strives to better understand the fundamental processes that sustain biological life. Unquestionably, effects at the genetic level are responsible for both subtle and dramatic phenotypic expression of an entire organism. We are only just starting to begin to construct computational models that can explicitly demonstrate this same degree of emergent pattern phenomena through appropriate inter-scale connectivity. It is our hope that the techniques and practices presented here are able to guide future efforts in this field towards high quality multiscale model implementation.

#### **SUMMARY POINTS**

1. Multiscale models are explicitly executed simulations of complex biological systems that have been integrated across temporal, spatial, and functional domains. Through simultaneous evaluation of multiple tiers of resolution, multiscale models provide access to systems behaviors that are not observable using single-scale techniques.
2. A combination of multiple computational techniques, including both continuous and discrete systems, is optimal for efficiently capturing information across biological scales. Each spatial scale can be summarized by the biological functions occupying that tier of resolution, allowing for modeling techniques to be implemented based on how well they represent these functions.
3. Multiscale models more closely recapitulate traditional bench top experimentation while allowing for high throughput hypothesis generation and testing, quantitation of values that cannot be measured, and translation to in vivo systems. Perturbations to high-resolution parameters (e.g. protein binding constants) can generate low-resolution outputs that are

biologically relevant (e.g. tissue developmental patterning), allowing for simultaneous access to quantifiable values across all scales of biology.

## **FUTURE ISSUES**

1. Fundamental to the model building process, sensitivity analyses are performed to explore the parameter space for potentially interesting and useful “tuning” variables on which system outputs are strongly dependent. Multiscale models must be thoroughly investigated to determine whether sensitivities are truly a function of the system behavior or an artifact of coarse-graining lower resolution outputs. This area will require further investigation through the continued development of multiscale and complex systems models.
2. Appropriate parameter selection remains a concern in the computational modeling community, as many of the parameter values required to develop multiscale models are either difficult or impossible to measure. Values obtained from in vitro data may not be suitable for multiscale models operating at a tissue network or larger spatial scale. As such, exploration of parameter estimation techniques may be required to better parameterize multiscale models. Alternatively, emerging in vivo molecular imaging techniques may grant access to previously unobtainable parameter values.

## **ACKNOWLEDGEMENTS**

The authors wish to acknowledge funding from the National Institutes of Health (R01 GM088244 to Jason A. Papin and NIH-HL082838 to Shayn M. Peirce) and the Cystic Fibrosis Research Foundation (grant 1060 to Jason A. Papin).

# CHAPTER 3

## AGENT-BASED MODEL OF ANGIOGENESIS SIMULATES CAPILLARY SPROUT INITIATION IN MULTICELLULAR NETWORKS

Acknowledgements: John C. Chappell<sup>†</sup>, Julia G. Cluceru<sup>†</sup>, Feilim Mac Gabhann<sup>‡</sup>,  
Victoria L. Bautch<sup>†</sup>, Shayn M. Peirce<sup>\*</sup>

<sup>†</sup>University of North Carolina, Chapel Hill

<sup>‡</sup>Johns Hopkins University

<sup>\*</sup>University of Virginia

The text included in this chapter is currently under review in *Integrative Biology*:  
Walpole J, Chappell JC, Cluceru JG, Mac Gabhann F, Bautch VL, Peirce SM. Agent-based model of  
angiogenesis simulates capillary sprout initiation in multicellular networks.

## **ABSTRACT**

Many biological processes are controlled by both deterministic and stochastic influences. However, efforts to model these systems often rely on either purely stochastic or purely deterministic methods. To better understand the balance between stochasticity and determinism in biological processes a computational approach that incorporates both influences may afford additional insight into underlying biological mechanisms that give rise to emergent system properties. We apply a combined approach to the simulation and study of angiogenesis, the growth of new blood vessels from existing networks. This complex multicellular process begins with selection of an initiating endothelial cell, or tip cell, which sprouts from the parent vessels in response to stimulation by exogenous cues. We have constructed an agent-based model of sprouting angiogenesis to evaluate endothelial cell sprout initiation frequency and location, and we have experimentally validated it using high-resolution time-lapse confocal microscopy. ABM simulations were then compared to a Monte Carlo model, revealing that purely stochastic simulations could not generate sprout locations as accurately as the rule-informed agent-based model. These findings support the use of deterministic approaches for modeling the complex mechanisms underlying sprouting angiogenesis over purely stochastic methods.

## INTRODUCTION

To understand, harness, and modulate complex systems, science must go beyond a deterministic cause-and-effect view of the natural world. While some biological subsystems may be described using deterministic rules, many must be supplemented with probabilistic or stochastic methods to understand, model, and predict the outcomes of biological processes (Blake and Collins 2005, Kaern, Elston et al. 2005, Balazsi, van Oudenaarden et al. 2011). Randomness in model descriptions of a biological system can be included at three tiers: (1) the biology itself may include stochastic elements or events (e.g. gene expression) that are described in the model using stochastic methods (Kaern, Elston et al. 2005, Laise, Di Patti et al. 2011), (2) measurements of the biological system may introduce sampling errors that propagate random noise, which should be accounted for in a model to understand the underlying biological mechanism being sampled; or (3) underlying deterministic behavior can be modeled using validated stochastic approaches as a method to reduce model complexity and computational cost without loss of insight (Alber, Chen et al. 2006, Cotter, Klika et al. 2014). Further, stochastic behavior may represent a contextual phenotype – a system may normally exist with strict deterministic control but then transition to stochastic behavior when certain conditions are met (e.g. chemokine signaling or pathological pathway activation) (Kulkarni, Shiraishi et al. 2013). Alternatively, a system may be stochastic at physiological conditions but converted to deterministic behavior when integrated into a more robust signaling network, such as in bacterial colony formation (Weber and Buceta 2013, Ben-Jacob, Lu et al. 2014).

We sought to explore this balance of stochastic and deterministic behaviors in the setting of sprouting angiogenesis, a fundamental biological process underlying blood vessel network growth throughout development (Potente, Gerhardt et al. 2011). In the adult, sprouting angiogenesis has roles in both wound healing and endometrial vascularization. Additionally, pathologic sprouting angiogenesis is implicated in the expansion of solid tumors (Folkman 1971, Plank, Sleeman et al. 2004, Strieter,

Burdick et al. 2006, Swanson, Rockne et al. 2011), growth of ectopic endometrial tissue in endometriosis (Fainaru, Adini et al. 2008, Machado, Berardo et al. 2010), and in neoangiogenesis of diabetic retinopathy (Hammes, Feng et al. 2011, Bandello, Lattanzio et al. 2013, Bressler, Qin et al. 2013). Sprouting angiogenesis can be approximated by five main stages: (1) tip cell selection, (2) endothelial stalk extension, (3) stalk guidance to neighboring or nearby vessels, (4) anastomosis with a neighboring vessel (success) or regression/collapse to the originating vessel (failure), and (5) maturation and lumenization of anastomosed vessels (Chappell, Wiley et al. 2011). Regardless of the final fate of the sprout, this process must begin with appropriate selection of a quiescent endothelial cell to undergo phenotype switching, becoming a tip cell with increased filopodial extension frequency. These cell behaviors, in aggregate and in conjunction with external signaling cues, have been presumed to dictate where new vessels initially form within a blood vessel network.

Regulation of endothelial phenotype switching is closely tied to several signaling pathways, including the well-studied Notch1/Delta-Like-Ligand 4 (DLL4) intercellular pathway (Noguera-Troise, Daly et al. 2006, Bentley, Gerhardt et al. 2008, Merks, Perryn et al. 2008, Benedetto, Roca et al. 2009, Staton, Reed et al. 2009, Eilken and Adams 2010, Chappell, Wiley et al. 2011, Potente, Gerhardt et al. 2011, Louvi and Artavanis-Tsakonas 2012), which suppresses sprout initiation, and the vascular endothelial growth factor receptor (VEGFR) axis that signals to increase phenotype switching and sprout frequency (Ferrara 2005, Potente, Gerhardt et al. 2011, Wiley, Kim et al. 2011). Disruption of either the suppressive pathway (Notch1/DLL4) or the activating pathway (VEGF/VEGFR) results in dramatic blood vessel phenotypes ranging from early embryonic lethality to significant vascular dysmorphogenesis (e.g. hypersprouting, hyperbranching phenotypes). Further, there are several isoform and dimerization states of VEGFRs allow for differential signaling (Ferrara, Gerber et al. 2003, Ferrara 2005, Benedetto, Roca et al. 2009, Chappell, Taylor et al. 2009, Louvi and Artavanis-Tsakonas 2012). In this work, we explore the balance between pro-angiogenic VEGFR2 and VEGFR1, which can function as a decoy receptor for VEGF.

As such, the balance between the DLL4 and VEGFR signaling axes is crucial to vascular patterning. However, endothelial cell behaviors leading to sprout initiations in the context of intercellular signaling and capillary network connectivity remain unclear.

Computational models offer unique insight into the study of biological systems, enabling us to query unmeasurable, unobservable, or inaccessible metrics pertinent to biomedical science (Kirschner and Linderman 2009, Gopalakrishnan, Kim et al. 2013, Long, Rekhi et al. 2013, Walpole, Papin et al. 2013, An and Kulkarni 2015, Cilfone, Ford et al. 2015). In assembling a model, the investigator is able to explicitly define methods for simulating each aspect of the biological processes they are modeling – either as stochastic or as deterministic. Comparisons between models that assume different relative contributions of stochastic and deterministic behaviors empower investigation of the underlying system properties by contrasting the accuracy of each technique. The relevant question then becomes: what do we learn from modeling a system using separate deterministic and stochastic techniques that both provide verifiable results?

Several other computational models have been developed using primarily deterministic methods to explore the process of sprouting angiogenesis with single-cell and subcellular resolution. These include ABMs of endothelial phenotype switching that focus on filopodial extension and intercellular Notch1 signaling (Bentley, Gerhardt et al. 2008). Bentley and colleagues have extended this model to bone regrowth as the multiscale model of osteogenesis and sprouting angiogenesis incorporating lateral inhibition of endothelial cells (MOSAIC) (Carlier, Geris et al. 2012), and more recently used it to explore endothelial cell motility in the context of the extending sprout stalk with and without genetic mosaics (Bentley, Franco et al. 2014). At the subcellular level, Hashambhoy et al. have used mass action kinetics models to explore VEGF diffusion, VEGFR dimerization, and surface signaling in simulated endothelial extensions (Hashambhoy, Chappell et al. 2011). Finally, Kleinstreuer et al. used a Cellular Potts Model to study vasculogenesis of the fetal liver with subsequent endothelial sprout

formation as a screening tool for high throughput toxicology analysis (Kleinstreuer, Dix et al. 2013). Though the specific approaches differ, these models all sufficiently capture and explore the possibility for a deterministic (or rule-informed) basis for cellular behaviors in sprouting angiogenesis at multiple resolutions. However, while these deterministic approaches are certainly valid, they do not compare their results to stochastic alternatives that may be similarly predictive of biological behavior.

Here, we describe a new agent based model (ABM) of angiogenic sprout initiation informed by high-resolution dynamic spatial and temporal data from the three-dimensional embryoid body (EB) model of embryogenesis (Kearney and Bautch 2003). Our ABM includes Notch1-DLL4 and VEGF signaling within and between cells to predict the frequency and location of endothelial sprout initiation events in image-based realistic multicellular networks and is validated against the data from the EB time-lapse movies. This is the first report of validating an ABM one-to-one with dynamic data of angiogenic sprouts. Further, we constructed a Monte Carlo simulation as a benchmark for asserting accuracy of sprout localization using purely stochastic methods. By comparing the rule-based ABM to the Monte Carlo we demonstrate that rule-based models more accurately simulate endothelial cell sprout initiation location. This combined approach supports the hypothesis that the location of sprout initiations in multicellular endothelial networks occur with in a deterministic manner, informed by underlying cell-signaling pathways.

## EXPERIMENTAL

### Embryoid body experiments

Maintenance and differentiation of mouse embryonic stem (ES) cells was described previously (Kearney and Bautch 2003) Stable expression of *PECAM-eGFP* in ES cell lines was previously reported (Kearney, Kappas et al. 2004) Real-time imaging of day 7-8 differentiating ES cell cultures was conducted as follows: confocal images were acquired at 4-10 min intervals for 16-20 hr with an Olympus FluoView FV1000 or FV10i system (full environmental controls) using either a 10× or 20× objective. At each location, a z-stack of 6-8 images was acquired with 4-6 microns between focal planes. These images were compressed post-acquisition into a single frame for each time point.

### Agent based model

**Agent and time definitions.** The ABM was built using Netlogo 5.0 and data were analyzed using MATLAB (Wilensky 1999). Each endothelial cell (EC) is spatially defined by eight membrane nodes (mNode) and a single centroid “nucleus” linked to each membrane node; the mNodes are connected to each other by membrane links (Figure 3.1A). The two-dimensional space occupied by cells is discretized into 10  $\mu\text{m}$  x 10  $\mu\text{m}$  pixels. During the course of the simulation the each cell adjusts its shape to approach an average endothelial cell surface area ( $EC_{SA}$ , Table 3.1); this is achieved by having links convey movement between their attached nodes – when a node is moved all linked nodes attempt to follow but may be hindered by other links. The time step of the simulation is 24 minutes, enough time to resolve micron-scale changes in cell position and still capture changes in protein levels (Barkefors, Le Jan et al. 2008) (Figure 3.2).

**TABLE 3.1: ABM PARAMETER VALUES**

Parameter	Description	Value	Reference
$EC_{SA}$	<i>EC Surface Area</i>	962E-8 cm <sup>2</sup>	(Adamson 1993)
$dsVEGFR1$	<i>Initial sVEGFR1 Secretion Rate</i>	2.8E-10 nmol cm <sup>-2</sup> · s <sup>-1</sup>	(Hashambhoy, Chappell et al. 2011)
$dmVEGFR1$	<i>Initial mVEGFR1 Insertion Rate</i>	2.8E-10 nmol cm <sup>-2</sup> · s <sup>-1</sup>	(Hashambhoy, Chappell et al. 2011)
$dVEGFR2$	<i>Initial VEGFR2 Insertion Rate</i>	8.4E-10 nmol cm <sup>-2</sup> · s <sup>-1</sup>	(Mac Gabhann and Popel 2004)
$dVEGF$	<i>VEGF Production Rate</i>	5.0E-10 nmol cm <sup>-2</sup> · s <sup>-1</sup>	(Hashambhoy, Chappell et al. 2011)
$dDLL4$	<i>Initial DLL4 Insertion Rate</i>	0	Estimated
$dNOTCH$	<i>Initial Notch Insertion Rate</i>	0	Estimated
$X_{min}$	<i>Minimum insertion rate</i>	1.0E-12 nmol cm <sup>-2</sup> · s <sup>-1</sup>	Estimated
$X_{max}$	<i>Maximum insertion rate</i>	1.0E-8 nmol cm <sup>-2</sup> · s <sup>-1</sup>	Estimated
$EC_{ctx}$	<i>Chemotactic Migration Rate</i>	30 μm · h <sup>-1</sup>	Estimated from (Liu, Ratner et al. 2007, Barkefors, Le Jan et al. 2008, van der Meer, Vermeul et al. 2010)
$\alpha$	<i>Notch Transfer Coefficient</i>	Model Specific	Parameter Fit

**Modeling molecular biology: VEGF and DLL4 signaling axes.** Each pixel stores concentration values of soluble VEGFR1 (sVEGFR1) and VEGF. sVEGFR1 is secreted by endothelial cells and in this simulation are produced by the mNodes. VEGF is secreted by cells throughout the tissue and therefore is produced by the pixels in this model. Diffusion is included using a simple distribution command – 25% of each diffusible species in each pixel is equally distributed among its eight neighboring pixels (Moore neighborhood).

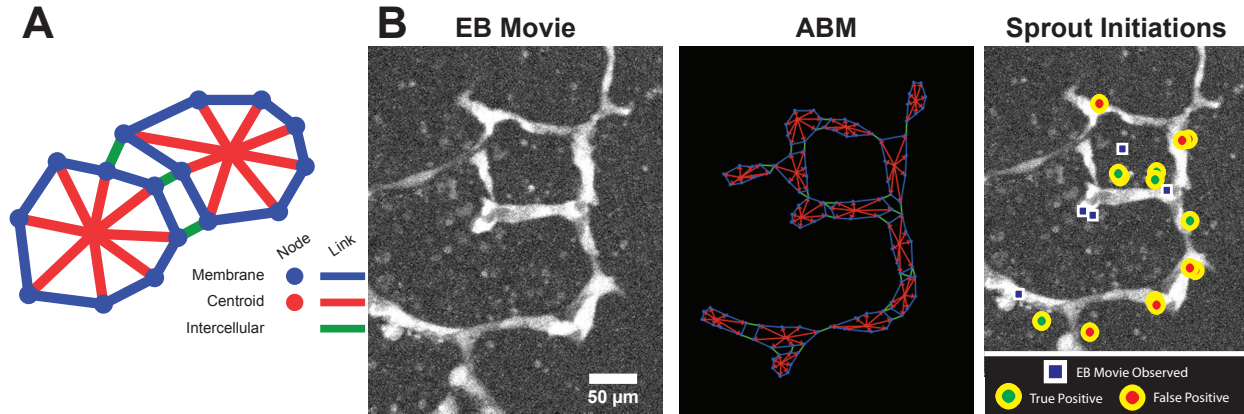


**FIGURE 3.1: CONSTRUCTION OF ABM FROM EXPERIMENTAL TIME-LAPSE MOVIES.**

Each cell is comprised of multiple agents including mNodes, nuclei, inter-, and intra-cellular links as shown in the cartoon (A). The embryoid body movie's initial frame is converted to an ABM representation to match EC locations. Simulation predictions of sprout initiations (circles) are then compared to observed sprout initiations from the EB movie (squares) and scored as true positive or false positive (B).

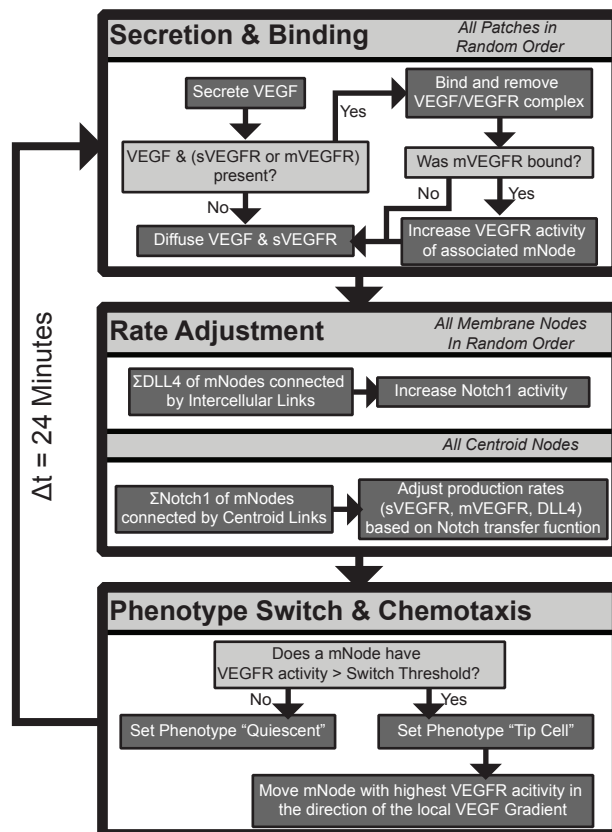


**FIGURE 3.2: ABM WORKFLOW.**

Each of the main subroutines occurs sequentially at every time step: secretion and binding, rate adjustment, and phenotype switching and chemotaxis.

Receptor binding kinetics are assumed to be 1:1 interactions between dimerized VEGFRs and dimeric VEGF (Mac Gabhann and Popel 2004, Vempati, Popel et al. 2011)– if a pixel contains VEGF and also includes either (1) an mNode with membrane-bound VEGFR1 (mVEGFR1), (2) an mNode with VEGFR2, or (3) sVEGFR1, then binding will occur until one of the pools (ligand or receptor) is completely depleted. For example, if there 10 molecules of VEGF and 100 available VEGFR2, the ABM will remove all VEGF from the pixel, while the local mNode reduces VEGFR2 to 90, and adds 10 phosphorylated VEGFR2 (pR2). When binding sVEGFR1 or mVEGFR1 there is no downstream function – receptor-ligand complexes are removed from the cell surface without further impact on signaling. These binding rules do not account for equilibria or mass action kinetics, favoring simpler, lower resolution molecular interactions at the multicellular scale. When VEGFR2 is converted to pR2 it increases the DLL4 production in that cell, following the formula:

$$DLL4_{t+1} = DLL4_t + (k \times pR2) - (k_{deg} \times DLL4_t) \quad (3.1)$$

where  $DLL4_{t+1}$  expression level is defined as the current amount of  $DLL4_t$ , increased by activation of pR2, and decreased at a constant degradation rate (Figure 3.2).

Based on what is known about the molecular biology of these families in endothelial cells, production rates of the VEGFRs are directly related to DLL4 expression on neighboring cells by the formula:

$$\dot{x}_{min} = x_{min} + (x_{max} - x_{min})e^{-\alpha \sum DLL4_{neighbors}} \quad (3.2)$$

where  $\dot{x}$  is the production rate per time-step of receptor  $x$ , and  $x_{min}$  and  $x_{max}$  are the minimum and maximum production rates, respectively. The DLL4 content of each neighboring cell (defined as having an intercellular link between mNodes) is summed and then scaled by the Notch1 transfer coefficient  $\alpha$ . When  $\alpha$  is 0 there is no information transfer between neighboring cells. Notch1 signaling alters the transcriptional regulation of VEGFRs, increasing the production of both sVEGFR1 and mVEGFR1 and

decreasing the production of VEGFR2 (Figure 3.2). VEGFR production rates are updated with each time-step.

Initial production rates for VEGF and VEGFRs are estimated based on literature-derived values (Table 4.1). In the case of Notch1 and DLL4, the initial values were set at 0 and instantiated based on Equation 3.2 and basal production rates. Minimum and maximum production rates ( $x_{\min}$  and  $x_{\max}$ , respectively) were estimated to be two orders of magnitude above and below the basal production rate.

**Phenotype switch from quiescent to tip cell.** When the pR2 levels on an endothelial cell in the model are above a particular threshold they undergo transition to the tip cell phenotype. Activated tip cells respond to VEGF signaling via chemotaxis towards the nearest source of VEGF. To calculate the direction of movement, the cell determines the mNode with highest pR2, and moves in the direction of the neighboring pixel with the highest VEGF concentration. This ability to sense VEGF concentrations at a distance of up to 10  $\mu\text{m}$  accounts for the effects of filopodial extension without explicitly modeling individual filopodia in the ABM. Endothelial cells in the tip cell state that drop below the pR2 threshold return to a quiescent phenotype.

**Rendering embryoid body data as ABM geometries.** Projections of confocal image stacks were converted to 16-bit intensity maps and loaded into the ABM using a custom image processing program written in Netlogo (Figure 3.1B). Loaded images were then converted to starting ABM configurations by manually selecting cell locations and then allowing for membrane shape change to approach the average endothelial cell surface area,  $EC_{SA}$ . Using the EB image as a guide, each cell mNode could be manually edited to better match the geometric configuration of the fluorescence intensity data. The EB image was then cleared and the resulting vessel geometry file exported for use in simulations (Figure 3.1B).

**Parameter estimation of Notch Transfer Coefficient.** From each of three EB movies a quadrant was selected and used as training data to determine the Notch Transfer Coefficient ( $\alpha$ , Equation 3.2) for

subsequent simulations. Simulation of sprouting using these starting configurations was performed over a parameter range from 0 to 2 in increments of 0.2, yielding a total of 16 different parameter values, each evaluated in 20 replicate ABM simulation runs. The number of sprout initiations over the course of each simulation was compared to raw sprout initiation counts from the paired EB movie and the best fit Notch Transfer Coefficient value was determined.

The Notch Transfer Coefficient value that generated the best fit from the parameterization was then validated in seven additional, independent EB Movie quadrants to confirm its accuracy and robustness across different initial network geometries. An example of true positive predictions as compared to false positives is shown in Figure 3.4B.

**Sensitivity analysis.** A local approach was used to evaluate sensitivity to the ABM Notch Transfer Coefficient: all other variables were held constant while sampling the parameter space of the Notch Transfer Coefficient between 0 and 2.0 using a 0.2 step size. A total of 20 simulations were run at each parameter value for each of the eleven total starting geometries defined by EB Movie quadrants.

**Monte Carlo analysis of stochastic sprouting without molecular control.** For each EB movie quadrant, Monte Carlo simulations were performed using Netlogo. Unlike the ABM, the Monte Carlo simulation randomly selects endothelial cells to undergo phenotype switch to tip cells (i.e. this method does not include the molecular mechanisms of VEGF and Notch1 signaling). The cells chosen were selected from a uniform distribution with replacement – this allowed the same cell to be chosen to be a tip cell more than once, as might occur in the ABM or EB model if a tip cell becomes quiescent and then reactivates at a later time point. The Monte Carlo simulations were not tasked with predicting the number of sprout initiation events; rather, the number of sprout initiation events (i.e. number of tip cell selection events) was drawn from a normal distribution with mean and standard deviation taken from ABM predictions. Each EB movie quadrant was evaluated over 1000 replicates.

The set of available sprout initiation locations available to the Monte Carlo simulation was bounded by the location of endothelial cells in the starting configurations of each EB movie quadrant. A performance index was defined as the difference between true positive frequencies in the ABM and Monte Carlo analyses – a positive value indicates better predictive performance of the ABM whereas a negative value indicates better predictive power of the Monte Carlo simulation.

**Genetic algorithm.** A genetic algorithm (GA) was applied to four parameters of the ABM (Notch Transfer Coefficient, tip cell activation threshold, sVEGFR1 production rate, and mVEGFR1 production rates) with the goal of maximizing the true positive frequency of the worst performing simulation, using the following objective function:

$$1 - X_{TP} = \mathcal{F}(x_1, x_2, x_3, x_4) \quad (3.3)$$

where  $X_{TP}$  is the true positive rate achieved by the ABM using a set of parameter values  $x_n$ . Minimum values for each parameter ( $x_n$  in Equation 3.3) were set to zero while maximum values were set to 100x the initial parameter value (Table 4.1). The simulation was run for 190 generations with 20 ABM replicates at each generation to determine an average true positive frequency.

**Statistical analysis.** Confidence intervals, Pearson's correlation, and partial least squares regression analysis were performed using GraphPad Prism version 5.0d for Mac OSX. Unless otherwise stated, significance was asserted at  $P \leq 0.05$ .

## RESULTS

**ABM Notch Transfer Coefficient parameter estimation.** Lacking a literature-derived value for the Notch Transfer Coefficient ( $\alpha$ , Equation 3.2), the key parameter governing the strength of Notch1 intercellular signaling, necessitated the use of parameter estimation. A single quadrant from each of three independent EB movies was evaluated over 16 different Notch Transfer Coefficient ( $\alpha$ ) parameter values (Figure 3.3D). As the strength of Notch lateral inhibition increases (increasing  $\alpha$ ), the number of sprout initiations occurring over the course of the simulations decreases, as would be expected. Above a value of  $\alpha = 1.6$  all three simulated movie quadrants converged to 0 sprout initiation events, effectively preventing any phenotype switching. Conversely, when the Notch Transfer Coefficient parameter was maintained at 0, no lateral inhibition was possible, and every cell in the simulation attempted to sprout. A Notch Transfer Coefficient parameter of approximately 0.6 resulted in agreement between the ABM predictions of sprout initiations and the observed sprout initiations in the three training quadrants (Figure 3.3D).

**ABM simulates sprout initiation frequency.** We sought to validate the Notch Transfer coefficient value of 0.6 established by parameter estimation with 3 training EB movie quadrants. To achieve this, 8 additional test EB movie quadrants were analyzed (Figure 3.3E). For all but one simulation (M3Q3), the observed number of sprout initiations in the corresponding EB movie quadrant fell within the ABM predicted 95% confidence interval of sprout initiations. This discrepancy for M3Q3 may be due to having a high number of sprout initiations occurring in close proximity in the EB movies – two sprout initiations that occur in close proximity may be underestimated by the ABM which predicts only one sprout initiation.

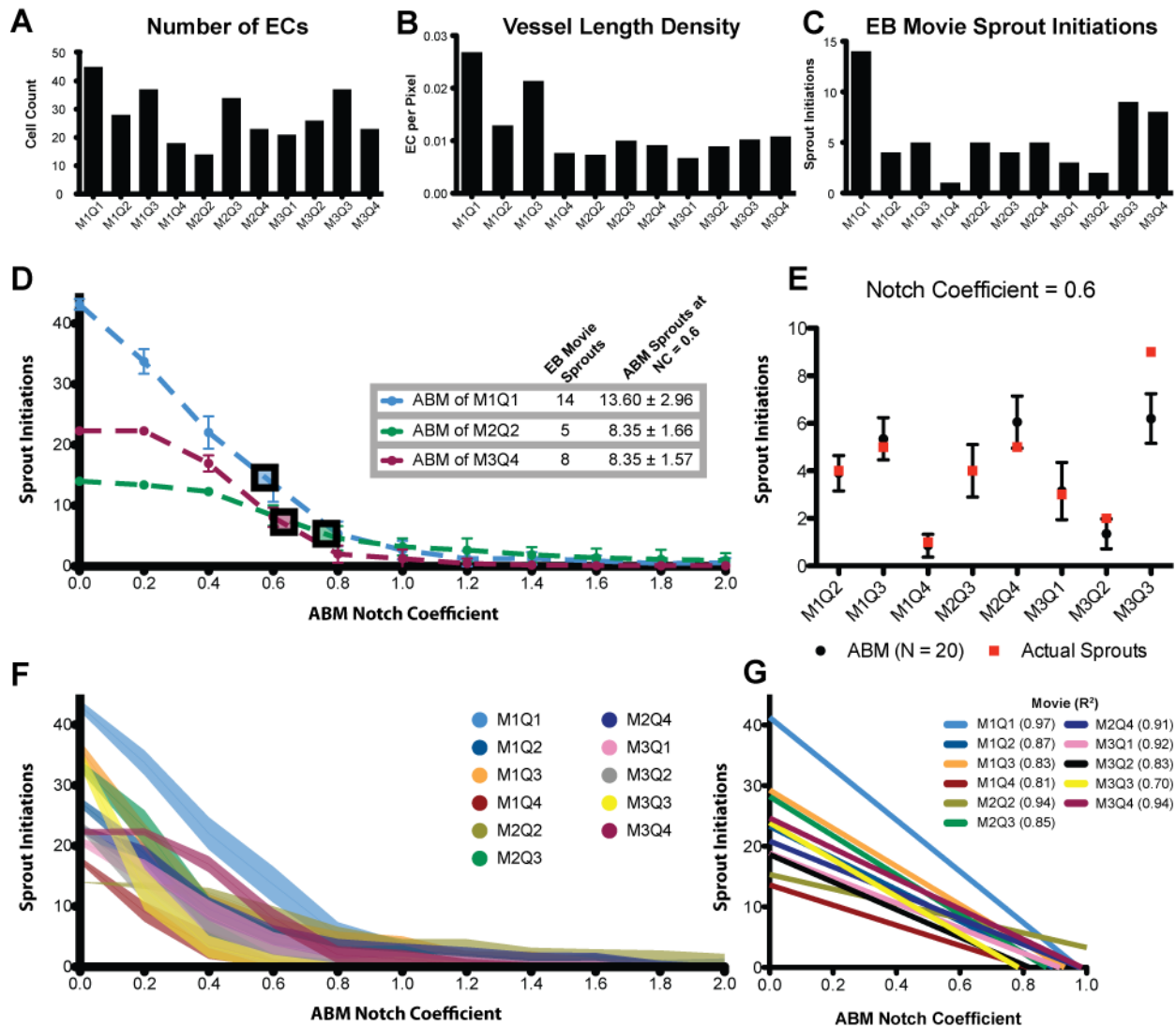


**FIGURE 3.3: PARAMETERIZATION AND VALIDATION OF ABM BASED ON A DIVERSE POPULATION OF EB MOVIES.**

The vessel network characteristics of each EB Movie are not uniform and represent a diverse sampling of possible EC network architectures (A-C). Using three EB Movies the ABM Notch Transfer Coefficient was parameterized to predict the number of sprout initiations (D). The Notch Transfer Coefficient value of 0.6 was then tested in all other EB Movies. The number of sprout initiations observed in the EB Movies (red squares) is shown to fall within the 95% confidence interval of ABM predictions (black circles and error bars, E). Performing the same sweep of the Notch Transfer Coefficient from 0.0 through 2.0 for all EB Movies demonstrates a similar trend, possessing a linear response region from 0.0 to 1.0 (shaded region is one standard deviation, F, G).

**Sensitivity of ABM to Notch Transfer Coefficient parameter.** All EB movie quadrants were evaluated for sensitivity to the Notch Transfer Coefficient. Across the range of tested parameter values ( $\alpha = 0.0-2.0$ ) all simulated vessel networks demonstrated a sprout initiation frequency that was inversely proportional to the Notch Transfer Coefficient (Figure 3.3F). Despite variations in vessel network morphology such as number of endothelial cells and vessel length density (Figure 3.3A-C), all simulated movie responses could be estimated using linear functions within the parameter range from 0.0 to 1.0 (Figure 3.3G) with coefficients of determination greater than 0.80 for all simulations except one (M3Q3,  $R^2 = 0.70$ ) and with non-zero slopes that were statistically significant ( $p < 0.05$ ). These data demonstrate sensitivity to the Notch Transfer Coefficient across all tested EB movie vessel networks.

**Use of a Monte Carlo model to evaluate accuracy of ABM-simulated sprout initiation locations.** The true positive frequency of ABM sprout initiation locations was scored using the methods described in Figure 3.1B. A Monte Carlo analysis was performed to determine the likelihood of correctly predicting sprout initiation locations purely by random chance, given the mean and standard deviation of paired ABM simulation sprout initiation events as input. The frequency of true positive events (determined by comparison to the observed sprout initiations in the EB movies) as generated by Monte Carlo simulation was compared to that of the ABM in the range of sprout initiation frequency when the Notch Transfer Coefficient parameter is set to 0.6 (Figure 3.4A).

Using the difference in true positive frequency as a performance index we demonstrated that the ABM has higher spatial accuracy in 7 of 11 starting geometries (Figure 3.4B). There appeared to be no correlation between performance index and initial conditions of the EB movie networks, such as number of sprout initiations, number of starting endothelial cells, vessel length density, or sprout initiation density (Figure 3.4C-F).

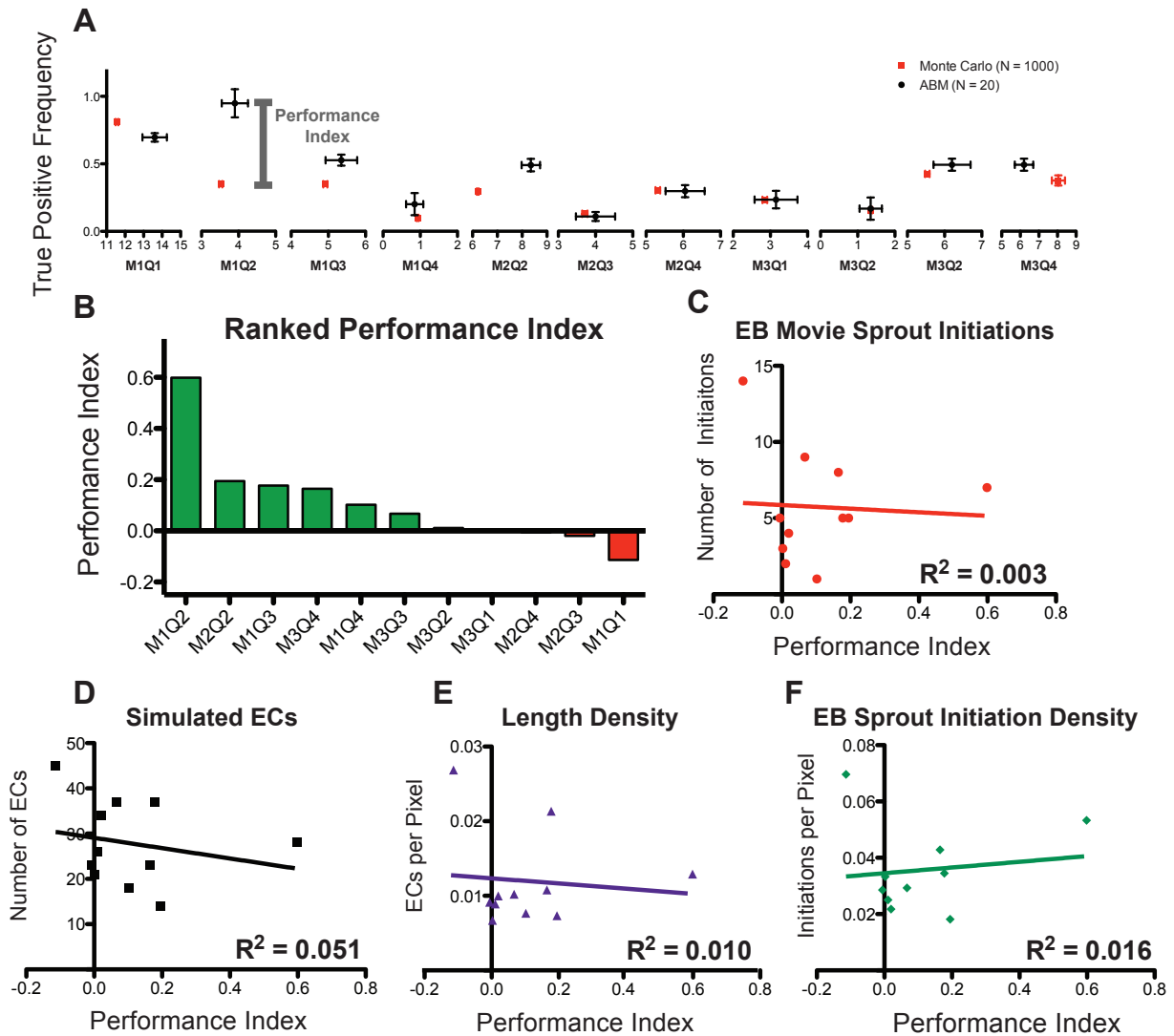


**FIGURE 3.4: COMPARING ABM AND MONTE CARLO PREDICTIONS OF SPROUT INITIATION LOCATIONS.**

For each movie, the Monte Carlo (red) and ABM (black) prediction of sprout initiations (x-axis) and true positive frequency (y-axis) were compared (SEM, A). A performance index, defined as the difference between ABM and Monte Carlo true positive frequency, was calculated. The ABM outperforms the Monte Carlo simulation in 7 out of 11 EB Movie simulations (Green Bars, B). C-F, Metrics of EC network structure from each EB Movie plotted as a function of the performance index; no correlation could be discerned.

**Unsupervised parameter identification in ABM using GA.** The parameter values used in the ABM simulations were literature-derived values (Table 3.1), with the exception of the Notch Transfer Coefficient, which was estimated (Figure 3.3). However, it is possible that a set of optimal parameters could improve the performance index of the ABM simulations. To explore this possibility, we used an unsupervised approach to search for a set of parameter values that could maximize the true positive frequency of the simulation with the worst performance index, M1Q1 (Figure 3.4B).

We used a GA to identify, in an unsupervised manner, the values of four key parameters (Notch Transfer Coefficient, tip cell activation threshold, sVEGFR1 production rate, VEGFR1 production rate, Equation 3.3) over the range from 0 to 100 times their original simulation values. As shown in Figure 3.5A the true positive frequency of the GA derived parameter values approach 40% accuracy. This rank ordering of all generations demonstrates four populations of outcomes: zero accuracy (no sprout initiations), low accuracy (less than 10%), medium accuracy (10%), and the highest accuracy (40%). Notably, these are all less than the original true positive frequency of the ABM (approximately 60%, Figure 3.4A).

Of interest, the GA obtained its best results when minimizing the activation threshold for phenotype switch from quiescent endothelium to tip cell. Conversely, reduced values of the Notch Transfer Coefficient ( $\alpha$ ) were associated with poorer performing populations (Figure 3.5C). Additionally, for the highest true positive frequency population (defined as >36%), the average value of  $\alpha$  was 0.63 (Figure 3.5B), in agreement with the parameter estimation performed in Figure 3.3.

The GA derived production rates of mVEGFR1 and sVEGFR1 were both approximately six orders of magnitude higher than the values used in Table 3.1, with the ratio of soluble to membrane bound production being 1.6 (data not shown).

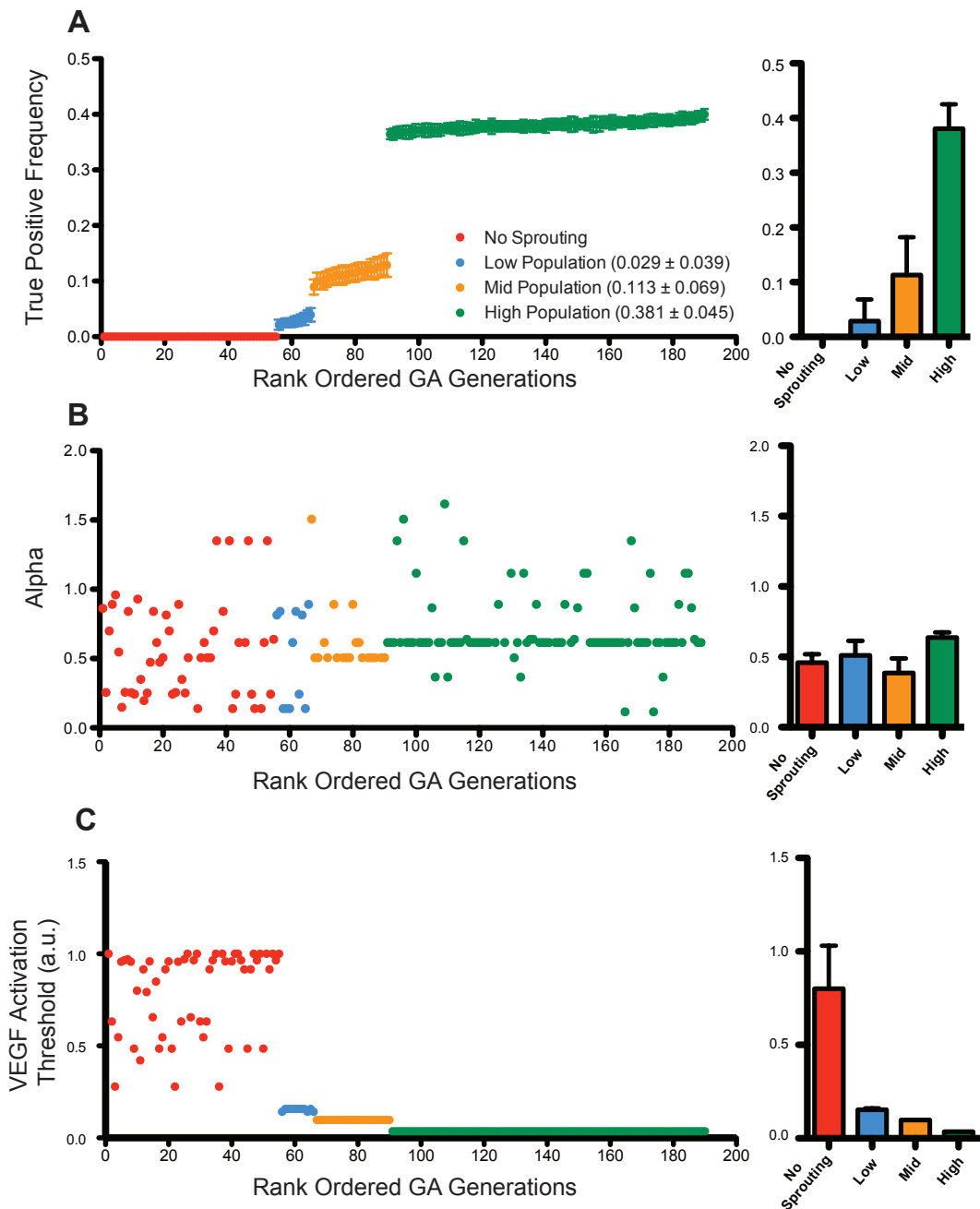


**FIGURE 3.5: PARAMETER OPTIMIZATION USING GENETIC ALGORITHM TO IMPROVE PERFORMANCE INDEX.**

The true positive frequency for each generation was plotted in increasing rank order to highlight four distinct outcome populations: no sprouting, low-, medium-, and high-populations (mean  $\pm$  SD, A). The Notch Transfer Coefficient ( $\alpha$ ) was plotted using the same rank-ordered generations and found to approach a value of 0.6 (B). To achieve improved true positive frequency the genetic algorithm attempted to minimize the activation threshold for phenotype switch from quiescent EC to tip cell (C).

## CONCLUSIONS

With the advent of innovations in intravital microscopy, such as light sheet microscopy, confocal, and multi-photon microscopy, imaging dynamic processes in living tissues and in *ex vivo* engineered tissue model systems has become more feasible (Fukumura, Duda et al. 2010, Giannouli, Chandris et al. 2014, Tanaka, Toiyama et al. 2014). These approaches generate data-rich movies that capture the dynamic behaviors of cells as they migrate within tissues and form multicellular structures, such as blood vessels (Brown, Campbell et al. 2001, Padera, Stoll et al. 2002, Jain, Munn et al. 2013). Viewing movies of tissue morphogenesis prompts the observer to ask a number of questions about underlying mechanisms, such as: are these behaviors defined by deterministic pathways? Are they the result of stochastic biological noise? Or, perhaps, are they controlled by some combination of both deterministic and stochastic influences? By combining computational modeling with confocal imaging we have attempted to address these questions in the context of angiogenic sprouting. We compared two different modeling approaches: (1) an ABM in which endothelial cell behaviors are governed by a set of deterministic rules and (2) a Monte Carlo simulation with purely stochastic cell behaviors, uninformed by signaling pathways.

In developing our ABM, we had to make several simplifying assumptions. In particular, diffusion and binding kinetics play important roles in signaling through the VEGFR family, including homo- and heterodimerization states that were not included in the ABM. Furthermore, VEGF itself was modeled as a single diffusive isoform with properties similar to the VEGF<sub>121</sub> splice variant that lacks a heparin binding domain (Ferrara, Gerber et al. 2003). We feel these assumptions are valid in the context of simulating the locations and frequencies of sprout initiations; however, simulating subsequent steps in sprouting angiogenesis, such as extension of the sprout away from its parent blood vessel, would likely require more high-resolution simulation of these molecular pathways, incorporating the physics of particle diffusion and mass action kinetics (Mac Gabhann and Popel 2004, Hashambhoy, Chappell et al. 2011,

Vempati, Popel et al. 2011). It is important to note that while the ABM simulations are driven by deterministic rules, diffusion of VEGF was modeled as a stochastic process, allowing for variation in receptor binding for each simulation.

Additionally, the ABM demonstrates sensitivity to the Notch Transfer Coefficient with a response region that can be approximated by a linear response with a non-zero slope. This permits tuning of the model to additional experimental conditions. For example, decreasing the Notch Transfer Coefficient parameter mimics inhibition of the Notch1-DLL4 pathway and produces increased sprout initiations as would be expected by small molecule inhibition (e.g. the gamma-secretase inhibitor DAPT) (Hellstrom, Phng et al. 2007, Benedito, Roca et al. 2009).

The Monte Carlo simulation, with no molecular mechanisms included, was constructed to compare a purely stochastic method of modeling endothelial cell behavior against ruled-based ABM-generated sprout initiation locations. Whereas we could directly compare the number of sprout initiations simulated by the ABM to the number of sprout initiations observed in the EB movies, there was no gold standard for evaluating the accuracy of sprout initiation locations. The Monte Carlo provided a benchmark for assigning a performance index (Figure 3.4B) of ABM accuracy as compared to the accuracy of random chance.

We demonstrate that the ABM accounting for Notch1-DLL4 lateral inhibition under control of VEGFR regulation is capable of simulating the frequency of angiogenic sprout initiations within the EB (Figure 3.3E). Despite disparate initial endothelial cell network configurations from one EB movie to the next (Figure 3.3A-C), the ABM predicted the correct number of sprout initiation events in all but one of the EB movie quadrants. Further, the ABM outperforms the Monte Carlo simulation of endothelial sprout initiation location in 7 of 11 EB movies (Figure 3.4B), strongly suggesting that deterministic rules are necessary for accurately simulating sprout initiation locations.

Using a GA, we attempted to improve the performance of an ABM with the lowest performance index as defined by the Monte Carlo. Four key parameters were selected and systematically tested by the GA to maximize the ABM true positive accuracy for that movie quadrant (Equation 3.3). Despite the use of this optimization algorithm, there was no improvement in the ABM's ability to accurately simulate sprout locations. This suggests that the literature-derived parameter values are better approximations of the underlying biological processes that they describe, as compared to the values obtained in an unsupervised manner by the GA.

Taken together, our use of a Monte Carlo simulation and a GA optimization algorithm to score ABM performance and attempt to improve upon that performance, respectively, lead us to conclude that inclusion of additional biological mechanisms in future iterations of the ABM may be necessary to improve its predictive capabilities. We speculate that the addition of new rules accounting for the presence of perivascular cells, for example, or that simulate VEGF molecular diffusion and receptor binding at the cell surface with higher spatial resolution, may extend the ABM's capabilities.

Others have also begun to explore how accurately angiogenic sprouting can be modeled by purely stochastic methods. Silva et al. recently investigated the frequency of sprouting events in a fibrin bead assay by comparison to a theoretical Poisson distribution and demonstrated that this probabilistic approach consistently underestimated sprout frequency (Silva, Eseonu et al. 2014). They concluded that enrichment with "efficient" sprouting endothelial cells was responsible for the discrepancy – indeed, isolation of a population of endothelial cells expressing low levels of CD143 and subsequent analysis in bead sprouting assays demonstrated significant increase in sprout frequency over both control (mixed) and isolated "inefficient" sprouting cells. Thus, after demonstrating that a probabilistic model insufficiently captured the features of fibrin bead sprouting, a new hypothesis – the existence of populations of endothelial cells with differential sprouting capacity – was generated and tested. Including this new deterministic cellular behavior (efficient or inefficient sprouting) into the theoretical

Poisson distribution generated sprout frequency predictions in agreement with experimentally observed results. Our present study is consistent with theirs, and suggests that probabilistic models that lack the inclusion of deterministic mechanisms may be insufficient for accurately simulating sprouting angiogenesis.

Our manuscript represents a first step towards greater understanding of sprouting angiogenesis through the integration of *ex vivo*, dynamic imaging techniques and computational simulations with both deterministic and stochastic methods. Our ABM uses a minimal set of rules to simulate, with considerable accuracy, the frequency and locations of endothelial sprout initiations in the EB during sprouting angiogenesis. By comparing ABM to Monte Carlo predictions, we were able to quantitate the spatial accuracy of the ABM and evaluate whether or not unsupervised parameter exploration improved its performance. Moreover, our simulations suggested that deterministic rules that account for key biological mechanisms are better able to recapitulate experimentally observed angiogenic sprout initiations than random chance, suggesting that deterministic influences predominate over stochastic influences in this setting of embryonic vascular development.

## **ACKNOWLEDGEMENTS**

We wish to acknowledge AHA grant 13PRE16580001, the Jefferson Trust Big Data Grant, the Cardiovascular Research Center Training Grant NIH T32-HL007284 (to JBW), NSF grant #1235244 (to SMP), NIH R01 HL43174 (to VLB), NIH grant R00HL093219, AHA grant 12BGIA12060154 and a Sloan Research Fellowship (to FMG), and NIH grants F32HL95359 and K99HL105779 (to JCC), for supporting this work.

# CHAPTER 4

**COMPUTATIONAL MODEL OF RETINAL  
ANGIOGENESIS SIMULATES RETINAL  
VASCULAR NETWORK MORPHOLOGY AS  
A FUNCTION OF PERICYTE COVERAGE.**

## **ABSTRACT**

Endothelial cells and pericytes act in concert to grow and maintain a healthy vascular network in the retina that is easily damaged by disruption of either cell type. Although endothelial cell signaling has been explored in detail, it remains unclear how pericytes function to modulate these signals that lead to a diverse set of vascular network geometries in health and disease. We have developed an agent-based model of retinal angiogenesis that incorporates both endothelial cells and pericytes to investigate the formation of vascular networks as a function of pericyte coverage. We use our model to test the hypothesis that pericytes interrupt Notch1-DLL4 signaling in endothelial cell-endothelial cell interactions. The ABM simulations that include pericytes are more physiologically accurate than simulations that lack pericytes and suggest that pericytes may influence sprouting behaviors through physical blockade of endothelial intercellular connections. This study supports a role for pericytes as a buffer to signal propagation for proper vascular network formation.

## INTRODUCTION

The developing murine retinal vasculature has long been a mainstay model for both studies that explore physiological and pathological angiogenesis (Fruttiger 2007). Mouse pups are born before their retinas are fully formed, with a stereotyped and conserved pattern of vascular patterning occurring over the course of approximately two weeks (Milde, Lauw et al. 2013). During the first 7 days of postnatal development, an angiogenic front of endothelial cells (ECs) grow along a template of astrocytes, beginning from the optic nerve and radiating outward to the distal retinal edge (Dorrell, Aguilar et al. 2002, West, Richardson et al. 2005, Scott, Powner et al. 2010). Over time, the angiogenic front advances, with the older, more proximal vasculature beginning a process of maturation – development of arterial/venous polarity, growth of vessels that penetrate deeper into the retinal tissue, and capillary rarefaction.

Throughout this process, pericytes (PCs), cells that enwrap endothelial cells, are maintained in close proximity to the EC network (Hughes 2008). Throughout the body, pericytes have been shown to affect vascular permeability (Armulik, Genove et al. 2010, Wisniewska-Kruk, Hoeben et al. 2012), capillary sprouting (Chang, Andrejcsk et al. 2013), capillary diameter (Durham, Surks et al. 2014), and leukocyte trafficking (Stark, Eckart et al. 2013). Loss of PCs in the eye plays a key role in the pathogenesis of several human eye diseases, notably proliferative diabetic retinopathy (DR), retinopathy of prematurity, and cancer-associated retinopathy (Ejaz, Chekarova et al. 2008, Cao, Xue et al. 2010, Hammes, Feng et al. 2011, Bandello, Lattanzio et al. 2013, Wu, Fernandez-Loaiza et al. 2013, Hartnett 2015). We have previously published evidence suggesting that an adipose-derived stem cell treatment may in fact replete PC loss in multiple murine models of DR, reducing capillary loss (Mendel, Clabough et al. 2013). Further, several groups have proposed an interplay between the Notch1-DLL4 EC signaling axis and PC function (Benedito, Roca et al. 2009, Simonavicius, Ashenden et al. 2012).

Despite the prevalence of retinal models of angiogenesis and a key role for PCs in retinal vascular development and health, much is still unknown about the function of PCs during vascular development. Specifically, the canonical Notch1-DLL4 signaling pathway in ECs has been studied in great detail (Noguera-Troise, Daly et al. 2006, Hellstrom, Phng et al. 2007, Chappell, Taylor et al. 2009, Chappell, Wiley et al. 2011), yet little has been done to elucidate how PCs may modulate that signaling axis. Computational models of the vascular endothelial growth factor receptor (VEGFR) and its effects on EC Notch1-DLL4 signaling have also been used to investigate endothelial behavior in angiogenic sprouts and vessel networks, but they do not explicitly account for putative effects of PCs during angiogenesis (Bentley, Gerhardt et al. 2008, Jakobsson, Franco et al. 2010, Hashambhoy, Chappell et al. 2011, Carlier, Geris et al. 2012, Kleinstreuer, Dix et al. 2013). Therefore, we have developed an agent-based model (ABM) for simulating EC and PC interactions at the angiogenic front during retinal vascular development.

Our ABM incorporates Notch1-DLL4 intercellular signaling between ECs, allowing for signal propagation throughout a multicellular network. EC directed chemotaxis is achieved through a stochastic model of VEGFR binding kinetics that accounts for competition between pro-angiogenic VEGFR2 and anti-angiogenic VEGFR1 (Fong, Rossant et al. 1995, Chappell, Taylor et al. 2009). A procedurally generated astrocyte network is included as the source of VEGF (West, Richardson et al. 2005, Fruttiger 2007, Scott, Powner et al. 2010). Our novel application of Minkowski functionals to both experimental and simulated angiogenic networks allows us to quantitatively compare the geometries of ABM-generated EC networks with images of actual angiogenic fronts taken from P3 murine retinas (Milde, Lauw et al. 2013).

Our results suggest that the presence of PCs alone, without any direct signaling to ECs, affects network formation. As compared to simulated networks comprised of only ECs, simulated networks with PCs more closely match the geometric properties of physiologic retinal vascular networks. Further, this effect cannot be replicated solely by increasing or decreasing the density of ECs in the network – PCs

must be present in the simulation to best match physiologic geometries. This supports a role for PCs as signaling “buffers” – spacing ECs to limit their intercellular contacts and preventing aberrant vessel growth due to inefficient or inaccurate intercellular communication.

## **METHODS**

### **Retinal Dissection and Immunohistochemistry**

All procedures were approved by the University of Virginia’s Institutional Animal Care and Use Committee (IACUC). Adult C57bl/6 mice were obtained from Jackson Laboratories and maintained in breeding pairs. At postnatal day 3 (P3) mouse retinas were dissected as previously described (Taylor, Seltz et al.). Briefly, eyes were enucleated and placed in a 0.4% paraformaldehyde solution for 7 minutes and then maintained in a phosphate buffered saline (PBS) solution for the remainder of dissection until slide mounting. While visualized using a Nikon SMZ1500 stereomicroscope, the sclera, lens, and hyaloid vasculature were removed and four relaxing incisions were made in a radially symmetric pattern around the posterior eyecup (Claybon and Bishop 2011). The remaining tissue was whole mounted on gelatin-coated slides.

Visualization of retinal vascular ECs and astrocytes was achieved by immunohistochemical staining. *Griffonia simplicifolia* isolectin B4 (IB4) preconjugated to Alexafluor-647 was used to identify ECs (Molecular Probes/Invitrogen/Life Technologies, Eugene, OR) (Gerhardt and Betsholtz 2003). Astrocytes were visualized by staining with a primary antibody against glial fibrillary acidic protein (GFAP, Dako/Agilent Technologies, Santa Clara, CA) (Fruttiger 2007, Milde, Lauw et al. 2013) and a secondary goat-anti-rabbit antibody conjugated to alexfluor 546 (Molecular Probes/Invitrogen/Life Technologies, Eugene, OR).

Retinas were permeablized with 1mg/mL Digitonin (Sigma-Aldrich, St. Louis, MO) in PBS for 1 hour followed by 3 washes with 1% bovine serum albumin (BSA) (Jackson ImmunoResearch, West Grove,

PA) in PBS for 10 minutes each. Blocking of non-specific binding was accomplished by a 1 hour incubation in 1% BSA-PBS. Primary antibodies were diluted in 1% PBS-BSA (1:200 IB4, 1:1000 GFAP) and allowed to incubate on retinas for 1 hour followed by 3 washes with 1% BSA-PBS for 10 minutes each. All of the preceding procedures were carried out at room temperature. Secondary antibodies for GFAP were diluted at 1:300 in 1% BSA-PBS and allowed to incubate overnight at 4°C. Finally, retinas were washed 3 additional times with 1% BSA-PBS for at 10 minute intervals before applying a 50/50 glycerol/PBS solution and sealing slides with cover glass. Samples were viewed immediately, with less than 24 hours between initial retinal harvest and confocal imaging.

### **Minkowski Analysis**

Image processing was performed using ImageJ and MATLAB. The Minkowski analysis is a method of quantitatively comparing images based on three geometric parameters: (1) area, (2) perimeter, and (3) Euler coefficient. Milde et al. have previously demonstrated the efficacy of the Minkowski analysis for identifying blood vessel patterns in the murine retina as a function of postnatal age (Milde, Lauw et al. 2013). We have adapted the technique to study both astrocytic and endothelial cell networks at the leading edge of the developing vascular front in both experimental and *in silico* angiogenic networks.

To perform a Minkowski analysis, the image (either immunohistochemical staining or ABM-derived) was first filtered through a binary mask. In the case of the astrocyte template studies, images were then skeletonized to reduce the network to a single pixel in diameter. The image area, perimeter, and Euler coefficient were then calculated as a function of the image dilation index (R). Through progressive image dilation a set of Minkowski functionals were generated that characterized the geometric properties of the original image. These image-processing steps are summarized in Figure 4.1. Area and perimeter values were normalized by the total area of the image to allow for comparison between images of different sizes and with different pixel dimensions.

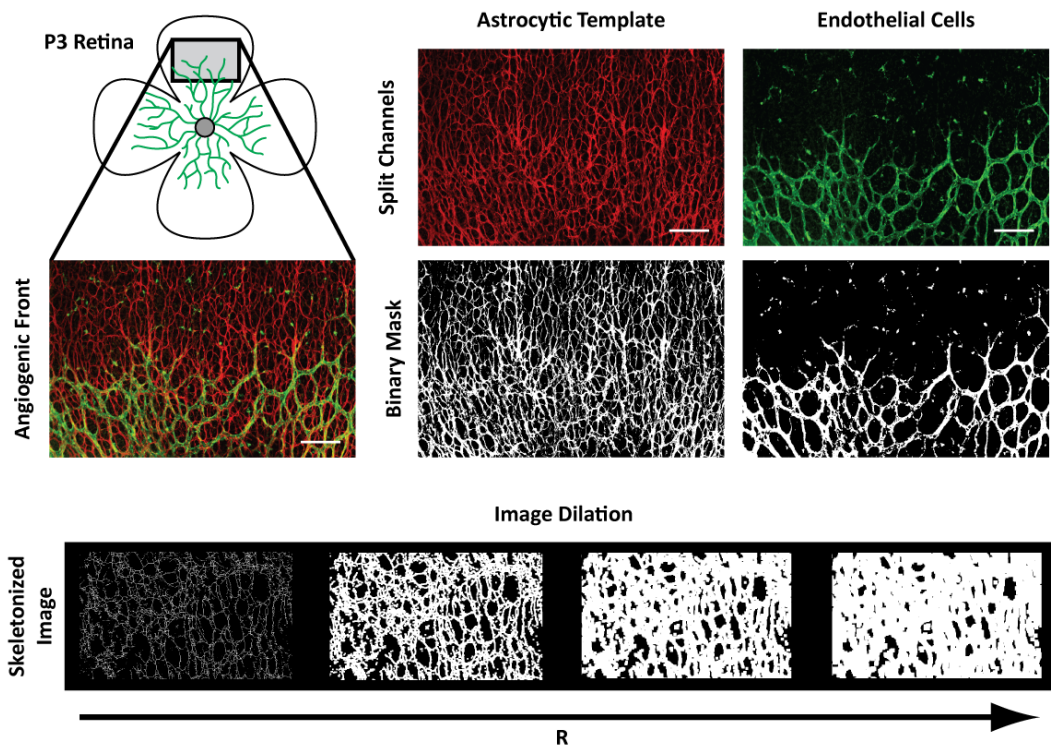


**FIGURE 4.1: IMAGE PROCESSING WORKFLOW FOR RETINAL MINKOWSKI ANALYSIS.**

Images of the extending vascular front of P3 retinas are collected (1 per retinal wing) to visualize astrocytes (red, GFAP) and endothelial cells (green, IB4). These channels are then separated and a binary mask is applied. For the astrocytic template, the image is then skeletonized prior to performing the Minkowski analysis. Minkowski functionals are a function of the image dilation value ( $R$ ). Scale bars = 100  $\mu\text{m}$ .

### ABM Temporal and Spatial Constraints

The total ABM simulation space was 0.087  $\text{mm}^2$  and is comprised of 5  $\mu\text{m}^2$  square pixels. Each EC and PC were assumed to maintain an average area of 500  $\mu\text{m}^2$  and therefore maintain a shape defined by 100 pixels (based on the assumption that in 2D only half of the total 1000  $\mu\text{m}^2$  surface area is present) (Adamson 1993). The ABM time-step was set to 10 minutes to simulate cell behaviors that take place on the time scale of days. As such, receptor binding and cell movement were iterated more than once per time-step. Specifically, cell movement occurred either 2 times (for quiescent ECs) or 4 times (for ECs with a tip cell phenotype). Receptor binding occurred with variable frequency each time step, with a

minimum of 20 stochastic binding iterations per pixel. Simulations were run for a total of 80 time steps, or equivalently 13.3 hours.

### **Astrocyte template generation**

Models were instantiated with a procedurally generated astrocyte template based on the Minkowski functionals of P3 murine retinal astrocytes. A variable number of starting pixel locations were randomly selected from the base of the model space. From each of these starting pixels, a new pixel “grew” within a 20 degree arc of the previous pixel’s heading, extending the astrocyte template skeleton. At any time, branching events occurred with probability ( $P_{\text{branch}}$ ), generating new paths. If forward movement converged upon an already existing path, the two branches converged and further progress was halted. The number of starting locations and  $P_{\text{branch}}$  were fit to generate an image with Minkowski functionals matching those of skeletonized astrocyte images from P3 murine retinas.

The finished ABM astrocyte template skeleton provided the only source of VEGF for the simulation with production and degradation rates of  $k_f$  and  $k_{\text{deg}}$ , respectively (Table 4.1). During each time-step, 40% of each pixel’s VEGF concentration was equally distributed within its Moore neighborhood (8 adjacent pixels) to simulate diffusion.

**TABLE 4.1: ABM PARAMETER VALUES**

Parameter	Description	Value	Reference
$EC_{SA}$	<i>EC Surface Area</i>	968 $\mu\text{m}^2$	(Adamson 1993)
$EC_{ctx}$	<i>Chemotactic Migration Rate</i>	30 $\mu\text{m} \cdot \text{h}^{-1}$	Estimated from (Liu, Ratner et al. 2007, Barkefors, Le Jan et al. 2008, van der Meer, Vermeul et al. 2010)
$\alpha$	<i>Notch Transfer Coefficient</i>	Model Specific	n/a
$\beta$	<i>Tip Cell Activation Threshold</i>	Model Specific	n/a
$k_{on}^{R2}$	<i>VEGF binding to VEGFR2</i>	1.0E7 $\text{M}^{-1}\text{s}^{-1}$	(Stefanini, Wu et al. 2008)
$k_{on}^{R1}$	<i>VEGF binding to VEGFR1</i>	3.0E7 $\text{M}^{-1}\text{s}^{-1}$	(Stefanini, Wu et al. 2008)
$k_{off}^{R2}$	<i>VEGF dissociation from VEGFR2</i>	1.0E-3 $\text{s}^{-1}$	(Stefanini, Wu et al. 2008)
$k_{off}^{R1}$	<i>VEGF dissociation from VEGFR1</i>	1.0E-3 $\text{s}^{-1}$	(Stefanini, Wu et al. 2008)
$k_{int}$	<i>Internalization rate of VEGFR2</i>	2.8E-4 $\text{s}^{-1}$	(Stefanini, Wu et al. 2008)

### Cell types and initial conditions

Three different experimental conditions were evaluated: simulations with both ECs and PCs, simulations with only ECs, and simulations sparsely populated with ECs. After generating the astrocytic template, ECs and PCs were seeded into the simulation within 65  $\mu\text{m}$  of the bottom to simulate the angiogenic front of a developing mouse retina. All simulations had at least 21 starting ECs. Simulations with ECs only had an additional 12 ECs (total of 32), while simulations with ECs and PCs had an additional 12 cells that each had a 25% chance of being PCs.

Finally, simulations with sparsely populated ECs followed the same rules except that the additional 12 cells each had a 25% chance to be removed. This third experimental condition with sparsely populated ECs was meant as a control for total EC number, matching the number of ECs in simulations with PCs – this allowed for separation of effects caused by purely reducing the EC count or by introducing PCs.

### Receptor Binding

In the ABM, ECs expressed two different forms of the VEGF receptor: VEGFR1 and VEGFR2. As was done previously by Mac Gabhann et al., receptor binding was approximated using a modified Gillespie algorithm for stochastic mass action kinetics (Gillespie 1977, Mac Gabhann, Yang et al. 2005). Reaction

rates were defined based on the number of VEGF molecules (V), VEGFR1 (R1), VEGFR2 (R2), VEGF-VEGR1 complexes (VR1), and VEGF-VEGFR2 complexes (VR2):

$$r_{on}^{R2} = \frac{k_{on}^{R2}}{vol \cdot N_A} \cdot V \cdot R2 \quad (4.1)$$

$$r_{on}^{R1} = \frac{k_{on}^{R1}}{vol \cdot N_A} \cdot V \cdot R1 \quad (4.2)$$

and normalized by the reaction volume (vol, one pixel of area  $5 \mu\text{m}^2$  with pseudo height assumed to be  $1 \mu\text{m}$ ) and Avogadro's number ( $N_A$ ). The receptor off rates were defined as:

$$r_{off}^{R2} = k_{off}^{R2} \cdot VR2 \quad (4.3)$$

$$r_{off}^{R1} = k_{off}^{R1} \cdot VR1 \quad (4.4)$$

The probability of receptor binding was thus a function of the on and off rates for both receptors at a given time, defined a  $P_{R1}$  and  $P_{R2}$  for receptors VEGFR1 and VEGFR2, respectively:

$$P_{R1} = \frac{r_{on}^{R1}}{r_{on}^{R1} + r_{off}^{R1}} \quad (4.5)$$

$$P_{R2} = \frac{r_{on}^{R2}}{r_{on}^{R2} + r_{off}^{R2}} \quad (4.6)$$

A random number ( $p_1$ ) was generated and compared to the probabilities of binding to determine the binding reaction outcomes:

$$\left. \begin{array}{l} R1 = R1 + 1 \\ VR1 = VR1 - 1 \\ R2 = R2 - 1 \\ VR2 = VR2 + 1 \end{array} \right\} p_1 > P_{R1} \wedge p_1 \leq P_{R2} \quad \left. \begin{array}{l} R1 = R1 - 1 \\ VR1 = VR1 + 1 \\ R2 = R2 + 1 \\ VR2 = VR2 - 1 \end{array} \right\} p_1 \leq P_{R1} \wedge p_1 > P_{R2}$$

$$\left. \begin{array}{l} V = V - 2 \\ R1 = R1 - 1 \\ VR1 = VR1 + 1 \\ R2 = R2 - 1 \\ VR2 = VR2 + 1 \end{array} \right\} p_1 \leq P_{R1} \wedge p_1 \leq P_{R2} \quad \left. \begin{array}{l} V = V + 2 \\ R1 = R1 + 1 \\ VR1 = VR1 - 1 \\ R2 = R2 + 1 \\ VR2 = VR2 - 1 \end{array} \right\} p_1 > P_{R1} \wedge p_1 > P_{R2} \quad (4.7)$$

Integration of new VEGFR2s and internalization of receptors or receptor complexes followed a similar algorithm whereby the insertion rate ( $sR$ ) was initially balanced with the internalization rate ( $k_{int}$ ) given 100 receptors at the cell surface:

$$sR = 100 \cdot k_{int} \quad (4.8)$$

This was then modified to reduce the insertion rate as a function of the Notch1 activity in the cell:

$$\widehat{sR} = sR \cdot \left(1 - \frac{Notch}{Notch_{max}}\right) \quad (4.9)$$

such that when Notch1 activity is maximal, no new VEGFR2 were expressed on the surface. Finally, the probability of incorporating a new receptor ( $P_{insert}$ ) was defined as:

$$P_{insert} = \frac{\widehat{sR}}{\widehat{sR} + k_{int} \cdot (R2 + VR2)} \quad (4.10)$$

and a random number ( $p_2$ ) was generated to determine the VEGFR2 turnover at the cell surface:

$$\left. \begin{array}{l} R2 = R2 - 1 \\ \text{or} \\ VR2 = VR2 - 1 \end{array} \right\} p_2 \leq P_{insert} \quad R2 = R2 + 1 \left. \right\} p_2 > P_{insert} \quad (4.11)$$

Note that there is an equal probability of removing either VEGFR2 ( $R2$ ) or a VEGF-VEGFR2 complex ( $VR2$ ) given that  $p_2 < P_{insert}$ . VEGFR1 was assumed to be maintained at a steady state concentration, such that the insertion and internalization rates are equal – thus, VEGFR1 surface turnover is not explicitly simulated.

### Intercellular Signaling

ECs were capable of communicating via a simulated Notch1-DLL4 mechanism, allowing for cells to modulate the insertion rate of new VEGFR2 molecules in their neighbors per equation 9. Each time step, ECs sum the DLL4 activity of their neighboring ECs (defined as any non-self EC within a Moore neighborhood) to determine their own Notch1 activity as defined by equation 12:

$$\text{Notch1}_{t+1} = \left( \alpha \times \sum \text{DLL4}_t \right) \quad (4.12)$$

where  $\alpha$  is the Notch transfer coefficient. This  $\alpha$  value scales the current DLL4 input from neighboring ECs such that increasing  $\alpha$  increases the Notch1 activity; conversely, a value of  $\alpha = 0$  decouples the system and simulates a loss of Notch1-DLL4 signaling.

### **Simulated Cell Behaviors**

The primary cellular behaviors and a process diagram of their implementation can be found in Figure 4.2. ECs and PCs both maintained cell contacts with cells that they were already in contact with. Importantly, loss of cell contacts was a condition for cell death – if ECs completely lost contact with any other ECs or PCs they underwent apoptosis. Similarly, if a PC lost contact with all neighboring ECs they also underwent apoptosis.

ECs were also capable of chemotaxis in response to VEGF. Specifically, when an EC moved it surveyed neighboring empty spaces (i.e. not already occupied by an EC or PC) and moved towards the one with the highest VEGF concentration. ECs transitioned from a quiescent to a tip cell phenotype if the number of ligated VEGFR2 molecules (VR2 in Equation 7) exceeded a threshold value of  $\beta$ . If VR2 dropped below  $\beta$ , the EC returned to a quiescent state. ECs with the tip cell phenotype had increased motility, which was simulated by doubling the number of migration attempts per time-step over quiescent ECs.

As cells migrated away from the initial starting positions, new ECs and PCs were added to simulate the growth of cells trailing the leading edge of the angiogenic front. The placement of these new cells followed the same rule set as the placement of the  $t_0$  cells, such as the probability of placing an EC or PC (in simulations that have both cell types). Probabilities of cell placement and model instantiation steps are summarized in Table 4.1 and Figure 4.2.

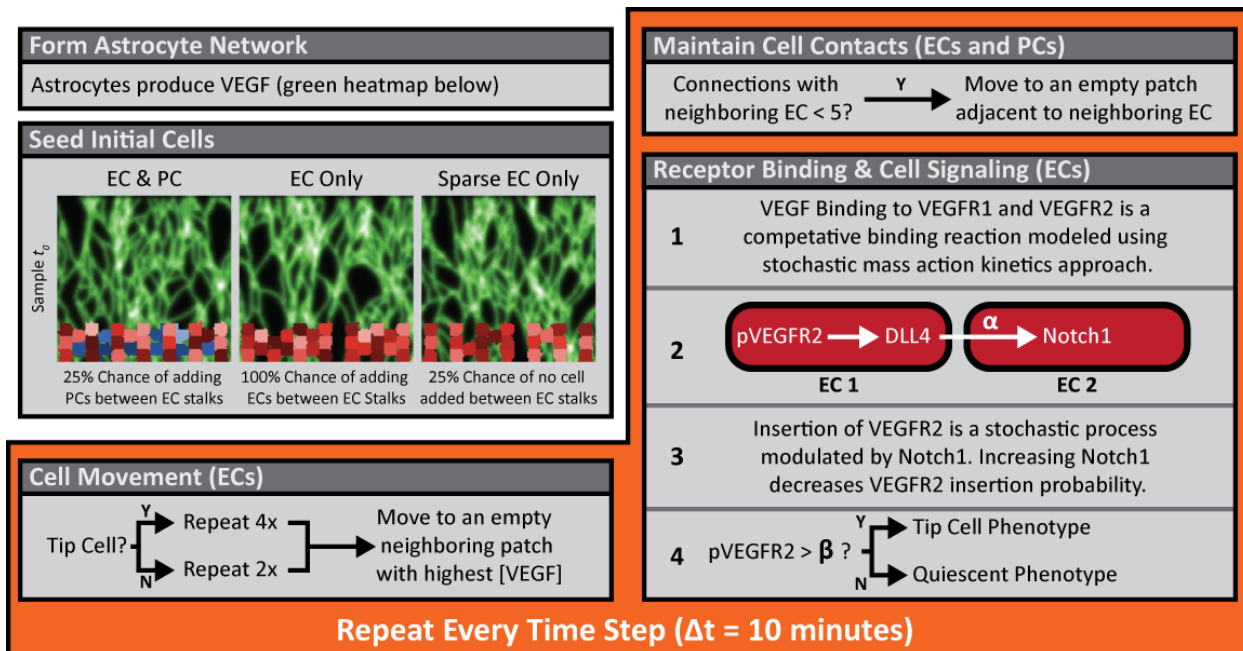


**FIGURE 4.2: RETINAL ABM PROCESS DIAGRAM**

Formation of the astrocyte network (Figure 4.3) and initial cell seeding are performed at the beginning of each simulation. Cell movement, maintenance of cell contacts, receptor binding, and cell signaling occur at each time step (highlighted in orange). Simulations are run for a total of 80 time steps after which EC locations are saved as tif images for Minkowski analysis.

### Statistics and Linear Regression

Confidence intervals, one-way analysis of variance (ANOVA), partial least squares regression analysis, and calculation of associated root mean squared error (RMSE) were performed using GraphPad Prism version 5.0d for Mac OSX and MATLAB. Unless otherwise stated, significance was asserted at  $P \leq 0.01$ .

## RESULTS

### ABM Astrocyte Template

Skeletonized immunohistochemical images of astrocytes labeled for GFAP (Figure 4.1) were compared to procedurally generated ABM astrocytic templates using their respective Minkowski functionals (Figure 4.3B). As  $P_{\text{branch}}$  increased, the ABM astrocyte networks became more highly branched, causing an increase in the total AREA covered by astrocytes. Conversely, increased branching reduced the total PERIMETER of the network, however this effect is comparatively small relative to the increase in AREA. Finally, the EULER NUMBER (e.g. measure of “laciness” or number of “holes” in the network) decreases with increased branching, confirming that more closed loops are generated in a more highly branched network.

These results were compared to the Minkowski functionals (AREA, PERIMETER, and EULER CHARACTERISTIC) obtained from harvested P3 retinal astrocyte networks (Figure 4.3B, black lines with grey fill). The skeletonized P3 retinal astrocyte networks closely followed the pattern of ABM networks with  $P_{\text{branch}} = 5\%$  according to the AREA functional. Conversely, the PERIMETER functionals for skeletonized P3 retina astrocyte networks were highly variable and did not converge until the dilation size (R) was approximately 15. Above a dilation size of 15, however, the P3 retina astrocyte networks again were most closely approximated by ABM astrocyte networks with  $P_{\text{branch}} = 5\%$ .

The EULER CHARACTERISTIC metric for actual P3 retina astrocyte networks was challenging to quantify below a dilation size of approximately 15 due to discontinuities in the skeletonized binary image. Because this metric is sensitive to the number of discontinuous objects, a certain amount of image dilation is necessary to generate a continuous network. Again, more negative values corresponded to more closed loops within the system. The P3 retina astrocyte networks at higher dilation sizes trended toward the ABM astrocyte networks with higher  $P_{\text{branch}}$ , although variability in the P3 retina data did not allow for a clear best fit.

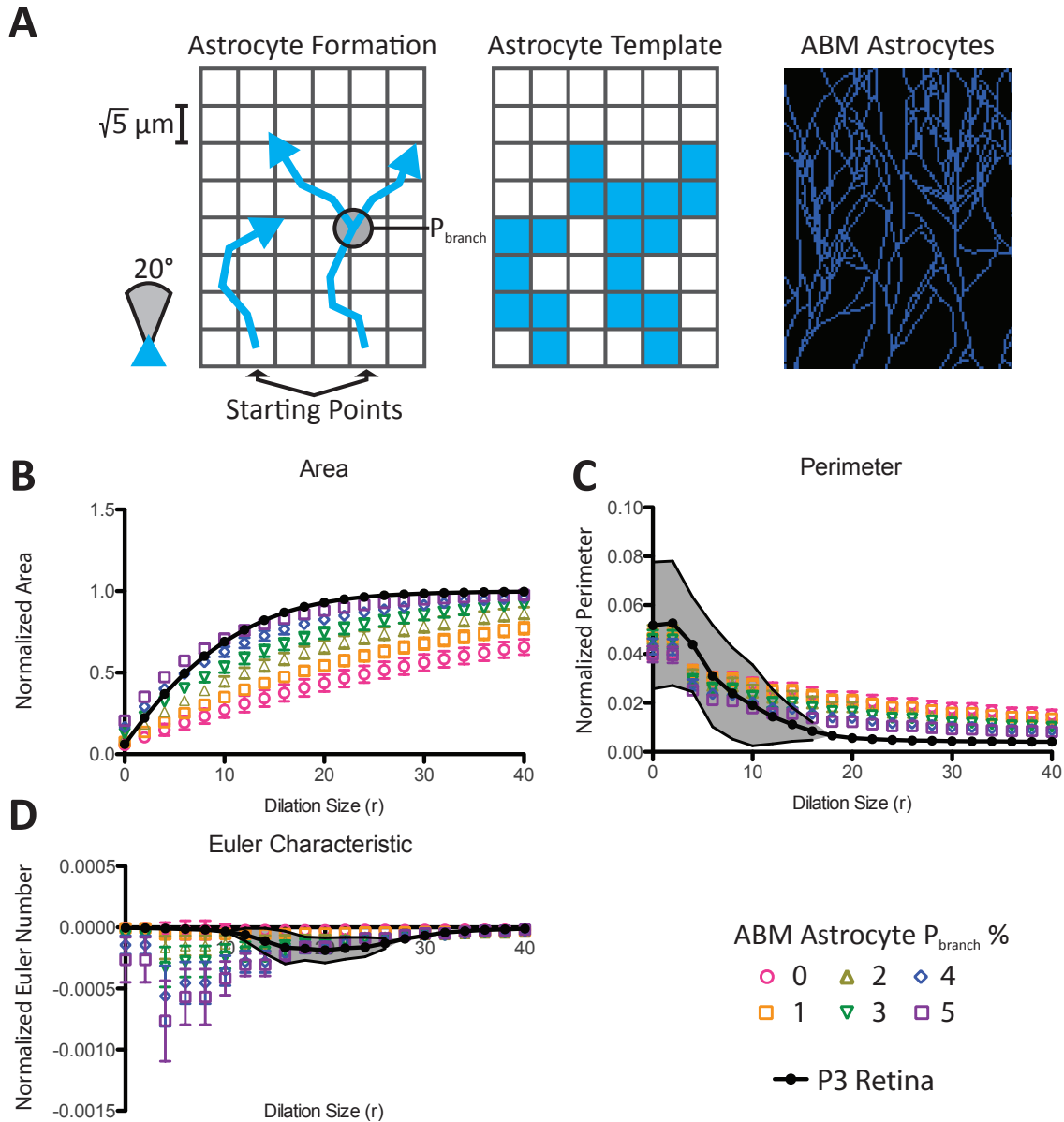


**FIGURE 4.3: DEVELOPMENT OF RETINAL ABM ASTROCYTE TEMPLATE**

The astrocyte template is instantiated at random starting points on the base of the simulation space and advances within a  $20^\circ$  arc of its current heading, with a possibility of branching defined by  $P_{branch}$  (A). This path is then converted into a discrete grid of  $5\mu\text{m}^2$  pixels for comparison to P3 retina astrocyte skeleton images (B-D). Data shown are Mean  $\pm$  SD (error bars for ABM data, shaded region for P3 retina data).  $N = 6$  retinal wing images,  $N = 100$  ABM simulation replicates.

Based on these results, a  $P_{\text{branch}} = 5\%$  was selected to generate the ABM astrocyte network templates for all subsequent simulations. ABM astrocyte networks generated using this probability closely matched the AREA and PERIMETER Minkowski functionals for actual P3 retina astrocyte networks and did not diverge significantly from the EULER CHARACTERISTIC.

### **Network Morphology Characterization**

A total of 160 different combinations of  $\alpha$  and  $\beta$  were tested with 10 replicate simulations being performed for each combination using each of the three experimental conditions. Recall that the astrocytic template and cell positions were stochastically generated, such that each replicate had a different starting configuration. This produced an ensemble of 4,800 ABM EC network images, each of which was characterized in an automated manner using Minkowski functionals. The Minkowski functionals for ABM-generated EC networks were compared to the Minkowski functionals generated for immunohistochemically stained P3 mouse retinas.

The similarity between the ABM-generated networks and real P3 retinas was evaluated by determining whether or not the Minkowski functionals for the ABM-generated networks fell within the 95% confidence interval (CI) of the Minkowski functionals for the actual P3 retinae. This similarity criterion allowed us to quantitatively assess the “performance” of the ABM; better performance was indicated by having more data points that fell within the 95% CI. ABM performance for all parameter combinations and all experimental conditions is shown in Figure 4.4, and an example of single parameter analysis is shown in Figure 4.5A. Observe that simulations with ECs and PCs greatly outperformed both other cell configurations when assessing the AREA functional (Figure 4A). Similarly, with respect to the EULER CHARACTERISTIC functional (a measure of closed loops within the network) simulations with both ECs and PCs also exhibited the best performance (Figure 4.4C). In contrast, ABM performance as characterized by the PERIMETER functional was not distinguishable between simulations

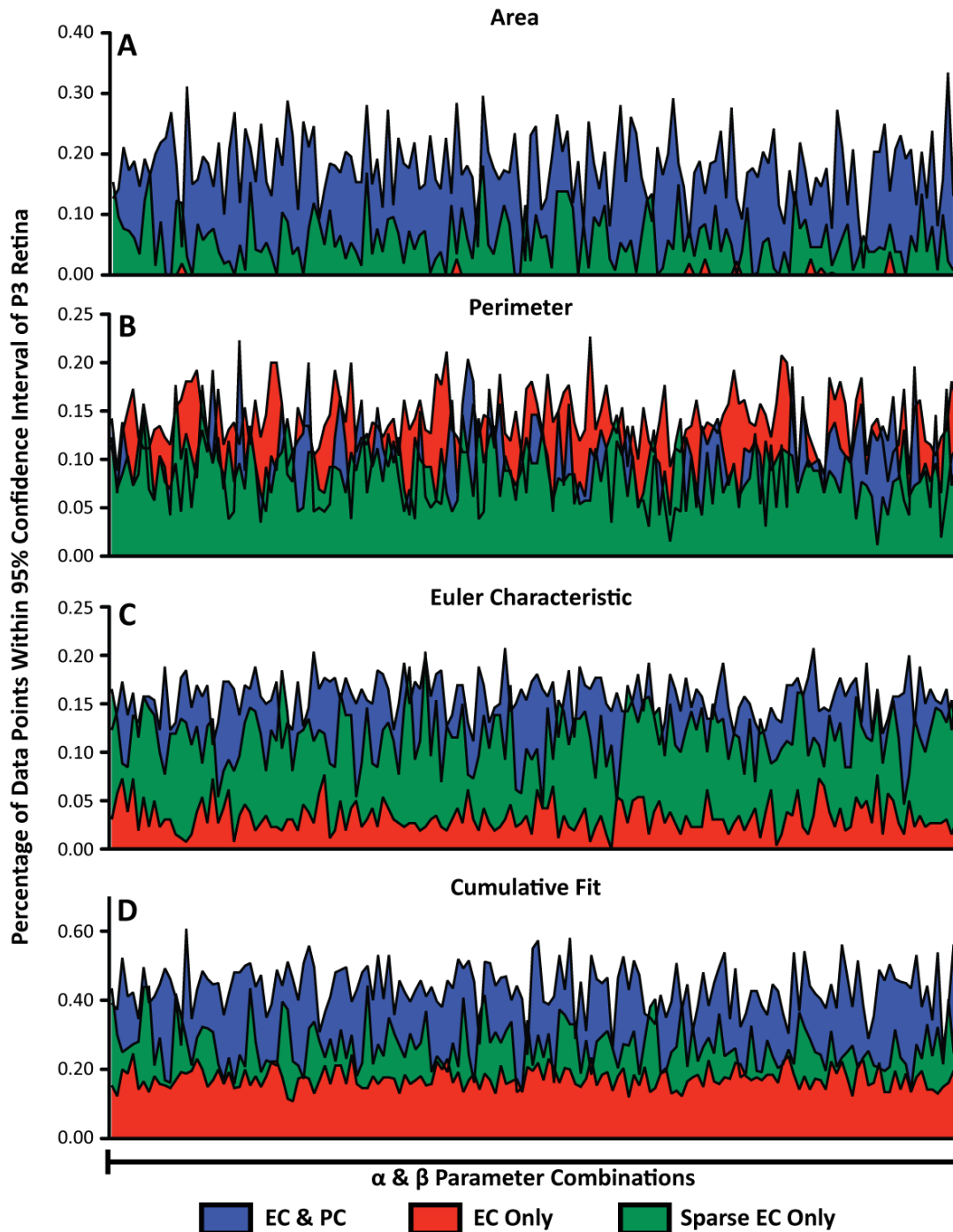


**FIGURE 4.4: ABM MINKOWSKI FUNCTIONALS COMPARED TO P3 RETINA ECs.**

Minkowski functionals were calculated from the positions of ECs at the final time step of the ABM for 160 combinations of  $\alpha$  and  $\beta$  parameters. The percentage of ABM-generated data points falling within the 95% confidence interval of the Minkowski functionals for P3 retinas is plotted as a function of parameter combinations for each of the experimental conditions (ECs & PCs, ECs only, or sparsely seeded ECs). Data shown for the AREA (A), PERIMETER (B), and EULER CHARACTERISTIC (C) are absolute percentages, while data for Cumulative Fit (D) is the sum of the former 3 (i.e. out of 300% rather than 100%).  $N = 10$  ABM simulations per parameter combination,  $N = 9$  P3 retinal wings.

with PC and EC, sparse EC, or EC only, and marginally better performance was seen in simulations with only ECs (Figure 4.4B).

Sparsely populated EC networks performed modestly across all Minkowski functionals. For only a few alpha and beta combinations did they outperform networks with both ECs and PCs, but for both the AREA functional and EULER CHARACTERISTIC functional, sparsely populated EC networks clearly performed better than more densely populated EC-only networks.

Finally, a cumulative performance score was generated by summing each of the Minkowski functionals (Figures 4.4D and 4.5C). This score mirrors what is described above, with ABM simulations of both ECs and PCs having the best overall performance, followed by sparsely populated EC simulations. We did not find a parameter combination for the ABM simulations with only ECs that performed better than the simulations with sparse ECs or both ECs and PCs.

### **Pericytes produce networks with greater branching and larger loops**

The slope of the Minkowski functionals provides additional insight into network morphology. As shown in an example analysis (Figure 4.5A,B), simulations with ECs and PCs have a more gradual rise in their AREA functional as compared to other simulation types. Across all 160 parameter combinations, simulations with ECs and PCs had a significantly smaller slope within the first 10 image dilations (ANOVA  $p < 0.01$ , average RMSE = 0.018, Figure 4.5D), which is characteristic of a network that, on the whole, has fewer intercellular spaces and less tortuosity.

Similarly, the PERIMETER functional demonstrates a shallower slope in the example case for the simulation with ECs and PCs (Figure 5A). This was, again, true across all parameter combinations, where simulations having both ECs and PCs had a significantly less negative slope compared to all simulations with only ECs (ANOVA  $p < 0.01$ , RMSE =  $9.98E-4$ , Figure 4.5E). A shallow slope for the PERIMETER functional is associated with more simple structures, lacking the complexity associated with vessel tortuosity.

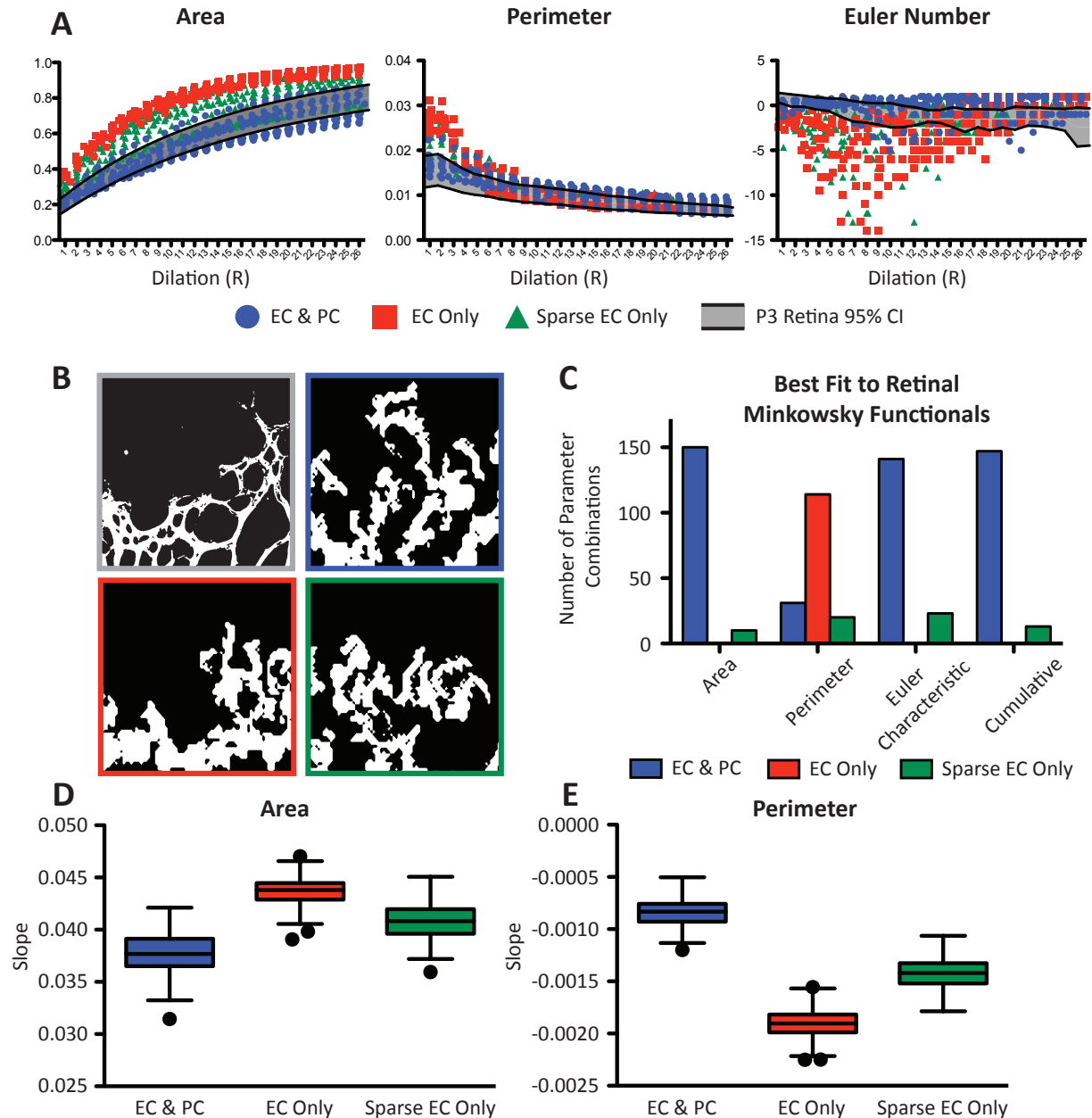


**FIGURE 4.5: AMB SIMULATIONS WITH PCs OUTPERFORM ALL OTHER SIMULATIONS FOR GENERATING EC NETWORKS WITH GEOMETRIES SIMILAR TO THOSE FOUND IN P3 RETINAS.**

Minkowski functionals for a single parameter combination ( $\alpha = 20$ ,  $\beta = 30$ , symbols) as compared to P3 retinas (shaded region) over a range of image dilation values (A). Binary images used for the Minkowski functionals shown in A, clockwise from top left: exemplar P3 Retina immunohistochemical stained ECs, ABM with ECs & PCs, ABM with sparsely populated ECs, ABM with only ECs (B). For all parameter combinations, the total number of times each experimental condition has the best performance (e.g. highest percent match to P3 Retinal 95% CI) as individual Minkowski functionals or cumulatively (C). Slopes for AREA and PERIMETER functions were significantly different ( $P < 0.01$ ) between all models (D and E).

Assigning an average slope value to the EULER CHARACTERISTIC functional was more challenging due in part to the high variability in some datasets, exemplified by the EC-only simulations (Figure 4.5A). This generated large residuals (average RMSE = 0.95 for the EULER CHARACTERISTIC functional) relative to the observed data, rendering associated linear fits unreliable. Large negative slopes for the EULER CHARACTERISTIC functional are indicative of high-density blind-ended loops, which was the trend for simulations with only ECs. Small positive slopes, as seen in the EC and PC simulations, suggest the presence of lacunae (vascular loops) of various sizes that gradually close as the image is dilated. Both of these trends were observed in the example EULER CHARACTERISTIC functional graph (Figure 4.5A); however, we were unable to identify any significant differences between ABMs with ECs only, sparse ECs, or PCs and ECs.

## DISCUSSION

In this paper, our objective was to develop a novel ABM of developmental retinal angiogenesis in order to test the hypothesis that pericytes can exert an indirect “buffering” effect on endothelial cells during capillary sprouting. Our ABM of murine retinal angiogenesis focused on cellular behaviors at the angiogenic front. Explicitly, we programmed receptor binding, intercellular communication via Notch1-DLL4 pathways, and subsequent chemotaxis that can be modulated by the phenotype of the EC (e.g. quiescent ECs migrate at half the speed of tip cell ECs that pass the VEGFR2 activation threshold,  $\beta$ ). Additionally, we incorporated PCs that serve as buffers to intercellular signaling – they themselves exert no direct effect on EC behavior, but they do limit the number of intercellular connections that ECs can make by physically providing a barrier to movement. Subsequent formation of cellular networks and geometric morphologies as quantitated by Minkowski functionals occur purely as a result of these rules without additional input.

Our study suggests that the mere presence of PCs as buffers to EC signaling and movement more closely recapitulates the actual geometry of the angiogenic front than ABM simulations with only ECs (either densely or sparsely populated). Importantly, this does not preclude direct effects of PCs on EC function and signaling – to the contrary, much has been written about the nuanced role that PCs play in maintaining EC function throughout the body (Díaz-Flores, Gutiérrez et al. 1991, Ejaz, Chekarova et al. 2008, Scheef, Sorenson et al. 2009, Armulik, Genové et al. 2011, Ribatti, Nico et al. 2011, Simonavicius, Ashenden et al. 2012, Kelly-Goss, Sweat et al. 2013). This ABM asserts a more basic question: can PCs play a role in EC network signaling through their presence alone? Furthermore, is this a function of PCs or simply a feature of vascular networks with fewer ECs? Indeed, our results support a role for PCs in supporting EC network formation that cannot be achieved simply by reducing the number of total ECs.

Our unbiased analysis using Minkowski functionals revealed that the microvascular network architecture of P3 retinas and ABM simulations with ECs and PCs agrees with our understanding of

vessel networks at the angiogenic front. As described by the slopes of the AREA and PERIMETER functionals (Figures 5D & 5E), these simulated vessel networks were characterized by having many branches and asymmetrically sized lacunae. Conversely, networks simulated by the EC-only ABM were thicker, more tortuous, and had more blind-ended branches. This description is consistent with the observed phenotype of pericyte loss in the retina, which is characterized by poorly formed vascular networks (Motiejunaite and Kazlauskas 2008, Mendel, Clabough et al. 2013, Wu, Fernandez-Loaiza et al. 2013, Hartnett 2015).

Simonavicius et al. have demonstrated that knockout of endosialin (CD248) in PCs leads to a defect in vascular regression and pruning despite normal recruitment to the EC network in the mouse retina (Simonavicius, Ashenden et al. 2012). Their study suggested that PC-derived endosialin binding to EC-generated (or EC-modified) basement membrane modulated VEGF binding to VEGFR2 – loss of the pathway promoted increased vessel density and loss of normal EC apoptosis during vessel maturation. Taken in context with our ABM findings, these studies suggest that the interplay between ECs and PCs during vascular development in the context of Notch1-DLL4 signaling may in fact be more important than previously thought.

That PCs exert no direct effects on EC signaling was a major assumption of our model. Pedrosa et al. have recently proposed a mechanism by which perivascular cells (PCs and vascular smooth muscle cells) directly interact with the Notch1 signaling axis of developing EC networks, although this was performed in skin wound healing assays, not in the developing retina (Pedrosa, Trindade et al. 2015). Specifically, overexpression of DLL4 led to an increase in PC coverage, decrease in vascular density, and a decrease in vessel leakage as measured by dye extravasation into the extracellular space. Additionally, we simplified EC function by only including signaling via VEGFR and Notch1-DLL4 pathways. The propagation of EC signaling at a network level through Notch1-DLL4 pathways has been described previously (Hainaud, Contreres et al. 2006, Hellstrom, Phng et al. 2007, Bentley, Gerhardt et al. 2008,

Benedito, Roca et al. 2009). Clearly, Notch1 signaling plays an important role in patterning the developing retinal vasculature. Several other key signaling pathways are implicated in retinal vascular development, including Notch4-EphrinB2 (Hainaud, Contreres et al. 2006) and the bone morphogenic protein family (BMP9 and BMP10) (Ricard, Ciais et al. 2012). However, given the current emphasis on VEGF and downstream signaling in treatment for proliferative diabetic retinopathy (Hammes, Feng et al. 2011, Bandello, Lattanzio et al. 2013, Bressler, Qin et al. 2013), we felt it prudent to focus on VEGF and Notch signaling. In our ABM, we also simplify the behaviors governing cell-cell contacts by including a rule that states that ECs and PCs must attempt to maintain contact with one another. Notably, this does not allow for the dynamics of EC cadherin expression that has recently been suggested as a mechanism for EC shuffling along angiogenic stalks (Bentley, Franco et al. 2014). Also, the ABM simulations all occurred on a planar surface in 2D – however, given the planar nature of the developing retinal vasculature (particularly at P3 when penetrating branches are rare) (Milde, Lauw et al. 2013), we feel that this and the preceding assumptions are valid for the present study.

The assembly of network structures from heterogeneous components is an ongoing area of intensive research across a broad array of disciplines. Indeed, Bentley et al. describe self-assembling systems ranging from robotics to vascular biology (Bentley, Philippides et al. 2014). In ABMs, the notion of self-assembly is commonly referred to as “emergent behavior” and describes the observation of a behavior that was not explicitly programmed into the model (Thorne, Hayenga et al. 2011, Borlin, Lang et al. 2014). This is a strength of so-called “bottom-up” approaches to modeling biological phenomena, allowing for a minimal rule set to generate a larger cohort of behaviors (Walpole, Papin et al. 2013). This work represents the first ABM specifically built to understand the interplay of ECs and PCs in the developing retina. Despite the many ocular diseases that are tied to the health of PCs, little has been done to computationally model the direct impact of perivascular cells on endothelial cells in retinal vascular networks undergoing angiogenesis. Our ABM simulations suggest that PCs can exert a direct

effect on EC network formation without explicitly modifying EC behavior through signaling pathways. This possible buffering effect should be taken into account in future studies of EC-PC interactions, particularly those involving active angiogenesis.

#### **ACKNOWLEDGEMENTS**

We wish to acknowledge AHA grant 13PRE16580001, the Jefferson Trust Big Data Grant, the Cardiovascular Research Center Training Grant NIH T32-HL007284 (to JBW), NSF grant #1235244 (to SMP), NIH 1R01EY022063 (to SMP), and the Hartwell Foundation (to SMP).

# CHAPTER 5:

## DISCUSSION AND FUTURE DIRECTIONS

### SYNTHESIS

The unifying theme of this body of work is applying computational modeling techniques to study the development of dynamic and geometrically heterogeneous multicellular networks. Specifically, I leverage ABM techniques to simulate angiogenesis *in vitro* and *in vivo* with a focus on understanding intercellular signaling through the VEGF and the Notch1-DLL4 axis. A key strength of ABMs is their capacity for representing and studying emergent phenomena – rather than explicitly programming network-level outcomes, I am able to instantiate rules that govern individual cells' behaviors and observe how those cells act in consort to form multicellular networks.

This work began with the presentation of a straightforward question: what governs the patterning of vascular networks? While a comprehensive answer remains elusive, I have begun the process of teasing apart the process using a bottom-up approach. By adding progressively more complicated components, I have built a pair of ABM simulation platforms that begin to address aspects of my original question. First, the Notch1-DLL4 and VEGF-VEGFR signaling axes sufficiently capture endothelial cell communication to inform spatially accurate predictions of tip cell initiations *in vitro* (Chapter 3). Certainly other signaling pathways are involved in the fine-tuning and regulation of vascular morphogenesis – yet a model accounting for these two interconnected canonical pathways remains uniquely sufficient for capturing this particular endothelial cell behavior. Second, in an ABM of retinal vascular development, I tested the hypothesis that pericytes affect capillary sprouting by serving as signaling buffers to endothelial intercellular communication (Chapter 4). Simulations lacking pericytes generated less accurate vessel geometries as defined by unbiased Minkowski functional analysis. This

quantitative approach to geometric analysis has allowed for direct comparison between physiologic images of P3 retinal angiogenesis that I obtained experimentally and ABM-derived vascular networks.

My simulations support a hypothesis that pericytes, through interrupting endothelial connections, buffer intercellular signaling and reinforce Notch1-DLL4 signal distribution to generate properly formed vascular networks in the developing retina. Note that this does not preclude other mechanisms of pericyte-mediated modulation of Notch1-DLL4 signaling in endothelial cells. Indeed, others have previously shown that pericytes can modulate Notch1-DLL4 signaling in endothelial cells both directly through intercellular connections (Pedrosa, Trindade et al. 2015) and indirectly through modifications of the basement membrane (Simonavicius, Ashenden et al. 2012). A logical next step will be to incorporate pericyte modulation of endothelial cell behavior through these mechanisms and see how they compare to the more simplified hypothesis that I chose to test.

The embryoid body ABM in Chapter 3 informed the development of the retinal ABM in Chapter 4 by supporting the hypothesis that rule-based simulations better capture endothelial sprout initiation behavior as compared to purely stochastic Monte Carlo simulations. Inclusion of Notch1-DLL4 signaling proved integral to predicting the correct endothelial sprout initiation locations, necessitating its inclusion in further studies. Indeed, as shown in Figure 5.2, Notch1-DLL4 activation patterns in the retinal ABM are more consistent with observed expression data (Hofmann and Luisa Iruela-Arispe 2007) when pericytes are included in the model (high DLL4 expression at the leading edge with higher Notch1 expression in neighboring endothelial cells). Further, exploration of the parameter space using a Genetic Algorithm approach (Figure 3.5) revealed sensitivity to both the Notch transfer coefficient ( $\alpha$ ) and the VEGF activation threshold ( $\beta$ ). Informed by these results, the retinal ABM output was not only analyzed as a function of pericyte coverage, but also as a function of these tunable parameters ( $\alpha$  and  $\beta$ , Figure 4.4).

Importantly, the embryoid body is generated from mouse embryonic stem cells that spontaneously differentiate, however only endothelial cells were observed in this transgenic mouse system because they expressed GFP under control of the lineage-specific marker PECAM (Figure 3.1B)(Kearney and Bautch 2003). The remaining space is, in fact, a milieu of other cell types, including pericytes (Magnusson, Looman et al. 2007), which could not be identified using dynamic confocal microscopy as they did not express a fluorescent reporter protein. Nonetheless, the effects of other cell types on sprout initiation (e.g. produced by heterotypic intercellular interactions with endothelial cells) may be implicitly accounted for by our parameterization of the Notch1 transfer coefficient ( $\alpha$ ). As such, the effect of pericytes on sprout initiation was not explicitly studied in Chapter 3, but their effects may still be partially captured by parameter estimation that was conducted for the ABM of the EB. However, this still may not account for all the effects of pericytes on sprouting in the EB. For example, it is hypothesized that pericytes must be displaced for underlying endothelial cells to initiate sprouting (Potente, Gerhardt et al. 2011) – if the locations of pericytes in the embryoid body movies could be identified and included in the ABM, it may have limited the number of locations where endothelial cells could sprout, thereby reducing false positive frequency.

This is a noteworthy distinction when considering the ABM of retinal angiogenesis presented in Chapter 4. Rather than implicitly modeling the effects of other cell types, we explicitly include pericytes and astrocytes as further constraints on endothelial cell migration and subsequent network formation. Including these additional rules did, in fact, produce a more accurate geometric representation of the retinal vasculature and allowed us to directly probe heterotypic intercellular interactions. As suggested by Chapter 3, including pericytes in the retinal ABM simulation improved model performance as compared to simulations without pericytes, and this allowed us to posit a novel hypothesis for the role of pericytes as signaling buffers that interrupt endothelial-endothelial intercellular connections.

In developing these models a major change to the ABM visualization and representation of cell types was performed (compare Figures 3.1B and 4.2). This adaptation was necessary to accommodate the types of questions each ABM sought to study. The embryoid body ABM focused on localizing sprouting initiation events, allowing for reshaping of the endothelial cell network without broad cell migration event (e.g. it did not generate endothelial stalks). To allow for a more dynamic cell migration simulation the retinal ABM was developed using a grid-based cellular geometry; while this limited the resolution of cell shape and discretized the positions cells could occupy it also allowed for improved control of cell migration behaviors. This shift in model architecture improved the ability to simulate

In summary, I have reviewed multiscale computational modeling across biological systems and presented two new ABMs of angiogenesis and vascular pattern development. In addition to suggesting a new testable hypothesis for how pericytes might influence endothelial cells during angiogenic sprouting, I have also developed new computational modeling techniques that have advanced the field of agent-based modeling. Specifically, I have: (1) developed new approaches for specifying ABMs based on images of vascular networks from both *in vitro* and *in vivo* experiments; (2) employed optimization strategies based on supervised and un-supervised methods; (3) simultaneously validated ABM predictions against experimental data and by comparing stochastic (e.g. Monte Carlo) and rule-based modeling approaches comparison to other modeling approaches; (4) employed functional analysis to directly compare ABM-generated cellular networks with my own library of developing retinal vascular networks (e.g. Minkowski Analysis); and (5) merged stochastic mass action kinetics of receptor binding with ABM spatial modeling (Gillespie algorithm for VEGFR binding). These efforts are a beginning – a series of steps towards a more multiscale understanding of vascular network development that spans molecular signaling to cellular behaviors to tissue-scale vascular network adaptations.

## **CONTRIBUTIONS AND EXTENDED APPLICATIONS**

### **Spatially accurate model of endothelial tip cell behavior**

I have generated an ABM that accurately predicts the frequency and location of endothelial tip cell extension events in the embryoid body model system. Previous work in this field has been limited to studying tip cell behaviors of smaller or less complicated (i.e. linear) networks of endothelial cells (Bentley, Gerhardt et al. 2008) or to simulations without explicit Notch1-DLL4 signaling (Kleinstreuer, Dix et al. 2013). My work extends this field by allowing for more complicated, physiologically mimetic endothelial cell geometries to be modeled and evaluated for tip cell behavior. Additionally, my model has the potential to be extended by incorporating additional signaling pathways or improving the resolution of current VEGF/VEGFR binding kinetics. Such additions would allow the ABM to potentially model more complicated tip cell behaviors, such as formation of endothelial stalks and shuffling of endothelial cells within the developing vascular network (Bentley, Mariggi et al. 2009, Bentley, Franco et al. 2014).

### **Directly matching biological data and using stochastic surrogates for validation**

A key innovation of the work in Chapter 3 is the marriage of high-resolution image sequences with an ABM. Through our collaboration with the Bautch laboratory (UNC Chapel Hill, Chapel Hill, NC), I was given access to time course data that was invaluable for generating my first ABM of tip cell behavior. Not only was this data necessary for designing accurate 2D embryoid body vessel networks, it also allowed for input-output matching – given a time course of data and the associated network of endothelial cells I could directly test the ability of the ABM to predict tip cell behavior. This method of matching imaging data to spatial modeling should act as a paradigm for future work – the strength of my ABM simulation was greatly enhanced by having high quality images and analysis to provide validation.

In my review of multiscale models, I discuss *in silico* perturbations and the “future” issues regarding parameter space exploration in models of complex systems that closely resemble their biological counterparts. This very issue became evident in my own work and required the generation of a unique performance index for quantifying the accuracy of ABM outputs. In seeking to evaluate the accuracy of my ABM I leveraged stochastic Monte Carlo methods to provide a baseline for performance. Thus, validation of my ABM required multiple approaches – spatiotemporal data and stochastic simulations were combined to demonstrate the accuracy of simulated tip cell behavior.

### **First ABM of retinal angiogenesis incorporating pericytes**

Many computational models of vascular development have been developed – some dealing with very specific physiology or pathophysiology (Plank, Sleeman et al. 2004, Tawhai, Burrowes et al. 2006, Carlier, Geris et al. 2012, Stapor, Azimi et al. 2012, Kleinstreuer, Dix et al. 2013), and others covering more broad endothelial cell biology (Mac Gabhann, Yang et al. 2005, Das, Lauffenburger et al. 2010, Hashambhoy, Chappell et al. 2011, Bentley, Franco et al. 2014). To date, no ABM of retinal angiogenesis has been developed incorporating pericytes or any other cell types that interact with endothelial cells. Furthermore, few ABM simulations actually incorporate perivascular cells of any type when studying endothelial cell behaviors. Through the development of this ABM of retinal angiogenesis, I have begun to explore the interplay between endothelial cell signaling and pericyte coverage.

### **Quantitative comparisons between ABM and retinal vascular networks**

Several quantitative methods have been employed to describe vascular networks – vascular length density, tortuosity, vessel diameter, etc. (Seaman, Peirce et al. 2011). These methods were developed specifically for studying labeled blood vessels and provide syntax for discussing the geometric qualities

of vascular networks across disciplines. However, these techniques are not optimized for high throughput image processing or analyzing general geometric properties of images.

I have employed Minkowski functional analysis to compare the geometric qualities of thousands of ABM-generated endothelial networks with those of P3 murine retinas. This method uses sequential image dilation to generate a series of Minkowski functional curves – area, perimeter, and Euler characteristic. These three parameters in ensemble quantitatively describe the features of an image and have been previously used to stage retinal vascular development (Milde, Lauw et al. 2013) as well as to classify small breast lesions on MRI (Nagarajan, Huber et al. 2013).

Using the Minkowski functionals, I demonstrated that ABM simulations containing pericytes more closely match the geometric properties of P3 retinal vascular networks than simulations containing only endothelial cells. As a control, to test if endothelial density was responsible for this result (simulations with or without pericytes had the same total number of cells, therefore EC-only simulations contained a higher density of endothelial cells), I examined networks that were sparsely populated with endothelial cells (i.e. same density as simulations with pericytes). While reducing the endothelial density did improve the accuracy of simulations, it still was not as accurate as simulations containing pericytes.

This analysis would have been computationally intractable to perform on an image-by-image basis as many studies of vascular networks are performed. Use of the Minkowski functionals proved to be an invaluable technique – one that should continue to gain in popularity as others become aware of the utility of morphological image analysis algorithms.

### **Pericytes as buffers for endothelial Notch1-DLL4 signaling**

A novel hypothesis generated by the ABM presented in Chapter 4 is that pericytes may provide intrinsic signal buffering in developing endothelial networks. As discussed, my ABM did not include any direct signaling between endothelial cells and pericytes – nevertheless, simulations with pericytes generated endothelial cell networks with geometric parameters most closely matching those of P3 retinal vascular networks. To my knowledge this is an untested hypothesis and may represent an alternative method for pericyte-modulation of endothelial cell signaling. This is an exciting theory that will require further investigation both experimentally and computationally.

## **FUTURE DIRECTIONS**

### **Extending ABMs to study additional stages of angiogenic sprouting**

A clear segue from the work presented in Chapter 3 would be developing an ABM capable of studying tip cell behavior subsequent to sprout initiation. Specifically, sprout guidance, extension, anastomosis (or retraction), and lumenization are key stages in sprouting angiogenesis that are also typically studied in isolation (Chappell et al., *Flt-1 (VEGFR-1) Coordinates Discrete Stages of Blood Vessel Formation*, in review). A comprehensive model of sprouting angiogenesis would account for all stages, following the initiation of tip extension through to the final fate of that particular endothelial branch.

### **Incorporating true multiscale simulations of angiogenesis**

As described in my review of multiscale modeling, different modeling strategies are better suited to simulating different scales of biology. An ongoing challenge in multicellular ABM simulations is the handling of subcellular processes – mass action binding kinetics, intracellular signaling, etc. This is partially due to computational limitations, as modeling the motion of all the individual molecules in the interstitial space of a tissue is both unrealistic and potentially uninformative. Rather, a method that performs these subcellular calculations when *necessary* and relies on lower resolution (spatial or temporal) calculations for relatively static regions would be ideal.

A solution would be a spatiotemporal adaptive mesh technique that uses high resolution modeling methods in regions where rapid dynamics are important while using computationally cost-effective methods in regions with slower dynamics. Zheng et al. have explored using a finite element adaptive mesh in a simulation of tumor progression – higher resolution calculations were made at the tips of angiogenic sprouts while quiescent regions were updated less frequently and with less spatial resolution (Zheng, Wise et al. 2005). This technique was accomplished based on a theoretical energy minimization – regions were modeled as having a weighted “tension” function based on surface

characteristics to define a spring energy constant. A region with high tension could be broken into smaller regions to minimize the system energy.

Admittedly, applying such a method would be a very large undertaking and would require collaboration with investigators having experience in adaptive mesh methods (or are at least familiar with the associated mathematical methods). I have previously attempted a first pass at incorporating multiscale modeling by combining my ABM of tip cell selection (Chapter 3) with a partial differential equations (PDE) model of VEGF diffusion and receptor binding developed by Hashambhoy et al. for studying local soluble VEGF gradient formation (Hashambhoy, Chappell et al. 2011). Using endothelial cell positions defined by the ABM, the PDE model generated high-resolution maps of VEGFR2 activation on the endothelial cell surface. These receptor activation states were then translated into changes in DLL4 expression and subsequent Notch1 activation to provide transcriptional regulation and chemotactic cues.

This initial test proved promising but required a great deal of hands-on observation and file handling to generate an closed-loop multiscale model of sprouting angiogenesis (e.g. a Type 2 Multiscale Model as defined by Figure 2.2). More recently, we have used this connection to generate a monodirectional multiscale model (e.g. a Type 1 Multiscale Model as defined by Figure 2.2) whereby endothelial cell geometries were generated by the ABM and fed into the PDE model for exploration of VEGF binding to VEGFR2 in multicellular networks with and without expression of soluble VEGFR1. This data is as yet unpublished, but will be appearing in a Chappell et al. publication entitled “Flt-1 (VEGFR-1) Coordinates Discrete Stages of Blood Vessel Formation” (Figure 5.1).

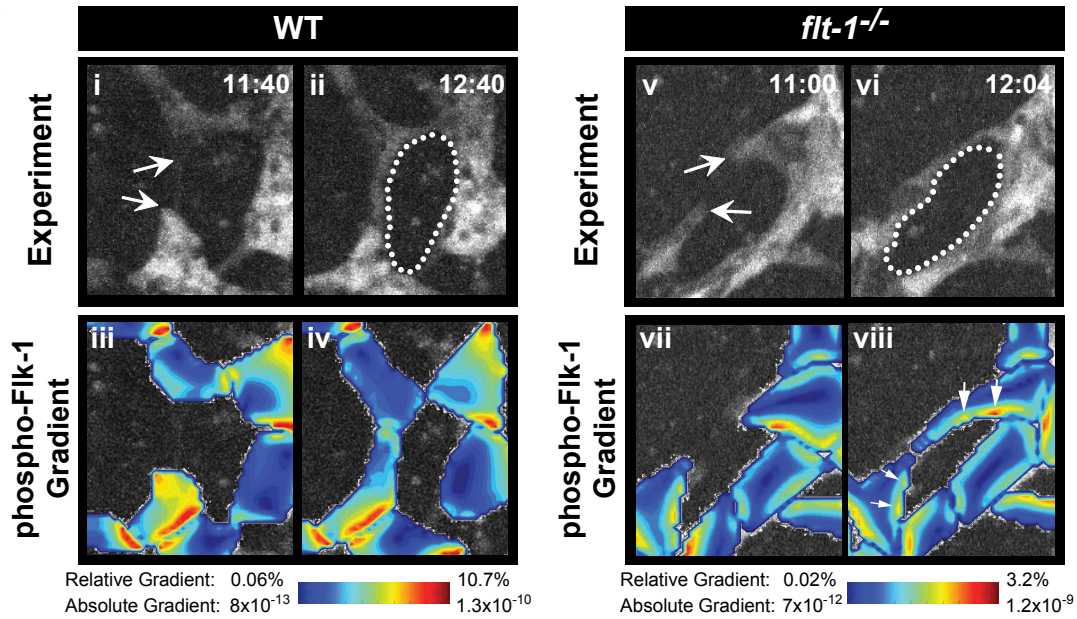


**FIGURE 5.1: MULTISCALE MODELING USING ABM OF TIP CELL SELECTION FOR ENDOTHELIAL CELL PLACEMENT.**

Figure adapted from Chappell JC et al. *Flt-1 (VEGFR-1) Coordinates Discrete Stages of Blood Vessel Formation*, in review. Endothelial cells were mapped from embryoid body images (Experiment panels i, ii, v, and vi) using the techniques outlined in Chapter 3. These ABM-generated endothelial positions were then used by F. Mac Gabhann to define boundary conditions for a PDE reaction diffusion model of VEGF receptor binding. A gradient of VEGFR2 activation (phospho-Flk1) across the endothelial cell surface could then be generated with and without soluble VEGFR1 production (*flt-1*). These data highlight increased VEGFR2 activation in the interior of closed loops (arrows, panel viii) that may contribute to vessel collapse in the *flt*<sup>-/-</sup> embryoid body model.

I hope to continue this work through ongoing collaboration and exploration of multiscale modeling techniques. A combined approach that strategically uses subcellular simulations to inform multicellular ABMs would be a truly unique contribution to the field of vascular biology.

### Exploring the effects of pericytes on Notch1-DLL4 signaling in endothelial cells

In Chapter 4, I presented an ABM that suggests the novel hypothesis that pericytes limit the number of endothelial cell-endothelial cell adhesions, interfering with Notch1-DLL4 signaling, and that this is the mechanism for improved ABM accuracy versus simulations with only endothelial cells. These ABM simulations set the stage for interesting follow-up work that would further test the hypothesis that pericytes affect EC-EC signaling through a signal “buffering” mechanism. Specifically, a study of signal

propagation is a clear next step to determine if the distribution of Notch1 activity in endothelial cell networks is affected by the presence or absence of pericyte coverage. Figure 5.2 shows images from the simulations presented in Chapter 4 that correspond to VEGF, VEGF-VEGFR2, Notch1, and DLL4 values distributed throughout the endothelial cell networks. Note that in the simulation with pericytes there is a clear increase of DLL4 along extending ECs (arrowhead, Figure 5.2C). A neighboring cell has relatively higher Notch1 signal (double arrow, Figure 5.2B) compared to nearby cells, as would be expected based on observations of Notch1-DLL4 patterning in the retina. Conversely, an example EC-only network demonstrates very high Notch1 activity at the leading edge (Figure 5.2F), which is not typical patterning in the developing retina. Further investigation of the patterns of expression and/or phosphorylation/activation of these molecules as a function of pericyte coverage would more directly test my proposed buffering hypothesis.

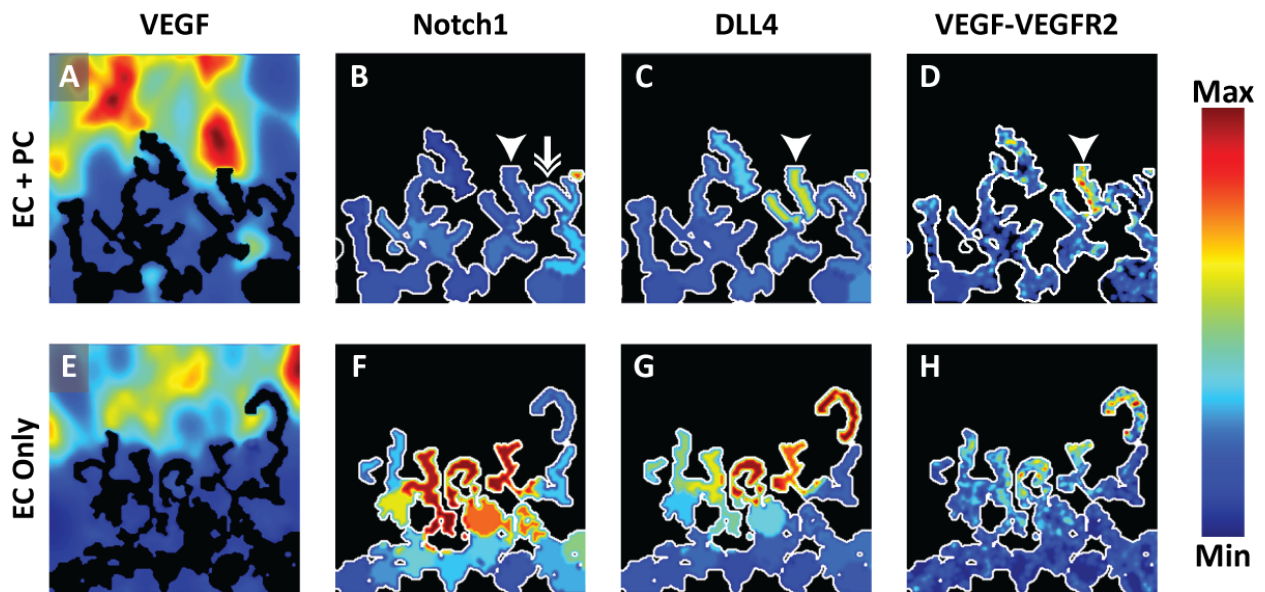


**FIGURE 5.2: SAMPLE HEATMAPS OF SIGNALING MOLECULES GENERATED BY THE RETINAL ANGIOGENESIS ABM.** Distribution of intercellular signal intensity, VEGF concentration, and VEGF-VEGFR2 receptor ligand complexes for ECs in simulations with (top) and without (bottom) pericytes. Levels of signaling molecules are shown on a relative scale for (A,E) VEGF, (B,F) Notch1, (C,G) DLL4, and (D,H) VEGF-VEGFR2. Endothelial cells are masked in black in (A,E) and outlined in white in (B,C,D,F,G,H). Arrowhead points to an EC with high VEGF-VEGFR2 levels (relative to neighboring cells) and a correspondingly high relative DLL4 level. The neighboring EC (double arrowhead) exhibits increased relative Notch1 levels as a result.

As this presents a key question in angiogenesis, I have envisioned a series of experiments to study these phenomena. A simple first step would be to evaluate the pattern of Notch1 activation and DLL4 expression in the developing retina with and without pericyte coverage using immunohistochemical staining and confocal microscopy. Typically, Notch1 activity is highest in the angiogenic front and is often seen at vessel bifurcations whereas DLL4 expression is more distributed, but its expression is highest in tip cells and stalk cells at the angiogenic front (Hofmann and Luisa Iruela-Arispe 2007). Disruption of pericyte recruitment to blood vessels is a hallmark of the endothelial-specific KO of platelet-derived growth factor-B (PDGFB) (Bjarnegard, Enge et al. 2004). Therefore, a study of P3 retinas from the EC-PDGF KO mouse may reveal a redistribution of Notch1 and DLL4 patterning not previously described. For example, retinas lacking pericyte coverage and immunohistochemically stained for DLL4 might demonstrate increased overall DLL4 expression at the angiogenic front with subsequent increases in Notch1. Alternatively, loss of pericyte buffering may lead to overall diminution of DLL4 and Notch1 expression as such a highly connected endothelial network may be unable to properly establish and reinforce a stable signaling pattern.

Results from such a study would be difficult to attribute purely to a signal buffering mechanism, however they would support the hypothesis for pericyte-mediated modulation of Notch1-DLL4 signaling in endothelial cell networks. For example, completely ablating the pericyte population might affect basement membrane composition and indirectly alter endothelial network geometry, independent of a direct effect on the number of endothelial cell intercellular adhesions. Simonavicius et al. have demonstrated that pericyte-derived endosialin interacts with endothelial-derived basement membrane components to maintain normal vascular pruning – loss of endosialin resulted in increased vessel density but not a reduction of pericyte recruitment (Simonavicius, Ashenden et al. 2012). Furthermore, pericytes may also *directly* interact with endothelial Notch1-DLL4 signaling – Pedrosa et al. have shown

that DLL4 may in fact play a role in properly recruiting pericyte to the endothelium (Pedrosa, Trindade et al. 2015).

Nevertheless, a thorough exploration of network-level Notch1-DLL4 signal transduction patterns as a function of pericyte coverage have not yet been evaluated. Naturally, incorporation of these signaling pathways into the existing ABM simulation of retinal angiogenesis would provide an alternative means for generating a hypothesis that combines active and passive pericyte modulation of Notch1-DLL4 signaling.

## CONCLUSION

A seemingly straightforward question – what governs the patterning of vascular networks? At least, I believed it to be a simple question when I was staring at blood vessels under a microscope. From there I have spun a tangled collection of experiments and computational methods in an effort to better understand a fundamental biological process while contributing to the ever-growing body of vascular biology knowledge.

I have demonstrated that ABM techniques can accurately simulate endothelial cell behavior during angiogenesis. Further, I have used ABM techniques to posit a new and unique hypothesis for the role of pericytes in Notch1-DLL4 signaling during retinal vascular development. Put simply – the formation of blood vessel networks is much greater than the sum of each individual cell. The *connectivity* of endothelial cells and pericytes (and likely leukocytes and other mural cells) is truly paramount to establishing a healthy vasculature. As a result of my dissertation work, computational methods that study the emergent properties of developing vascular networks can better account for the multiscale connectivity between molecular mechanisms, cellular behaviors, and network-level geometric changes. These tools are now better poised to uncover new mechanistic hypotheses that could inform future experiments that may lead to medical advances in the treatment of proliferative vascular pathologies.

This process of self-assembly – a term used across multiple fields of research – continues to baffle, intrigue, and excite me. Endothelial cells have the capacity to generate complicated structures of vascular networks with the support of perivascular cells in a context-dependent manner. Bowman's capsule of the kidney, hepatic sinusoids, the retinal vasculature, and many other tissues – all of these specialized vascular networks are derived from the same component parts and are seemingly unrelated beyond the most basic comparison. To me, this typifies the beauty and mystery of biology. I hope that my efforts to elucidate – in a quantitative and mechanistic manner – a small part of this marvelous

machinery will contribute to a greater understanding of the fundamentals of tissue development at a cellular level.

# REFERENCES

MATLAB and Statistics Toolbox R2012b. Natick, Massachusetts, MathWorks Inc.

Adamson, R. (1993). "Microvascular endothelial cell shape and size in situ." Microvascular research **46**(1): 77-88.

Adra, S., T. Sun, S. MacNeil, M. Holcombe and R. Smallwood (2010). "Development of a three dimensional multiscale computational model of the human epidermis." PloS one **5**(1): e8511.

Aguado-Sierra, J., A. Krishnamurthy, C. Villongco, J. Chuang, E. Howard, M. J. Gonzales, J. Omens, D. E. Krummen, S. Narayan, R. C. Kerckhoffs and A. D. McCulloch (2011). "Patient-specific modeling of dyssynchronous heart failure: A case study." Progress in biophysics and molecular biology.

Alber, M., N. Chen, T. Glimm and P. M. Lushnikov (2006). "Multiscale dynamics of biological cells with chemotactic interactions: From a discrete stochastic model to a continuous description." Physical Review E **73**(5): 051901.

An, G. and S. Kulkarni (2015). "An agent-based modeling framework linking inflammation and cancer using evolutionary principles: Description of a generative hierarchy for the hallmarks of cancer and developing a bridge between mechanism and epidemiological data." Math Biosci **260C**: 16-24.

Armulik, A., G. Genové and C. Betsholtz (2011). "Pericytes: developmental, physiological, and pathological perspectives, problems, and promises." Developmental cell **21**(2): 193-215.

Armulik, A., G. Genove, M. Mae, M. H. Nisancioglu, E. Wallgard, C. Niaudet, L. He, J. Norlin, P. Lindblom, K. Strittmatter, B. R. Johansson and C. Betsholtz (2010). "Pericytes regulate the blood-brain barrier." Nature **468**(7323): 557-561.

Artel, A., H. Mehdizadeh, Y. C. Chiu, E. M. Brey and A. Cinar (2011). "An agent-based model for the investigation of neovascularization within porous scaffolds." Tissue engineering. Part A **17**(17-18): 2133-2141.

Bailey, A. M., B. C. Thorne and S. M. Peirce (2007). "Multi-cell agent-based simulation of the microvasculature to study the dynamics of circulating inflammatory cell trafficking." Annals of biomedical engineering **35**(6): 916-936.

Balazsi, G., A. van Oudenaarden and J. J. Collins (2011). "Cellular decision making and biological noise: from microbes to mammals." Cell **144**(6): 910-925.

Bandello, F., R. Lattanzio, I. Zucchiatti and C. Del Turco (2013). "Pathophysiology and treatment of diabetic retinopathy." Acta diabetologica.

Barkefors, I., S. Le Jan, L. Jakobsson, E. Hejll, G. Carlson, H. Johansson, J. Jarvius, J. W. Park, N. Li Jeon and J. Kreuger (2008). "Endothelial cell migration in stable gradients of vascular endothelial growth factor A

and fibroblast growth factor 2: effects on chemotaxis and chemokinesis." *J Biol Chem* **283**(20): 13905-13912.

Barua, D., J. Kim and J. L. Reed (2010). "An automated phenotype-driven approach (GeneForce) for refining metabolic and regulatory models." *PLoS computational biology* **6**(10): e1000970.

Bassingthwaight, J. B. (2010). "Predictive Modeling and Integrative Physiology: The Physiome Projects." *The open pacing, electrophysiology & therapy journal* **3**: 66-74.

Bassingthwaight, J. B. and H. J. Chizeck (2008). "The Physiome Projects and Multiscale Modeling." *IEEE signal processing magazine* **25**(2): 121-144.

Bauer, A. L., T. L. Jackson, Y. Jiang and T. Rohlf (2010). "Receptor cross-talk in angiogenesis: mapping environmental cues to cell phenotype using a stochastic, Boolean signaling network model." *Journal of theoretical biology* **264**(3): 838-846.

Ben-Jacob, E., M. Lu, D. Schultz and J. N. Onuchic (2014). "The physics of bacterial decision making." *Front Cell Infect Microbiol* **4**: 154.

Benedito, R., C. Roca, I. Sorensen, S. Adams, A. Gossler, M. Fruttiger and R. H. Adams (2009). "The notch ligands Dll4 and Jagged1 have opposing effects on angiogenesis." *Cell* **137**(6): 1124-1135.

Bentley, K., C. A. Franco, A. Philippides, R. Blanco, M. Dierkes, V. Gebala, F. Stanchi, M. Jones, I. M. Aspalter, G. Cagna, S. Westrom, L. Claesson-Welsh, D. Vestweber and H. Gerhardt (2014). "The role of differential VE-cadherin dynamics in cell rearrangement during angiogenesis." *Nat Cell Biol* **16**(4): 309-321.

Bentley, K., H. Gerhardt and P. A. Bates (2008). "Agent-based simulation of notch-mediated tip cell selection in angiogenic sprout initialisation." *Journal of theoretical biology* **250**(1): 25-36.

Bentley, K., G. Mariggi, H. Gerhardt and P. A. Bates (2009). "Tipping the balance: robustness of tip cell selection, migration and fusion in angiogenesis." *PLoS Comput Biol* **5**(10): e1000549.

Bentley, K., A. Philippides and E. Ravasz Regan (2014). "Do endothelial cells dream of eclectic shape?" *Dev Cell* **29**(2): 146-158.

Bjarnegard, M., M. Enge, J. Norlin, S. Gustafsdottir, S. Fredriksson, A. Abramsson, M. Takemoto, E. Gustafsson, R. Fassler and C. Betsholtz (2004). "Endothelium-specific ablation of PDGFB leads to pericyte loss and glomerular, cardiac and placental abnormalities." *Development* **131**(8): 1847-1857.

Blake, W. J. and J. J. Collins (2005). "And the noise played on: stochastic gene expression and HIV-1 infection." *Cell* **122**(2): 147-149.

Borlin, C. S., V. Lang, A. Hamacher-Brady and N. R. Brady (2014). "Agent-based modeling of autophagy reveals emergent regulatory behavior of spatio-temporal autophagy dynamics." *Cell Commun Signal* **12**(1): 56.

Bressler, S., H. Qin, M. Melia, N. Bressler, R. Beck, C. Chan, S. Grover, D. Miller and N. Diabetic Retinopathy Clinical Research (2013). "Exploratory analysis of the effect of intravitreal ranibizumab or

triamcinolone on worsening of diabetic retinopathy in a randomized clinical trial." JAMA ophthalmology **131**(8): 1033-1040.

Brodland, G. W., X. Chen, P. Lee and M. Marsden (2010). "From genes to neural tube defects (NTDs): insights from multiscale computational modeling." HFSP journal **4**(3-4): 142-152.

Brown, B. N., I. M. Price, F. R. Toapanta, D. R. DeAlmeida, C. A. Wiley, T. M. Ross, T. D. Oury and Y. Vodovotz (2011). "An agent-based model of inflammation and fibrosis following particulate exposure in the lung." Mathematical biosciences **231**(2): 186-196.

Brown, E. B., R. B. Campbell, Y. Tsuzuki, L. Xu, P. Carmeliet, D. Fukumura and R. K. Jain (2001). "In vivo measurement of gene expression, angiogenesis and physiological function in tumors using multiphoton laser scanning microscopy." Nat Med **7**(7): 864-868.

Callura, J. M., C. R. Cantor and J. J. Collins (2012). "Genetic switchboard for synthetic biology applications." Proceedings of the National Academy of Sciences of the United States of America **109**(15): 5850-5855.

Cao, R., Y. Xue, E. M. Hedlund, Z. Zhong, K. Tritsarlis, B. Tondelli, F. Lucchini, Z. Zhu, S. Dissing and Y. Cao (2010). "VEGFR1-mediated pericyte ablation links VEGF and PlGF to cancer-associated retinopathy." Proc Natl Acad Sci U S A **107**(2): 856-861.

Caputo, K. E. and D. A. Hammer (2009). "Adhesive dynamics simulation of G-protein-mediated chemokine-activated neutrophil adhesion." Biophysical journal **96**(8): 2989-3004.

Carrier, A., L. Geris, K. Bentley, G. Carmeliet, P. Carmeliet and H. Van Oosterwyck (2012). "MOSAIC: a multiscale model of osteogenesis and sprouting angiogenesis with lateral inhibition of endothelial cells." PLoS computational biology **8**(10).

Causey, L., S. C. Cowin and S. Weinbaum (2012). "Quantitative model for predicting lymph formation and muscle compressibility in skeletal muscle during contraction and stretch." Proceedings of the National Academy of Sciences of the United States of America **109**(23): 9185-9190.

Chang, W. G., J. W. Andrejcsk, M. S. Kluger, W. M. Saltzman and J. S. Pober (2013). "Pericytes modulate endothelial sprouting." Cardiovasc Res **100**(3): 492-500.

Chappell, J. C., S. M. Taylor, N. Ferrara and V. L. Bautch (2009). "Local guidance of emerging vessel sprouts requires soluble Flt-1." Developmental cell **17**(3): 377-386.

Chappell, J. C., D. M. Wiley and V. L. Bautch (2011). "Regulation of blood vessel sprouting." Seminars in cell & developmental biology **22**(9): 1005-1011.

Cilfone, N. A., C. B. Ford, S. Marino, J. T. Mattila, H. P. Gideon, J. L. Flynn, D. E. Kirschner and J. J. Linderman (2015). "Computational Modeling Predicts IL-10 Control of Lesion Sterilization by Balancing Early Host Immunity-Mediated Antimicrobial Responses with Caseation during Mycobacterium tuberculosis Infection." J Immunol **194**(2): 664-677.

Clayton, A. and A. J. Bishop (2011). "Dissection of a mouse eye for a whole mount of the retinal pigment epithelium." J Vis Exp(48).

Coddington, E. A. and N. Levinson (1955). Theory of ordinary differential equations. New York,, McGraw-Hill.

Cosgrove, B. D., L. G. Alexopoulos, J. Saez-Rodriguez, L. G. Griffith and D. A. Lauffenburger (2009). "A multipathway phosphoproteomic signaling network model of idiosyncratic drug- and inflammatory cytokine-induced toxicity in human hepatocytes." Conference proceedings : ... Annual International Conference of the IEEE Engineering in Medicine and Biology Society. IEEE Engineering in Medicine and Biology Society. Conference **2009**: 5452-5455.

Cotter, S. L., V. Klika, L. Kimpton, S. Collins and A. E. Heazell (2014). "A stochastic model for early placental development." J R Soc Interface **11**(97): 20140149.

Das, A., D. Lauffenburger, H. Asada and R. D. Kamm (2010). "A hybrid continuum-discrete modelling approach to predict and control angiogenesis: analysis of combinatorial growth factor and matrix effects on vessel-sprouting morphology." Philosophical transactions. Series A, Mathematical, physical, and engineering sciences **368**(1921): 2937-2960.

Derycke, L., L. Morbidelli, M. Ziche, O. De Wever, M. Bracke and E. Van Aken (2006). "Soluble N-cadherin fragment promotes angiogenesis." Clinical & experimental metastasis **23**(3-4): 187-201.

Díaz-Flores, L., R. Gutiérrez, H. Varela, N. Rancel and F. Valladares (1991). "Microvascular pericytes: a review of their morphological and functional characteristics." Histology and histopathology **6**(2): 269-286.

Dorrell, M., E. Aguilar and M. Friedlander (2002). "Retinal vascular development is mediated by endothelial filopodia, a preexisting astrocytic template and specific R-cadherin adhesion." Investigative ophthalmology & visual ....

Du, P., G. O'Grady, J. B. Davidson, L. K. Cheng and A. J. Pullan (2010). "Multiscale modeling of gastrointestinal electrophysiology and experimental validation." Critical reviews in biomedical engineering **38**(3): 225-254.

Dulmovits, B. and I. Herman (2012). "Microvascular remodeling and wound healing: a role for pericytes." The international journal of biochemistry & cell biology **44**(11): 1800-1812.

Durham, J. T., H. K. Surks, B. M. Dulmovits and I. M. Herman (2014). "Pericyte contractility controls endothelial cell cycle progression and sprouting: insights into angiogenic switch mechanics." Am J Physiol Cell Physiol **307**(9): C878-892.

Eilken, H. M. and R. H. Adams (2010). "Dynamics of endothelial cell behavior in sprouting angiogenesis." Current opinion in cell biology **22**(5): 617-625.

Eissing, T., L. Kuepfer, C. Becker, M. Block, K. Coboeken, T. Gaub, L. Goerlitz, J. Jaeger, R. Loosen, B. Ludewig, M. Meyer, C. Niederal, M. Sevestre, H. U. Siegmund, J. Solodenko, K. Thelen, U. Telle, W. Weiss, T. Wendl, S. Willmann and J. Lippert (2011). "A computational systems biology software platform for multiscale modeling and simulation: integrating whole-body physiology, disease biology, and molecular reaction networks." Frontiers in physiology **2**: 4.

Ejaz, S., I. Chekarova, A. Ejaz, A. Sohail and C. Lim (2008). "Importance of pericytes and mechanisms of pericyte loss during diabetes retinopathy." Diabetes, obesity & metabolism **10**(1): 53-63.

Fainaru, O., A. Adini, O. Benny, I. Adini, S. Short, L. Bazinet, K. Nakai, E. Pravda, M. D. Hornstein, R. J. D'Amato and J. Folkman (2008). "Dendritic cells support angiogenesis and promote lesion growth in a murine model of endometriosis." FASEB journal : official publication of the Federation of American Societies for Experimental Biology **22**(2): 522-529.

Fallahi-Sichani, M., J. L. Flynn, J. J. Linderman and D. E. Kirschner (2012). "Differential risk of tuberculosis reactivation among anti-TNF therapies is due to drug binding kinetics and permeability." Journal of immunology **188**(7): 3169-3178.

Fallahi-Sichani, M., D. E. Kirschner and J. J. Linderman (2012). "NF-kappaB Signaling Dynamics Play a Key Role in Infection Control in Tuberculosis." Frontiers in physiology **3**: 170.

Fedosov, D. A., H. Lei, B. Caswell, S. Suresh and G. E. Karniadakis (2011). "Multiscale modeling of red blood cell mechanics and blood flow in malaria." PLoS computational biology **7**(12): e1002270.

Ferrara, N. (2005). "The role of VEGF in the regulation of physiological and pathological angiogenesis." EXS(94): 209-231.

Ferrara, N., H. P. Gerber and J. LeCouter (2003). "The biology of VEGF and its receptors." Nat Med **9**(6): 669-676.

Folcik, V. A., G. Broderick, S. Mohan, B. Block, C. Ekbote, J. Doolittle, M. Khoury, L. Davis and C. B. Marsh (2011). "Using an agent-based model to analyze the dynamic communication network of the immune response." Theoretical biology & medical modelling **8**: 1.

Folkman, J. (1971). "Tumor angiogenesis: therapeutic implications." The New England journal of medicine **285**(21): 1182-1186.

Fong, G., J. Rossant, M. Gertsenstein and M. Breitman (1995). "Role of the Flt-1 receptor tyrosine kinase in regulating the assembly of vascular endothelium." Nature **376**(6535): 66-70.

Frank, R. N. (2004). "Diabetic retinopathy." The New England journal of medicine **350**(1): 48-58.

Frank, R. N., S. Dutta and M. A. Mancini (1987). "Pericyte coverage is greater in the retinal than in the cerebral capillaries of the rat." Invest Ophthalmol Vis Sci **28**(7): 1086-1091.

Frank, R. N., T. J. Turczyn and A. Das (1990). "Pericyte coverage of retinal and cerebral capillaries." Invest Ophthalmol Vis Sci **31**(6): 999-1007.

Friedl, P. and K. Wolf (2010). "Plasticity of cell migration: a multiscale tuning model." The Journal of cell biology **188**(1): 11-19.

Fruttiger, M. (2007). "Development of the retinal vasculature." Angiogenesis **10**(2): 77-88.

- Fukumura, D., D. G. Duda, L. L. Munn and R. K. Jain (2010). "Tumor microvasculature and microenvironment: novel insights through intravital imaging in pre-clinical models." Microcirculation **17**(3): 206-225.
- Geraldes, P., J. Hiraoka-Yamamoto, M. Matsumoto, A. Clermont, M. Leitges, A. Marette, L. P. Aiello, T. S. Kern and G. L. King (2009). "Activation of PKC-delta and SHP-1 by hyperglycemia causes vascular cell apoptosis and diabetic retinopathy." Nature medicine **15**(11): 1298-1306.
- Gerhardt, H. and C. Betsholtz (2003). "Endothelial-pericyte interactions in angiogenesis." Cell Tissue Res **314**(1): 15-23.
- Giannouli, C. C., P. Chandris and R. L. Proia (2014). "Visualizing S1P-directed cellular egress by intravital imaging." Biochim Biophys Acta **1841**(5): 738-744.
- Gillespie, D. T. (1977). "Exact Stochastic Simulation of Coupled Chemical-Reactions." Journal of Physical Chemistry **81**(25): 2340-2361.
- Goktepe, S., O. J. Abilez, K. K. Parker and E. Kuhl (2010). "A multiscale model for eccentric and concentric cardiac growth through sarcomerogenesis." Journal of theoretical biology **265**(3): 433-442.
- Gopalakrishnan, V., M. Kim and G. An (2013). "Using an Agent-Based Model to Examine the Role of Dynamic Bacterial Virulence Potential in the Pathogenesis of Surgical Site Infection." Adv Wound Care (New Rochelle) **2**(9): 510-526.
- Greenstein, J. L. and R. L. Winslow (2011). "Integrative systems models of cardiac excitation-contraction coupling." Circulation research **108**(1): 70-84.
- Grima, R. (2008). "Multiscale modeling of biological pattern formation." Current topics in developmental biology **81**: 435-460.
- Haggart, C. R., J. A. Bartell, J. J. Saucerman and J. A. Papin (2011). "Whole-genome metabolic network reconstruction and constraint-based modeling." Methods in enzymology **500**: 411-433.
- Hainaud, P., J. O. Contreres, A. Villemain, L. X. Liu, J. Plouet, G. Tobelem and E. Dupuy (2006). "The role of the vascular endothelial growth factor-Delta-like 4 ligand/Notch4-ephrin B2 cascade in tumor vessel remodeling and endothelial cell functions." Cancer Res **66**(17): 8501-8510.
- Hammes, H.-P., Y. Feng, F. Pfister and M. Brownlee (2011). "Diabetic retinopathy: targeting vasoregression." Diabetes **60**(1): 9-16.
- Hartnett, M. E. (2015). "Pathophysiology and mechanisms of severe retinopathy of prematurity." Ophthalmology **122**(1): 200-210.
- Hashambhoy, Y. L., J. C. Chappell, S. M. Peirce, V. L. Bautch and F. Mac Gabhann (2011). "Computational modeling of interacting VEGF and soluble VEGF receptor concentration gradients." Frontiers in physiology **2**: 62.

Hayenga, H. N., B. C. Thorne, S. M. Peirce and J. D. Humphrey (2011). "Ensuring Congruency in Multiscale Modeling: Towards Linking Agent Based and Continuum Biomechanical Models of Arterial Adaptation." Annals of biomedical engineering.

Hellstrom, M., L. K. Phng, J. J. Hofmann, E. Wallgard, L. Coultas, P. Lindblom, J. Alva, A. K. Nilsson, L. Karlsson, N. Gaiano, K. Yoon, J. Rossant, M. L. Iruela-Arispe, M. Kalen, H. Gerhardt and C. Betsholtz (2007). "Dll4 signalling through Notch1 regulates formation of tip cells during angiogenesis." Nature **445**(7129): 776-780.

Hofmann, J. J. and M. Luisa Iruela-Arispe (2007). "Notch expression patterns in the retina: An eye on receptor-ligand distribution during angiogenesis." Gene Expr Patterns **7**(4): 461-470.

Holland, D. O., N. C. Krainak and J. J. Saucerman (2011). "Graphical approach to model reduction for nonlinear biochemical networks." PloS one **6**(8): e23795.

Hughes, C. (2008). "Endothelial-stromal interactions in angiogenesis." Current opinion in hematology **15**(3): 204-209.

Jain, R. K., L. L. Munn and D. Fukumura (2013). "Measuring leukocyte-endothelial interactions in mice." Cold Spring Harb Protoc **2013**(6): 561-563.

Jakobsson, L., C. Franco, K. Bentley, R. Collins, B. Ponsioen, I. Aspalter, I. Rosewell, M. Busse, G. Thurston, A. Medvinsky, S. Schulte-Merker and H. Gerhardt (2010). "Endothelial cells dynamically compete for the tip cell position during angiogenic sprouting." Nature cell biology **12**(10): 943-953.

Kaern, M., T. C. Elston, W. J. Blake and J. J. Collins (2005). "Stochasticity in gene expression: from theories to phenotypes." Nat Rev Genet **6**(6): 451-464.

Kearney, J. B. and V. L. Bautch (2003). "In vitro differentiation of mouse ES cells: hematopoietic and vascular development." Methods in enzymology **365**: 83-98.

Kearney, J. B. and V. L. Bautch (2003). "In vitro differentiation of mouse ES cells: hematopoietic and vascular development." Methods Enzymol **365**: 83-98.

Kearney, J. B., N. C. Kappas, C. Ellerstrom, F. W. DiPaola and V. L. Bautch (2004). "The VEGF receptor flt-1 (VEGFR-1) is a positive modulator of vascular sprout formation and branching morphogenesis." Blood **103**(12): 4527-4535.

Kelly-Goss, M., R. Sweat, P. Stapor, S. Peirce and W. Murfee (2013). "Targeting Pericytes for Angiogenic Therapies." Microcirculation (New York, N.Y. : 1994).

Kim, M. J. and I. V. Maly (2009). "Deterministic mechanical model of T-killer cell polarization reproduces the wandering of aim between simultaneously engaged targets." PLoS computational biology **5**(1): e1000260.

Kirschner, D. E. and J. J. Linderman (2009). "Mathematical and computational approaches can complement experimental studies of host-pathogen interactions." Cell Microbiol **11**(4): 531-539.

- Kleinstreuer, N., D. Dix, M. Rountree, N. Baker, N. Sipes, D. Reif, R. Spencer and T. Knudsen (2013). "A computational model predicting disruption of blood vessel development." PLoS computational biology **9**(4).
- Kulkarni, P., T. Shiraishi and R. V. Kulkarni (2013). "Cancer: tilting at windmills?" Mol Cancer **12**(1): 108.
- Laise, P., F. Di Patti, D. Fanelli, M. Masselli and A. Arcangeli (2011). "Deterministic and stochastic aspects of VEGF-A production and the cooperative behavior of tumoral cell colony." Journal of theoretical biology **272**(1): 55-63.
- Lee, S., A. Zeiger, J. Maloney, M. Kotecki, K. Van Vliet and I. Herman (2010). "Pericyte actomyosin-mediated contraction at the cell-material interface can modulate the microvascular niche." Journal of physics. Condensed matter : an Institute of Physics journal **22**(19): 194115.
- Leslie, J. D., L. Ariza-McNaughton, A. L. Bermange, R. McAdow, S. L. Johnson and J. Lewis (2007). "Endothelial signalling by the Notch ligand Delta-like 4 restricts angiogenesis." Development **134**(5): 839-844.
- Liu, G., A. A. Qutub, P. Vempati, F. Mac Gabhann and A. S. Popel (2011). "Module-based multiscale simulation of angiogenesis in skeletal muscle." Theoretical biology & medical modelling **8**: 6.
- Liu, L., B. D. Ratner, E. H. Sage and S. Jiang (2007). "Endothelial cell migration on surface-density gradients of fibronectin, VEGF, or both proteins." Langmuir **23**(22): 11168-11173.
- Long, B. L., R. Rekhi, A. Abrego, J. Jung and A. A. Qutub (2013). "Cells as state machines: cell behavior patterns arise during capillary formation as a function of BDNF and VEGF." J Theor Biol **326**: 43-57.
- Longo, D., S. M. Peirce, T. C. Skalak, L. Davidson, M. Marsden, B. Dzamba and D. W. DeSimone (2004). "Multicellular computer simulation of morphogenesis: blastocoel roof thinning and matrix assembly in *Xenopus laevis*." Developmental biology **271**(1): 210-222.
- Louvi, A. and S. Artavanis-Tsakonas (2012). "Notch and disease: a growing field." Seminars in cell & developmental biology **23**(4): 473-480.
- Mac Gabhann, F., B. Annex and A. Popel (2010). "Gene therapy from the perspective of systems biology." Current opinion in molecular therapeutics **12**(5): 570-577.
- Mac Gabhann, F. and A. Popel (2004). "Model of competitive binding of vascular endothelial growth factor and placental growth factor to VEGF receptors on endothelial cells." American journal of physiology. Heart and circulatory physiology **286**(1): 64.
- Mac Gabhann, F., M. T. Yang and A. S. Popel (2005). "Monte Carlo simulations of VEGF binding to cell surface receptors in vitro." Biochim Biophys Acta **1746**(2): 95-107.
- Machado, D. E., P. T. Berardo, C. Y. Palmero and L. E. Nasciutti (2010). "Higher expression of vascular endothelial growth factor (VEGF) and its receptor VEGFR-2 (Flk-1) and metalloproteinase-9 (MMP-9) in a rat model of peritoneal endometriosis is similar to cancer diseases." Journal of experimental & clinical cancer research : CR **29**: 4.

Magnusson, P. U., C. Looman, A. Ahgren, Y. Wu, L. Claesson-Welsh and R. L. Heuchel (2007). "Platelet-derived growth factor receptor-beta constitutive activity promotes angiogenesis in vivo and in vitro." Arterioscler Thromb Vasc Biol **27**(10): 2142-2149.

Meir, E., E. M. Munro, G. M. Odell and G. Von Dassow (2002). "Ingeneue: a versatile tool for reconstituting genetic networks, with examples from the segment polarity network." The Journal of experimental zoology **294**(3): 216-251.

Mendel, T., E. Clabough, D. Kao, T. Demidova-Rice, J. Durham, B. Zotter, S. Seaman, S. Cronk, E. Rakoczy, A. Katz, I. Herman, S. Peirce and P. Yates (2013). "Pericytes derived from adipose-derived stem cells protect against retinal vasculopathy." PloS one **8**(5).

Merks, R. M., E. D. Perryn, A. Shirinifard and J. A. Glazier (2008). "Contact-inhibited chemotaxis in de novo and sprouting blood-vessel growth." PLoS computational biology **4**(9): e1000163.

Milde, F., S. Lauw, P. Koumoutsakos and M. L. Iruela-Arispe (2013). "The mouse retina in 3D: quantification of vascular growth and remodeling." Integr Biol (Camb) **5**(12): 1426-1438.

Milne, C. B., J. A. Eddy, R. Raju, S. Ardekani, P. J. Kim, R. S. Senger, Y. S. Jin, H. P. Blaschek and N. D. Price (2011). "Metabolic network reconstruction and genome-scale model of butanol-producing strain *Clostridium beijerinckii* NCIMB 8052." BMC systems biology **5**: 130.

Modi, S. R., D. M. Camacho, M. A. Kohanski, G. C. Walker and J. J. Collins (2011). "Functional characterization of bacterial sRNAs using a network biology approach." Proceedings of the National Academy of Sciences of the United States of America **108**(37): 15522-15527.

Moreno, J. D., Z. I. Zhu, P. C. Yang, J. R. Bankston, M. T. Jeng, C. Kang, L. Wang, J. D. Bayer, D. J. Christini, N. A. Trayanova, C. M. Ripplinger, R. S. Kass and C. E. Clancy (2011). "A computational model to predict the effects of class I anti-arrhythmic drugs on ventricular rhythms." Science translational medicine **3**(98): 98ra83.

Motiejunaite, R. and A. Kazlauskas (2008). "Pericytes and ocular diseases." Exp Eye Res **86**(2): 171-177.

N'Dri, N. A., W. Shyy and R. Tran-Son-Tay (2003). "Computational modeling of cell adhesion and movement using a continuum-kinetics approach." Biophysical journal **85**(4): 2273-2286.

Nagarajan, M. B., M. B. Huber, T. Schlossbauer, G. Leinsinger, A. Krol and A. Wismuller (2013). "Classification of small lesions in dynamic breast MRI: Eliminating the need for precise lesion segmentation through spatio-temporal analysis of contrast enhancement over time." Mach Vis Appl **24**(7).

Nawroth, J. C., H. Lee, A. W. Feinberg, C. M. Ripplinger, M. L. McCain, A. Grosberg, J. O. Dabiri and K. K. Parker (2012). "A tissue-engineered jellyfish with biomimetic propulsion." Nature biotechnology.

Newman, S. A., S. Christley, T. Glimm, H. G. Hentschel, B. Kazmierczak, Y. T. Zhang, J. Zhu and M. Alber (2008). "Multiscale models for vertebrate limb development." Current topics in developmental biology **81**: 311-340.

- Noguera-Troise, I., C. Daly, N. J. Papadopoulos, S. Coetzee, P. Boland, N. W. Gale, H. C. Lin, G. D. Yancopoulos and G. Thurston (2006). "Blockade of Dll4 inhibits tumour growth by promoting non-productive angiogenesis." Nature **444**(7122): 1032-1037.
- Padera, T. P., B. R. Stoll, P. T. So and R. K. Jain (2002). "Conventional and high-speed intravital multiphoton laser scanning microscopy of microvasculature, lymphatics, and leukocyte-endothelial interactions." Mol Imaging **1**(1): 9-15.
- Paik, J.-H., A. Skoura, S.-S. Chae, A. Cowan, D. Han, R. Proia and T. Hla (2004). "Sphingosine 1-phosphate receptor regulation of N-cadherin mediates vascular stabilization." Genes & development **18**(19): 2392-2403.
- Pedrosa, A. R., A. Trindade, A. C. Fernandes, C. Carvalho, J. Gigante, A. T. Tavares, R. Dieguez-Hurtado, H. Yagita, R. H. Adams and A. Duarte (2015). "Endothelial Jagged1 Antagonizes Dll4 Regulation of Endothelial Branching and Promotes Vascular Maturation Downstream of Dll4/Notch1." Arterioscler Thromb Vasc Biol.
- Peirce-Cottler, S. M., F. Mac Gabhann and V. L. Bautch (2012). "Integration of Experimental and Computational Approaches to Sprouting Angiogenesis."
- Plank, M. J., B. D. Sleeman and P. F. Jones (2004). "A mathematical model of tumour angiogenesis, regulated by vascular endothelial growth factor and the angiopoietins." Journal of theoretical biology **229**(4): 435-454.
- Pospieszalska, M. K., A. Zarbock, J. E. Pickard and K. Ley (2009). "Event-tracking model of adhesion identifies load-bearing bonds in rolling leukocytes." Microcirculation **16**(2): 115-130.
- Potente, M., H. Gerhardt and P. Carmeliet (2011). "Basic and therapeutic aspects of angiogenesis." Cell **146**(6): 873-887.
- Qu, Z., A. Garfinkel, J. N. Weiss and M. Nivala (2011). "Multi-scale modeling in biology: How to bridge the gaps between scales?" Progress in biophysics and molecular biology.
- Quo, C. F., R. A. Moffitt, A. H. Merrill and M. D. Wang (2011). "Adaptive control model reveals systematic feedback and key molecules in metabolic pathway regulation." Journal of computational biology : a journal of computational molecular cell biology **18**(2): 169-182.
- Ribatti, D., B. Nico and E. Crivellato (2011). "The role of pericytes in angiogenesis." The International journal of developmental biology **55**(3): 261-268.
- Ricard, N., D. Ciais, S. Levet, M. Subileau, C. Mallet, T. A. Zimmers, S. J. Lee, M. Bidart, J. J. Feige and S. Bailly (2012). "BMP9 and BMP10 are critical for postnatal retinal vascular remodeling." Blood **119**(25): 6162-6171.
- Sample, C. and S. Y. Shvartsman (2010). "Multiscale modeling of diffusion in the early Drosophila embryo." Proceedings of the National Academy of Sciences of the United States of America **107**(22): 10092-10096.

- Sander, E. A., T. Stylianopoulos, R. T. Tranquillo and V. H. Barocas (2009). "Image-based multiscale modeling predicts tissue-level and network-level fiber reorganization in stretched cell-compacted collagen gels." Proceedings of the National Academy of Sciences of the United States of America **106**(42): 17675-17680.
- Scheef, E., C. Sorenson and N. Sheibani (2009). "Attenuation of proliferation and migration of retinal pericytes in the absence of thrombospondin-1." American journal of physiology. Cell physiology **296**(4): 34.
- Scheff, J. D., P. D. Mavroudis, S. E. Calvano, S. F. Lowry and I. P. Androulakis (2011). "Modeling autonomic regulation of cardiac function and heart rate variability in human endotoxemia." Physiological genomics **43**(16): 951-964.
- Schmidt, B. J., J. A. Papin and M. B. Lawrence (2009). "Nano-motion dynamics are determined by surface-tethered selectin mechanokinetics and bond formation." PLoS computational biology **5**(12): e1000612.
- Scott, A., M. B. Powner, P. Gandhi, C. Clarkin, D. H. Gutmann, R. S. Johnson, N. Ferrara and M. Fruttiger (2010). "Astrocyte-derived vascular endothelial growth factor stabilizes vessels in the developing retinal vasculature." PLoS One **5**(7): e11863.
- Seaman, M. E., S. M. Peirce and K. Kelly (2011). "Rapid analysis of vessel elements (RAVE): a tool for studying physiologic, pathologic and tumor angiogenesis." PLoS One **6**(6): e20807.
- Seok, J., W. Xiao, L. L. Moldawer, R. W. Davis and M. W. Covert (2009). "A dynamic network of transcription in LPS-treated human subjects." BMC systems biology **3**: 78.
- Sharafi, B., E. G. Ames, J. W. Holmes and S. S. Blemker (2011). "Strains at the myotendinous junction predicted by a micromechanical model." Journal of biomechanics.
- Shirinifard, A., J. S. Gens, B. L. Zaitlen, N. J. Poplawski, M. Swat and J. A. Glazier (2009). "3D multi-cell simulation of tumor growth and angiogenesis." PLoS one **4**(10): e7190.
- Silva, E. A., C. Eseonu and D. J. Mooney (2014). "Endothelial cells expressing low levels of CD143 (ACE) exhibit enhanced sprouting and potency in relieving tissue ischemia." Angiogenesis.
- Silva, J. R. and Y. Rudy (2010). "Multi-scale electrophysiology modeling: from atom to organ." The Journal of general physiology **135**(6): 575-581.
- Simonavicius, N., M. Ashenden, A. van Weverwijk, S. Lax, D. Huso, C. Buckley, I. Huijbers, I. Huijber, H. Yarwood and C. Isacke (2012). "Pericytes promote selective vessel regression to regulate vascular patterning." Blood **120**(7): 1516-1527.
- Sims, D. (1986). "The pericyte--a review." Tissue & cell **18**(2): 153-174.
- Singh, S., A. S. Narang and R. I. Mahato (2011). "Subcellular fate and off-target effects of siRNA, shRNA, and miRNA." Pharmaceutical research **28**(12): 2996-3015.

Sprinzak, D., A. Lakhanpal, L. Lebon, L. A. Santat, M. E. Fontes, G. A. Anderson, J. Garcia-Ojalvo and M. B. Elowitz (2010). "Cis-interactions between Notch and Delta generate mutually exclusive signalling states." Nature **465**(7294): 86-90.

Stapor, P., M. Azimi, T. Ahsan and W. Murfee (2012). "An Angiogenesis Model for Investigating Multi-Cellular Interactions across Intact Microvascular Networks." American journal of physiology. Heart and circulatory physiology.

Stark, K., A. Eckart, S. Haidari, A. Tirniceriu, M. Lorenz, M.-L. von Brühl, F. G. S. rtner, A. Khandoga, K. Legate, R. Pless, I. Hepper, K. Lauber, B. Walzog and S. Massberg (2013). "Capillary and arteriolar pericytes attract innate leukocytes exiting through venules and 'instruct' them with pattern-recognition and motility programs." Nature immunology **14**(1): 41-51.

Staton, C. A., M. W. Reed and N. J. Brown (2009). "A critical analysis of current in vitro and in vivo angiogenesis assays." International journal of experimental pathology **90**(3): 195-221.

Stefanini, M. O., F. T. Wu, F. Mac Gabhann and A. S. Popel (2008). "A compartment model of VEGF distribution in blood, healthy and diseased tissues." BMC Syst Biol **2**: 77.

Stewart, D. J., M. J. Kutryk, D. Fitchett, M. Freeman, N. Camack, Y. Su, A. Della Siega, L. Bilodeau, J. R. Burton, G. Proulx and S. Radhakrishnan (2009). "VEGF gene therapy fails to improve perfusion of ischemic myocardium in patients with advanced coronary disease: results of the NORTHERN trial." Molecular therapy : the journal of the American Society of Gene Therapy **17**(6): 1109-1115.

Strieter, R. M., M. D. Burdick, J. Mestas, B. Gomperts, M. P. Keane and J. A. Belperio (2006). "Cancer CXC chemokine networks and tumour angiogenesis." Eur J Cancer **42**(6): 768-778.

Sun, T., S. Adra, R. Smallwood, M. Holcombe and S. MacNeil (2009). "Exploring hypotheses of the actions of TGF-beta1 in epidermal wound healing using a 3D computational multiscale model of the human epidermis." PloS one **4**(12): e8515.

Swanson, K. R., R. C. Rockne, J. Claridge, M. A. Chaplain, E. C. Alvord, Jr. and A. R. Anderson (2011). "Quantifying the role of angiogenesis in malignant progression of gliomas: in silico modeling integrates imaging and histology." Cancer research **71**(24): 7366-7375.

Tanaka, K., Y. Toiyama, Y. Okugawa, M. Okigami, Y. Inoue, K. Uchida, T. Araki, Y. Mohri, A. Mizoguchi and M. Kusunoki (2014). "In vivo optical imaging of cancer metastasis using multiphoton microscopy: a short review." Am J Transl Res **6**(3): 179-187.

Tawhai, M. H., K. S. Burrowes and E. A. Hoffman (2006). "Computational models of structure-function relationships in the pulmonary circulation and their validation." Exp Physiol **91**(2): 285-293.

Taylor, A. C., L. M. Seltz, P. A. Yates and S. M. Peirce "Chronic whole-body hypoxia induces intussusceptive angiogenesis and microvascular remodeling in the mouse retina." Microvasc Res **79**(2): 93-101.

Thompson, A. B., F. S. Gayzik, D. P. Moreno, A. C. Rhyne, N. A. Vavalle and J. D. Stitzel (2012). "A paradigm for human body finite element model integration from a set of regional models." Biomedical sciences instrumentation **48**: 423-430.

- Thorne, B. C., H. N. Hayenga, J. D. Humphrey and S. M. Peirce (2011). "Toward a multi-scale computational model of arterial adaptation in hypertension: verification of a multi-cell agent based model." Frontiers in physiology **2**: 20.
- Tillet, E., D. Vittet, O. Féraud, R. Moore, R. Kemler and P. Huber (2005). "N-cadherin deficiency impairs pericyte recruitment, and not endothelial differentiation or sprouting, in embryonic stem cell-derived angiogenesis." Experimental cell research **310**(2): 392-400.
- Tomlin, C. J. and J. D. Axelrod (2007). "Biology by numbers: mathematical modelling in developmental biology." Nature reviews. Genetics **8**(5): 331-340.
- Trayanova, N. A. and J. J. Rice (2011). "Cardiac electromechanical models: from cell to organ." Frontiers in physiology **2**: 43.
- Tveito, A., G. T. Lines, A. G. Edwards, M. M. Maleckar, A. Michailova, J. Hake and A. McCulloch (2012). "Slow Calcium-Depolarization-Calcium waves may initiate fast local depolarization waves in ventricular tissue." Progress in biophysics and molecular biology.
- Valentin, A. and J. D. Humphrey (2009). "Evaluation of fundamental hypotheses underlying constrained mixture models of arterial growth and remodelling." Philosophical transactions. Series A, Mathematical, physical, and engineering sciences **367**(1902): 3585-3606.
- Valentin, A. and J. D. Humphrey (2009). "Parameter sensitivity study of a constrained mixture model of arterial growth and remodeling." Journal of biomechanical engineering **131**(10): 101006.
- van der Meer, A. D., K. Vermeul, A. A. Poot, J. Feijen and I. Vermes (2010). "A microfluidic wound-healing assay for quantifying endothelial cell migration." Am J Physiol Heart Circ Physiol **298**(2): H719-725.
- Vempati, P., A. S. Popel and F. Mac Gabhann (2011). "Formation of VEGF isoform-specific spatial distributions governing angiogenesis: computational analysis." BMC systems biology **5**: 59.
- von Dassow, G., E. Meir, E. M. Munro and G. M. Odell (2000). "The segment polarity network is a robust developmental module." Nature **406**(6792): 188-192.
- Walpole, J., J. A. Papin and S. M. Peirce (2013). "Multiscale computational models of complex biological systems." Annu Rev Biomed Eng **15**: 137-154.
- Weber, M. and J. Buceta (2013). "Dynamics of the quorum sensing switch: stochastic and non-stationary effects." BMC Syst Biol **7**: 6.
- West, H., W. D. Richardson and M. Fruttiger (2005). "Stabilization of the retinal vascular network by reciprocal feedback between blood vessels and astrocytes." Development **132**(8): 1855-1862.
- Wilensky, U. (1999). Netlogo. <http://ccl.northwestern.edu/netlogo>. Center for Connected Learning and Computer-Based Modeling, Northwestern University. Evanston, IL.
- Wiley, D. M., J. D. Kim, J. Hao, C. C. Hong, V. L. Bautch and S. W. Jin (2011). "Distinct signalling pathways regulate sprouting angiogenesis from the dorsal aorta and the axial vein." Nature cell biology **13**(6): 686-692.

Wisniewska-Kruk, J., K. A. Hoeben, I. M. Vogels, P. J. Gaillard, C. J. Van Noorden, R. O. Schlingemann and I. Klaassen (2012). "A novel co-culture model of the blood-retinal barrier based on primary retinal endothelial cells, pericytes and astrocytes." Exp Eye Res **96**(1): 181-190.

Wu, L., P. Fernandez-Loaiza, J. Sauma, E. Hernandez-Bogantes and M. Masis (2013). "Classification of diabetic retinopathy and diabetic macular edema." World journal of diabetes **4**(6): 290-294.

Xu, K. and O. Cleaver (2011). "Tubulogenesis during blood vessel formation." Semin Cell Dev Biol **22**(9): 993-1004.

Zahedmanesh, H. and C. Lally (2011). "A multiscale mechanobiological modelling framework using agent-based models and finite element analysis: application to vascular tissue engineering." Biomechanics and modeling in mechanobiology.

Zhang, X. and R. Z. Gan (2011). "A comprehensive model of human ear for analysis of implantable hearing devices." IEEE transactions on bio-medical engineering **58**(10): 3024-3027.

Zheng, X., S. M. Wise and V. Cristini (2005). "Nonlinear simulation of tumor necrosis, neo-vascularization and tissue invasion via an adaptive finite-element/level-set method." Bull Math Biol **67**(2): 211-259.

# APPENDICES

# **APPENDIX I**

## **REPLACING THE BAR GRAPH**

**Acknowledgements: William Green<sup>†</sup>, Elizabeth O'Brien<sup>†</sup>, Angela Jividen<sup>\*</sup>,  
Jeana Ripple<sup>†</sup>, Shayn M. Peirce<sup>\*</sup>**

**<sup>\*</sup>University of Virginia, Department of Biomedical Engineering**

**<sup>†</sup>University of Virginia, School of Architecture**

Data display is an exercise in pragmatism. An author must balance the clarity of a message with its breadth of information in an effort to convey an idea or thought to an observer with high fidelity. Sacrificing either clarity or breadth can result in misinterpretation or misunderstanding, both of which undermine communication of technical material. Whether explicitly or implicitly, authors who draft graphs or figures of data display must engage in this editing process when preparing their work for presentation. Sometimes this drafting process results in becoming confounded by their own data when they are unable to share their observations with peers because they lack the tools to do so.

Through collaboration with the School of Architecture and support from the Jefferson Trust Big Data grant, I explored alternative methods for displaying multiparametric data sets generated by the ABM presented in Chapter 3. Traditional 2D data display methods proved unwieldy for presenting and analyzing the large datasets generated by performing multiparametric parameter space exploration – the density of data was so great that any attempt to plot on a Cartesian coordinate plane resulted in over plotting and over complexity (Figure I.1).

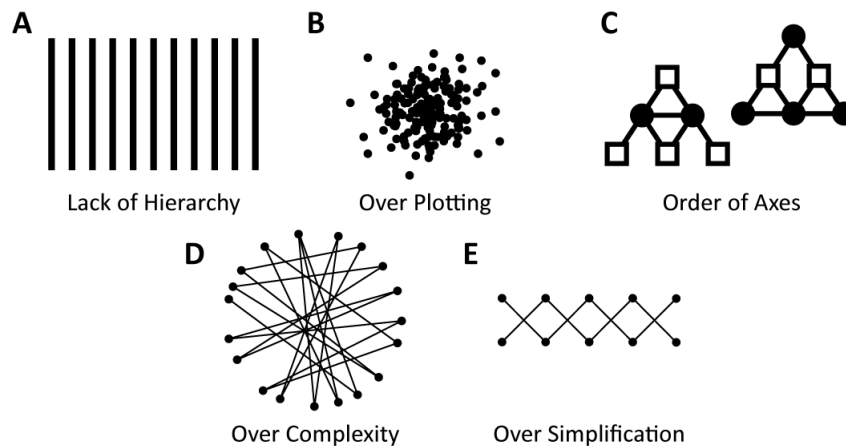


**FIGURE I.1: CHALLENGES DISPLAYING BIG DATA SETS**

A loss of dimensionality through parameter reduction can sometimes lead to a lack of hierarchy (A) or an over simplification that lacks complexity (E). Conversely, attempting to display an entire dataset can result in over plotting (B) or overly complex graphics (D). Finally, the order of axes in multiparametric data is an important consideration as it may change the shape of data trends, revealing or concealing important information (C).

Our collaboration generated a series of plotting alternatives based on a parallel coordinate systems approach. Parameter values are plotted radially along a series of parallel axes – specific parameter combinations are shown as lines crossing each axis at their respective values (Figure I.2A). Outputs from a simulation (e.g. accuracy of a modeling prediction for a parameter combination) are conveyed by the line weight or hue, thereby preserving the breadth of the dataset without over plotting the information. The most recent versions of this display technique have been dubbed “Lightning Plots” for their visual similarity to lightning strikes (Figure I.2B).

A case study in data visualization is currently in preparation based on this collaboration. The manuscript will include a review of data display methods and challenges (Figure I.1) for large data sets as well as introduce our specific Lightning Plot methodology. Further, A. Jividen and E. O’Brien have produced an online resource for compiling methods of data display that can be found at <http://explico.virginia.edu>. This website, Project Explico, will serve as a live version of the manuscript that can be updated with additional data display methods and resources over time.

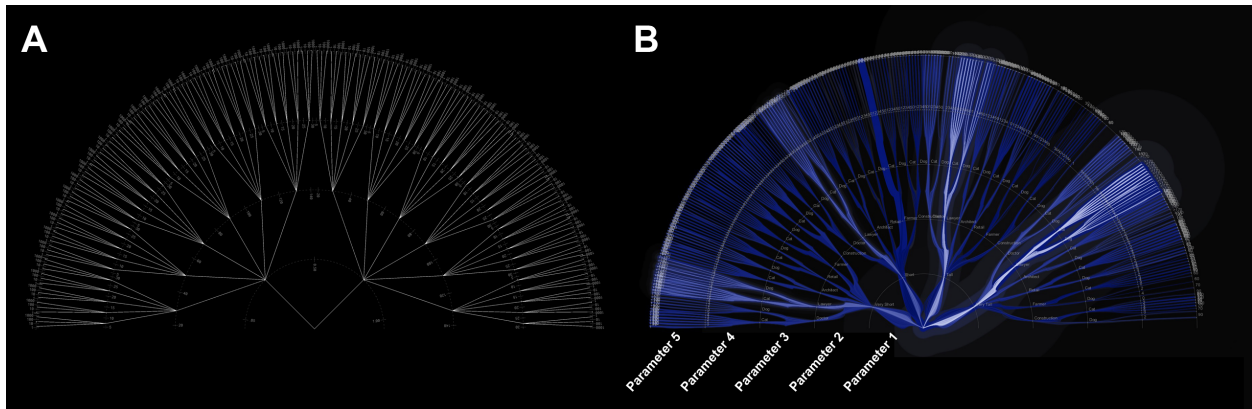


**FIGURE 1.2: LIGHTNING PLOT DESIGN**

Modified radial parallel coordinate phase space shown with lines connecting all possible parameter combinations (A). Phase space with example Lightning Plot where line hue represents density of data (i.e. how many times a parameter combination was tested) using a test dataset (B).

## APPENDIX II

### SCIENCE NEWS FOR STUDENTS: VIRTUAL WOUNDS: COMPUTERS PROBE HEALING

**Acknowledgement: Naila Moreira**

As part of an article reviewing the use of computational models in biology, I was interviewed by N. Moreira (*Science News for Students*) to discuss how an ABM might be used to study wound healing. In addition to providing a background of the immune process and how a prototypical skin abrasion might heal, I constructed a simple ABM for students to explore the process on their own (Figure II.1). By manipulating parameters such as the bacterial proliferation rate, the user is able to observe the time course of an immune response.

Under certain conditions (i.e. highly infectious bacteria, poor immune response) the infection lingers and enters a steady state where the immune system is unable to properly clear the bacterial load, as might be seen in an immunocompromised patient. Conversely, with a healthy immune response the infection is cleared following a typical progression of neutrophil invasion followed by macrophage recruitment. Between these two extremes (swift healing and latent infection) there are many other system behaviors to be explored based on chosen parameter values. For example, the duration of infection is highly dependent on initial bacterial load and proliferation rate.

This work has been published as: Moreira, Naila. "Virtual wounds: Computers probe healing." *Science News for Students*. The Society for Science and the Public. January 16, 2015.

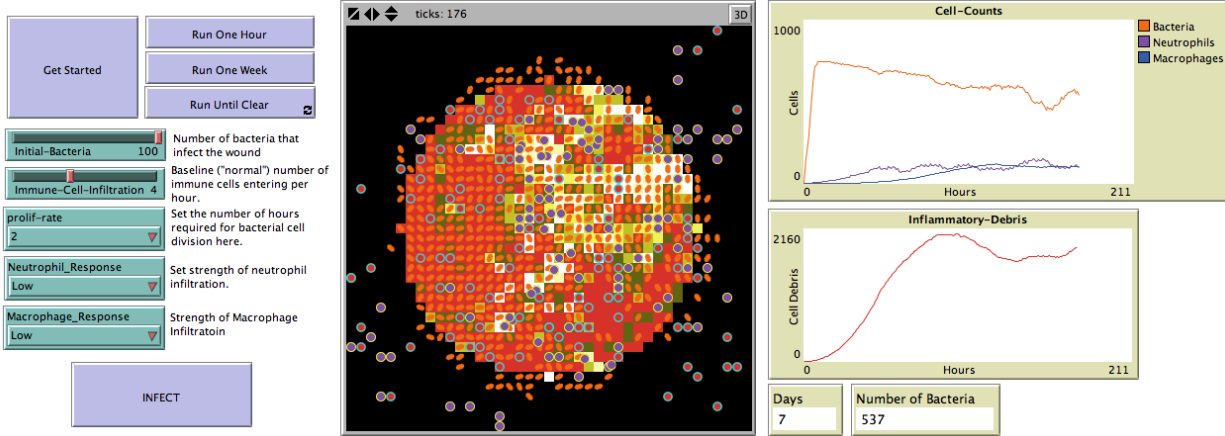


**FIGURE II.1 VIRTUAL WOUND MODEL**

A snapshot of the interface of the Virtual Wound Model for students. The user can select the duration of the simulation (one hour, one week, or until resolved), the initial bacterial load, the immune cell infiltration rate, the proliferation rate of bacteria, and the effectiveness of either the macrophage or neutrophil response. A visualization of the wound shows the various cell types interacting spatially, while graphs plot the population size of each cell type and the amount of inflammatory debris (e.g. necrotic tissue). This interface was designed for a primary school student to explore the fundamental immune response to a skin abrasion.

## VIRTUAL WOUND MODEL NETLOGO CODE

```
globals
[
  clock
  generations          ; a counter to keep track of the number of times the cells have
5  divided
  number-of-cells      ; a counter used to keep track of the number of total cells in
the world
  Migration-Probability
  Macrophage-Strength
10  Neutrophil-Homing-Range
  ShowDebris
]

15  breed [bacteria bacterium]          ; this is the sub-category of turtles that are
bacterial cells
breed [neutrophils neutrophil]        ; this is the first wave of immunes cells, they
release anti-microbial cytokines and can also phagocytose bacteria
20  breed [macrophages macrophage]      ; this is the second wave of immune cells, the
phagocytes that "clean up" debris and remove aged neutrophils

turtles-own [age]                    ; a counter to keep track of turtles age after dividing
(replaces "clock")
patches-own [
25  debris                          ; all dead cell become "debris" that must be removed to fully
heal the wound
  wound                            ; only a subset of patches are in the "Wound" and this
represents where bacteria can enter from
]
30  to setup
    __clear-all-and-reset-ticks      ; clear all
    ask patch 0 0 [ask patches in-radius 15 [set wound 1 set pcolor red]]

35  if Neutrophil_Response = "Low" [create-neutrophils ceiling (.1 * Immune-Cell-
Infiltration)]
    if Neutrophil_Response = "Normal" [create-neutrophils ceiling (1 * Immune-Cell-
Infiltration)]
40  if Neutrophil_Response = "High" [create-neutrophils ceiling (2 * Immune-Cell-
Infiltration)]

    ask neutrophils
    [
45  setxy random-xcor random-ycor      ; randomize turtle locations to locations
within the boundaries of the world
    setxy pycor pxcor                ; place the turtles on the center of each
patch
    set shape "neutrophil"           ; denote the shape of the turtle as an
bacteria cell shape
50  set age 1
    ]

    set Migration-Probability 70
    set Macrophage-Strength 3
55  set Neutrophil-Homing-Range 1
    set ShowDebris true
end

to Run-Simulation
60  proliferate-bacteria
    proliferate-neutrophils
    proliferate-macrophages
    migrate
```

```

Leukocyte-Actions
65   if any? bacteria [
      if Neutrophil_Response = "Low" and ticks mod 3 = 0 [create-neutrophils ceiling (.1
* Immune-Cell-Infiltration) [setxy random-xcor random-ycor setxy pycor pxcor set shape
"neutrophil" set age 1]]
70     if Neutrophil_Response = "Normal" [create-neutrophils ceiling (1 * Immune-Cell-
Infiltration)[setxy random-xcor random-ycor setxy pycor pxcor set shape "neutrophil"
set age 1]]
      if Neutrophil_Response = "High" [create-neutrophils ceiling (2 * Immune-Cell-
75 Infiltration) [setxy random-xcor random-ycor setxy pycor pxcor set shape "neutrophil"
set age 1]]

    ]

      if any? patches with [debris > 0 and ticks > 24] [
80     if Macrophage_Response = "Low" and ticks mod 3 = 0 [create-macrophages ceiling (.1
* Immune-Cell-Infiltration) [setxy random-xcor random-ycor setxy pycor pxcor set shape
"macrophage" set age 1]]
      if Macrophage_Response = "Normal" [create-macrophages ceiling (1 * Immune-Cell-
85 Infiltration)[setxy random-xcor random-ycor setxy pycor pxcor set shape "macrophage"
set age 1]]
      if Macrophage_Response = "High" [create-macrophages ceiling (2 * Immune-Cell-
Infiltration) [setxy random-xcor random-ycor setxy pycor pxcor set shape "macrophage"
set age 1]]

90   ]

    ifelse ShowDebris                                ;set patches to report debris by
color
    [ask patches with [wound = 1 and debris > 0][set pcolor scale-color yellow debris 0
95 5]] ;scale patch color based on amount of debris
    [ask patches [set pcolor black]]
    ask patches with [wound = 1 and debris = 0][set pcolor red] ;reset patch color to
red or black based on previous wound state
100  ask patches with [wound = 0 and debris = 0][set pcolor black]

    ask neutrophils with [age > 48][if 100 * (age / 96) > random 100 [die ask patch-here
[set debris debris + 1]]]
105  ask macrophages with [age > 96][if 100 * (age / 192) > random 100 [die]]
    ask patches [if debris < 0 [set debris 0]]

    ask turtles [set age age + 1]
    set number-of-cells count bacteria                ; this counts the total number of
bacteria cells, which is shown in the counter window below the main world.
110  set clock clock + 1
    tick

end

115  to infect
    ask patch 0 0 [
      ask n-of Initial-Bacteria patches in-radius 15[
        sprout 1                ; create the number of initial bacteria as designated by the
slider on the interface tab
120      [
        set breed bacteria                ; denote the 'breed' of the turtle as an
"bacteria" cell
        set shape "bacteria"            ; denote the shape of the turtle as an
bacteria cell shape
125      set age random prolif-rate
        ]
      ]
    ]
  ]

```

```

130 end

to proliferate-bacteria          ; this sub-routine simulates cell proliferation
without any contact inhibition [
  ask bacteria [
135   if age mod proliferate-rate = 0 and count bacteria-on neighbors < 8          ;
cell division happens for every cell at the same time (i.e. clock tick) according to
the 'prolif-rate' set on the interface tab. See 'proliferate' sub-routine below.
    [
      hatch 1 [
140       let attempted-moves 0
          while [any? other bacteria-here and attempted-moves < 16]
            [
145              if not any? neighbors with [wound = 1 and not any? bacteria-here][die]
                move-to one-of neighbors with [wound = 1 and not any? bacteria-here]
                set attempted-moves attempted-moves + 1]
            ]
          ]
    ]
  ]
150 end

to proliferate-neutrophils      ; this procedure simulates cell
proliferation with contact inhibition for neutrophils
  ask neutrophils [
155   if age mod 6 = 0 and age < 48 and count neutrophils-on neighbors = 0
    [
      hatch 1 [
160       let attempted-moves 0
          while [any? other neutrophils-here and attempted-moves < 16]
            [
                move-to one-of neighbors with [not any? neutrophils-here]
                set attempted-moves attempted-moves + 1]
            ]
          ]
    ]
  ]
165 ]
end

170 to proliferate-macrophages  ; this procedure simulates cell
proliferation with contact inhibition for macrophages
  ask macrophages [
    if age mod 15 = 0 and age < 48 and count macrophages-on neighbors = 0
      [
175       hatch 1 [
          let attempted-moves 0
          while [any? other macrophages-here and attempted-moves < 16]
            [
180              move-to one-of neighbors with [not any? macrophages-here]
                set attempted-moves attempted-moves + 1]
            ]
          ]
      ]
    ]
185 ]
end

to migrate
  if random 100 <= migration-probability          ; migration is probabalistic based
on a slider value
  [
    ask bacteria
    [

```

```

195         if any? neighbors with [not any? bacteria-here and wound = 1] ;
migration only occurs if there is at least one empty neighboring patch
        [
            move-to one-of neighbors with [not any? bacteria-here] ; migrate to one of the
            8 neighboring patches without a cell in it already
        ]
200     ]
    ]

    ask neutrophils ;neutrophils move towards bacteria in their homine range, or to a
205 random neighboring patch
    [
        ifelse any? bacteria in-radius Neutrophil-Homing-Range [
            face min-one-of bacteria [distance myself]
            fd 1
        ]
210     [move-to one-of neighbors]
    ]

    ask macrophages
215     [
        ifelse any? bacteria-on neighbors or any? neighbors with [debris > 0]
        [move-to one-of neighbors with [any? bacteria-here or debris > 0]]
        [move-to one-of neighbors]
    ]
220 end

to Leukocyte-Actions
    ask neutrophils [if any? bacteria-on patch-here
225     [
        ask patch-here [set debris debris + (count bacteria-here)]
        ask bacteria-on patch-here [die]
    ]
    ]

230 ask macrophages [if any? bacteria-on patch-here
    [ask bacteria-on patch-here [die]]
    if [debris] of patch-here > 0
    [ask patch-here [set debris debris - Macrophage-Strength]]
235 ]
end

```

## APPENDIX III

### NETLOGO CODE FOR EMBRYOID BODY SIMULATIONS

```
breed [leader leaders]
breed [follower followers]
breed [nucleus nuclei]
breed [tip-cell tip-cells]
5  globals [InitialConditionsFile counter location_x location_y my-ID move-OK? start_x
start_y mitosis-counter recording ESCAPE? DIRECTORY
    basal-sVEGFR1-Production basal-mVEGFR1-Production basal-VEGFR2-Production basal-
dll4-production basal-notch-activity sVEGFR1-EC-Production mVEGFR1-EC-Production
10  kNotch kVEGFR]
turtles-own [cell-ID pulling-force leader-state age VEGFR2 polarity VEGFR2-activity
mVEGFR1-activity NOTCH-activity NOTCH-activity-rate sVEGFR1 Dll4-activity]
nucleus-own [NOTCH-input NOTCH-production NOTCH-production-rate DLR4-production
VEGFR2-production mVEGFR1-production sVEGFR1-production Dll4-production DLL4-
production-rate]
15  links-own [link-ID]
patches-own [VEGF sVEGFR trueSproutLocation]
undirected-link-breed [membrane membranes]
undirected-link-breed [cell-to-cell cell-to-cells]
directed-link-breed [cyto cytos]
20  cell-to-cell-own [NOTCH]

to RESET
    clear-all
25  reset-ticks
    file-close-all
end

to Setup
30  if not Use-Current-Directory? [set-current-directory user-directory]
    set recording false

    set InitialConditionsFile "WT11Q1world.csv"
35  Make-Cell

    let EC-Surface-Area 962E-8 ;cm^2, from Adamson RH 1993
    set sVEGFR1-EC-Production 2.8E-10 ;nmol cm^-2 s^-1 Hashambhoy 2011
40  set mVEGFR1-EC-Production 2.8E-10 ;nmol cm^-2 s^-1 Hashambhoy 2011
    set basal-sVEGFR1-Production EC-Surface-Area * sVEGFR1-EC-Production ; nmol/s
    set basal-mVEGFR1-Production EC-Surface-Area * mVEGFR1-EC-Production ; nmol/s
    set basal-VEGFR2-Production EC-Surface-Area * mVEGFR1-EC-Production * 3 ;based on 3x
insertion rate from Mac Gabhann 2003
45  set basal-dll4-production 1e-16
    set basal-notch-activity 1e-16

    if RunGeneticAlg? [importGenAlgParameters]

50  ask nucleus [
    set sVEGFR1-production basal-sVEGFR1-production
    set mVEGFR1-production basal-mVEGFR1-production
    set VEGFR2-production basal-VEGFR2-production
    set DLL4-production basal-DLL4-production
55  set NOTCH-activity basal-NOTCH-activity

    ask out-cytos-neighbors [
        set notch-activity basal-notch-activity / 8
```

```

60         set dll4-activity basal-dll4-production / 8
        ]
    ]
    ask patches [set trueSproutLocation 0]
65    importSproutLocations
    reset-ticks
end

to Go
70    ;set-current-directory "C:\\Users\\jbw2w\\Dropbox\\2012-12-07-Test"
    ;while [not file-exists? "Ready-for-ABM.txt"][wait 5]
    ;file-delete "Ready-for-ABM.txt"
    ;Input-From-PDE ;Reads files from PDE simulation (without PDE input,
calculates VEGF gradients)
75    make-gradient ;Surrogate VEGF Production (not using PDE values)
    Calculate-Rates ;Calculates production rates based on NOTCH and VEGF
activation, Polarity Matrix
    Follow-Gradient ;Cells move up VEGFR2 activity gradient
    Adjust-Connections ;Geometries of connections are curated
80    ;Output-To-PDE ;Sends Geometry, Production rates, and FLAG file to PDE
    tick

end

85    ;Follow-Gradient governs the movement of cells in response to [VEGF] in patches
to Follow-Gradient
;New gradient code: determine the membrane element with highest VEGF concentration and
the membrane element with lowest VEGF concentration.
90    ;Next, set the heading of the membrane with highest VEGF to be that of the dx/dy
between lowest and highest membrane elements.
;Essentially, this sets the trajectory of the cell in the direction of the steepest
gradient accross the cell.

95    ask nucleus [
        let highest-activity max-one-of out-link-neighbors [VEGFR2-activity]
        let lowest-activity min-one-of out-link-neighbors [VEGFR2-activity]
        ;show [VEGFR2-activity] of highest-activity - [VEGFR2-activity] of lowest-
activity
100        if ([VEGFR2-activity] of highest-activity - [VEGFR2-activity] of lowest-
activity) >= (VEGF-Tolerance * 10) [
            let delta-x ([xcor] of highest-activity - [xcor] of lowest-activity)
            let delta-y ([ycor] of highest-activity - [ycor] of lowest-activity)
105            ask max-one-of out-link-neighbors [VEGFR2-activity] [
                set leader-state 2
                if delta-x = 0 and delta-y > 0 [set heading 0]
                if delta-x = 0 and delta-y < 0 [set heading 180]
110                if delta-y = 0 and delta-x > 0 [set heading 90]
                if delta-y = 0 and delta-x < 0 [set heading 270]
                if delta-x != 0 and delta-y != 0 [set heading tan (delta-x / delta-y)]
                movement 1.25
                set breed tip-cell
115                set shape "circle"
            ]
            if leader-state = 0 [
                output-type ticks output-type " " output-type (round((xcor + max-pxcor) * 100)
120 / 100) output-type " " output-print (round((ycor + max-pycor) * 100) / 100)
                set leader-state 1
            ]
        ]
    ]

```

```

125     ]
end

;Make-Cell is the code used to generate a nucleus linked to 8 membrane nodes at an
130 input location.
;The nucleus, membrane nodes and all links share the same Cell-ID or Link-ID for
identification
to Make-Cell
  if Initial-Position = "Random"
135   [
      set start_x 0 set start_y -15

      repeat num_of_cells [
140         create-nucleus 1 [
            set location_x start_x + 2 - random 5
            set location_y start_y + 2 - random 5
            set cell-ID count nucleus
            setxy location_x location_y
145             set color red
            set shape "circle"
            set Notch-production 1
            set DLR4-production 1
            set VEGFR2-production 1
150             set sVEGFR1-production 1
            set mVEGFR1-production 1

            ;The nuclei must be placed to avoid overlap or edge compression of the membrane:
            while [any? other turtles in-radius 6 OR (abs xcor) > (max-pxcor - 3) OR (abs
155 ycor) > (max-pycor - 3) OR (ycor) > -5 or ycor < -25][
                let old-x location_x
                let old-y location_y
                set location_x location_x + 1 - random 3
                set location_y location_y + 1 - random 3
                carefully [setxy location_x location_y][set location_x old-x set location_y
160 old-y]
            ]
        ]
      ]
      ;Generate the 8 Membrane elements in a circle around the nucleus:
165 create-ordered-follower 8 [
          set cell-ID count nucleus
          set polarity 1
          set color blue
          set shape "circle"
          setxy location_x location_y
170          jump 3]
      ask nucleus with [cell-ID = count nucleus][
          create-cyto-to follower with [cell-ID = count nucleus]
          ask my-out-links [set link-ID count nucleus set color red]
          ask out-link-neighbors [
175             while [(count my-links) < 3] [
                create-membrane-with min-n-of 2 other (follower with [cell-ID = [cell-ID] of
myself]) [distance myself]
                ask my-membrane [set link-ID count nucleus set color blue set thickness .3]
            ]
          ]
180      ]
      ask follower with [cell-ID = count nucleus AND count my-cell-to-cell = 0][
          let neighbor min-one-of follower with [(cell-ID != [cell-ID] of myself) AND (count
my-cell-to-cell = 0)] [distance myself]
185          carefully [
              if distance neighbor < 3 [
                  create-cell-to-cells-with neighbor [set color green]
                  ask my-cell-to-cell[

```

```

190         if any? other links with [crossed? self myself]
            [die]
        ]
    ]
  ][]
]
195 ]
]
if Initial-Position = "User-Defined"
[
200   repeat num_of_cells [
        set counter true
        while [counter] [
205   counter false]
            if mouse-down? [set location_x mouse-xcor set location_y mouse-ycor set
                wait 0.1
            ]

210   create-nucleus 1 [
        set cell-ID count nucleus
        setxy location_x location_y
        set color red
        set shape "circle"
215   set Notch-production 1
        set DLR4-production 1
        set VEGFR2-production 1
        set sVEGFR1-production 1
        set mVEGFR1-production 1

220   ;The nuclei must be placed to avoid overlap or edge compression of the membrane:
        while [any? other turtles in-radius 6 OR (abs xcor) > (max-pxcor - 3) OR (abs
225   ycor) > (max-pycor - 3)][
            let old-x location_x
            let old-y location_y
225   set location_x location_x + 1 - random 3
            set location_y location_y + 1 - random 3
            carefully [setxy location_x location_y][set location_x old-x set location_y
230   old-y]
        ]
    ]
    ;Generate the 8 Membrane elements in a circle around the nucleus:
    create-ordered-follower 8 [
235   set cell-ID count nucleus
        set polarity 1
        set color blue
        set shape "circle"
        setxy location_x location_y
        jump 3]
    ask nucleus with [cell-ID = count nucleus][
240   create-cyto-to follower with [cell-ID = count nucleus]
        ask my-out-links [set link-ID count nucleus set color red]
        ask out-link-neighbors [
            while [(count my-links) < 3] [
245   myself]) [distance myself]
                create-membrane-with min-n-of 2 other (follower with [cell-ID = [cell-ID] of
                    ask my-membrane [set link-ID count nucleus set color blue set thickness .3]
                ]
            ]
        ]
    ]
250   ask follower with [cell-ID = count nucleus AND count my-cell-to-cell = 0][
        let neighbor min-one-of follower with [(cell-ID != [cell-ID] of myself) AND (count
my-cell-to-cell = 0)] [distance myself]
        carefully [

```

```

255     if distance neighbor < 3 [
        create-cell-to-cells-with neighbor [set color green]
        ask my-cell-to-cell[
            if any? other links with [crossed? self myself]
                [die]
        ]
260     ]
    ][]
]
]
]
265 if Initial-Position = "Import"
[
    let VEGF-tolerance-hold VEGF-Tolerance
    let DLL4-TO-NOTCH-FACTOR-hold DLL4-TO-NOTCH-FACTOR
270 ;import-world WT11Q1start.csv
    import-world InitialConditionsFile
    set VEGF-Tolerance VEGF-tolerance-hold
    set DLL4-TO-NOTCH-FACTOR DLL4-TO-NOTCH-FACTOR-hold
275 random-seed timer
    reset-ticks
]

280 if Initial-Position = "Fixed"
[
    file-open "Fixed-Positions.txt"
    set counter true
285 while [counter][

        create-nucleus 1 [
            set cell-ID count nucleus
            set location_x file-read
290 set location_y file-read
            if file-at-end? [set counter false]

            set Notch-production 1
            set DLR4-production 1
295 set VEGFR2-production 1
            set sVEGFR1-production 1
            set mVEGFR1-production 1
            setxy location_x location_y
            set color red
300 set shape "circle"
        ]
        ;Generate the 8 Membrane elements in a circle around the nucleus:
        create-ordered-follower 8 [
            set cell-ID count nucleus
305 set polarity 1
            set color blue
            set shape "circle"
            setxy location_x location_y
            jump 3]
310 ask nucleus with [cell-ID = count nucleus][
            create-cyto-to follower with [cell-ID = count nucleus]
            ask my-out-links [set link-ID count nucleus set color red]
            ask out-link-neighbors [
                while [(count my-links) < 3] [
315 create-membrane-with min-n-of 2 other (follower with [cell-ID = [cell-ID] of
myself]) [distance myself]
                    ask my-membrane [set link-ID count nucleus set color blue set thickness .3]
                ]
            ]
        ]
    ]
]
]

```

```

320     ]
    ]
    ask follower with [cell-ID = count nucleus AND count my-cell-to-cell = 0][
    let neighbor min-one-of follower with [(cell-ID != [cell-ID] of myself) AND (count
my-cell-to-cell = 0)] [distance myself]
    carefully [
325       if distance neighbor < 3 [
          create-cell-to-cells-with neighbor [set color green]
          ask my-cell-to-cell[
            if any? other links with [crossed? self myself]
330             [die]
          ]
        ]
      ][]
    ]
  ]
335  file-close
]

end

340  ; MOVEMENT is the procedure for any turtle to proceed forward.  It receives [dist] as
you would for jump or bk,
; however it checks to make sure that moving forward does not cause illegal overlaps
within the cell
to movement [dist]
345  jump dist
    set my-ID cell-ID
    set move-OK? false
    ;First make sure that moving won't cause the cell shape to invert on itself
    ;while [move-OK? = false][
350  ask links with [link-ID = my-ID][
    ifelse any? other links with [crossed? self myself] ;calls crossed? procedure to
determine if links are crossed
    [set move-OK? false] ;if crossed, don't move
    [set move-OK? true] ;if not crossed, moving is OK
355  ]
    ;Second, make sure that leaders don't pass through another cell to get to the
chemokine
    if breed = leader [
      ask my-links [
360        ifelse any? other links with [crossed? self myself]
          [set move-OK? false]
          [set move-OK? true]
        ]
      ]
    ]
365  ;Third, make sure that the movements does not over-extend the cell membrane
    if any? my-membrane with [link-length > Max-Link-Length]
    [set move-OK? false]
    ifelse move-OK? []
    [jump -1 * dist] ;set heading random 360 jump 0.5]
370  ;]
end

;Adjust-Connections curates intercellular links (adds/subtracts as definted by
length/tension)
375 ;and also adjusts the distance between link neighbors of all types
;Adjust-Conncetions also call the Mitosis command for cells that have grown too large

to Adjust-Connections
;Firstly, make new connections with neighboring cells that are within a critical
380 distance
    ask-concurrent turtles [if age > 0 [set age age - 1]]
    ask-concurrent turtles with [count my-cell-to-cell = 0][

```

```

    let neighbor min-one-of turtles with [(cell-ID != [cell-ID] of myself) AND (count
385 my-cell-to-cell = 0)] [distance myself]
    carefully [
        if distance neighbor < 6 [
            create-cell-to-cells-with neighbor [set color green]
            ask-concurrent my-cell-to-cell[
                if any? other links with [crossed? self myself]
390 [die]
            ]
        ]
    ][]
]
395
;Set Notch level of cell-to-cell links based on the type of cell they are connected
to
ask-concurrent cell-to-cell [
    ifelse [breed] of end1 = tip-cell OR [breed] of end2 = tip-cell [set NOTCH 2][set
400 NOTCH 1]
]

;Next, adjust the distances between linked turtles
ask follower [
405 let furthest max-one-of membranes-neighbors [distance myself]
    if distance furthest > 3 [face furthest movement [distance myself] of furthest /
3]

    carefully[
410 set furthest max-one-of cell-to-cells-neighbors [distance myself]
        if distance furthest > 0.5 and [breed] of furthest = tip-cell [face furthest
movement [distance myself] of furthest / 3]
        if distance furthest > 0.5 and [breed] of furthest != tip-cell [face furthest
movement [distance myself] of furthest / 3]][]
415 ]

;break cell-to-cell links that cross, become too long, or that orginate from the
same cell
ask-concurrent cell-to-cell [
420 if link-length > Max-Link-Length [die]
    if any? other links with [crossed? self myself] [die]
]
ask-concurrent turtles [
425 if count my-cell-to-cell > 1 [
    ask one-of my-cell-to-cell [die]
]
]

ask-concurrent tip-cell[
430 let furthest max-one-of membranes-neighbors [distance myself]
    if distance furthest > 3 and [breed] of furthest = leader [face furthest movement
0.6]
    if distance furthest > 3 and [breed] of furthest != leader [face furthest movement
0.5]
435 ]
ask-concurrent nucleus [
    let furthest max-one-of out-link-neighbors [distance myself]
    if distance furthest > 3 and [breed] of furthest = leader [
        face furthest movement 0.5
440 ]
    if distance furthest > 3 and [breed] of furthest != leader [
        face furthest movement 0.25
    ]
]
445 ;Finally, adjust distances by moving away from agents that are too close
ask-concurrent turtles [
    let closest min-one-of other turtles [distance myself]

```

```

    if distance closest < 2 AND (not cell-to-cells-neighbor? closest) [
      face closest movement -0.75
450   if distance closest < 0.1 AND (cell-to-cells-neighbor? closest) [
        face closest movement -0.1
      ]
    ]
  ]
455 ]

;Call Cell Division command based on the size of a cell and it's age (i.e. cell
cannot have divided recently)
;ask-concurrent nucleus with [sum [link-length] of my-out-links > Mitosis-Threshold
and all? out-link-neighbors [breed = follower]] [divide [cell-ID] of self]
460 end

;Cell Division;

to divide [ID]
465   set mitosis-counter mitosis-counter + 1
      let max-ID max [cell-ID] of nucleus + 1
      ask follower with [cell-ID = ID and any? my-cell-to-cell][
        set pulling-force [link-length] of max-one-of my-cell-to-cell [link-length]
      ]
470   repeat 30[
ask-concurrent follower with [cell-ID = ID]
[
475     let closest min-one-of membranes-neighbors [distance myself]
        let furthest max-one-of membranes-neighbors [distance myself]
        if distance closest < 4 [face closest jump -.25]
        if distance furthest > 4 [face furthest jump .25]
      ]
ask-concurrent nucleus with [cell-ID = ID]
480 [
      let closest min-one-of out-cytos-neighbors [distance myself]
      let furthest max-one-of out-cytos-neighbors [distance myself]
      if distance closest < 5.2 [ask closest [face myself jump -.25]]
      if distance furthest > 5.2 [ask furthest [face myself jump .25]]
485   ]
  ]

490 ;First, identify the followers that will become part of the daughter cells and which
will retain parent cell-ID
ask max-one-of turtles with [cell-ID = ID] [pulling-force][
  let furthest max-n-of 4 other turtles with [cell-ID = ID] [distance myself]
  ask furthest [
495    set cell-ID max-ID
    ask my-in-cyto [die]
  ]
]

500 ask nucleus with [cell-ID = ID] [
  hatch 1 [
    set cell-ID max-ID
    create-cyto-to other turtles with [cell-ID = [cell-ID] of myself][
      set color red
505    set link-ID [cell-ID] of myself
    ]
    facexy mean [pxcor] of out-link-neighbors mean [pycor] of out-link-neighbors
    movement (mean [link-length] of my-out-links) / 2
  ]
510 facexy mean [pxcor] of out-link-neighbors mean [pycor] of out-link-neighbors
    movement (mean [link-length] of my-out-links) / 2
  ]
]

```

```

;Delete links between the two cell membranes
515 ask membrane with [[cell-ID] of end1 != [cell-ID] of end2][die]

;generate new membranes
ask patch (mean list one-of [pxcor] of nucleus with [cell-ID = ID] one-of [pxcor]
of nucleus with [cell-ID = max-ID])
520 (mean list one-of [pycor] of nucleus with [cell-ID = ID] one-of [pycor] of
nucleus with [cell-ID = max-ID])[

    foreach [1.5 -1.5 3 -3 ][
        let $i ?
525         foreach [1 2][
            sprout-follower 1
            [
                set color blue
                set shape "Circle"
530                 face one-of nucleus with [cell-ID = ID]
                ifelse ? = 1
                [
                    jump .5
                    set cell-ID ID
535                 ]
                [
                    jump -.5
                    set cell-ID max-ID
                ]
540                 rt 90
                jump $i
            ]
        ]
    ]
545 ]

repeat 2[
    ask nucleus with [cell-ID = ID][
550         set age 10
        create-cyto-to follower with [cell-ID = ID]
        ask my-out-links [set link-ID ID set color red]
        ask-concurrent out-link-neighbors [
            if (count my-membrane) < 2 [
555             create-membranes-with min-one-of other follower with [cell-ID = [cell-ID] of
myself AND count my-membrane < 2] [distance myself]
            ask my-membrane [set link-ID ID set color blue set thickness .3]
            ]
        ]
    ]
560     ask nucleus with [cell-ID = max-ID][
        set age 10
        create-cyto-to follower with [cell-ID = max-ID]
        ask my-out-links [set link-ID max-ID set color red]
        ask-concurrent out-link-neighbors [
565             if (count my-membrane) < 2 [
                create-membranes-with min-one-of other follower with [cell-ID = [cell-ID] of
myself AND count my-membrane < 2] [distance myself]
                ask my-membrane [set link-ID max-ID set color blue set thickness .3]
            ]
        ]
570     ]
]
end

575 to-report crossed? [link-a link-b]
;; store nodes in variables for easy access
let a1 [end1] of link-a

```

```

let a2 [end2] of link-a
let b1 [end1] of link-b
580 let b2 [end2] of link-b
let nodes (turtle-set a1 a2 b1 b2)
;; if the links share a node, they don't cross
if 4 > count nodes [ report false ]
;; but if two nodes are on top of each other, we will say
585 ;; the links do cross (so you can't cheat that way)
if 4 > length remove-duplicates [list xcor ycor] of nodes
[ report true ]
;; if the ends of link-a are on opposite sides of link-b,
;; and the ends of link-b are on opposite sides of link-a,
590 ;; then the links cross
report [subtract-headings towards a2 towards b1 < 0 xor
subtract-headings towards a2 towards b2 < 0] of a1
and [subtract-headings towards b2 towards a1 < 0 xor
subtract-headings towards b2 towards a2 < 0] of b1
595 end

to Output-To-PDE
set DIRECTORY "C:\\Users\\jwb2w\\Dropbox\\2012-12-07-Test"
600 set-current-directory DIRECTORY
carefully[
file-delete (word "Cell-Locations.txt")
file-delete (word "sVEGFR1-Production.txt")
605 file-delete (word "mVEGFR1-Production.txt")
file-delete (word "VEGFR2-production.txt")
]
[]

610 file-open (word "Cell-Locations.txt")
foreach sort-on [cell-ID] nucleus [
ask ? [
file-type(word Cell-ID " ")
615 foreach sort out-cytos-neighbors [
ask ? [
file-type(word (round((xcor + max-pxcor) * 10) / 10) " " (round((ycor + max-
pycor) * 10) / 10) " "))
]
]
620 ]
file-print "\r"
]
file-close

625 file-open(word "sVEGFR1-production.txt")
foreach sort-on [cell-ID] nucleus [
ask ? [
file-type(word Cell-ID " ")
file-type(word (round(sVEGFR1-production * 1e19) / 1e19) " ")
630 foreach sort out-cytos-neighbors [
ask ? [
file-type(word polarity " ")
]
]
635 ]
file-print "\r"
]
file-close

640 file-open(word "mVEGFR1-production.txt")
foreach sort-on [cell-ID] nucleus [
ask ? [

```

```

file-type(word Cell-ID " ")
file-type(word (round(mVEGFR1-production * 1e19) / 1e19) " ")
645 foreach sort out-cytos-neighbors [
      ask ? [
        file-type(word polarity " ")
      ]
    ]
650 ]
file-print "\r"
]
file-close

655 file-open(word "VEGFR2-production.txt")
      foreach sort-on [cell-ID] nucleus [
        ask ? [
          file-type(word Cell-ID " ")
          file-type(word (round(VEGFR2-production * 1e19) / 1e19) " ")
660 foreach sort out-cytos-neighbors [
              ask ? [
                file-type(word polarity " ")
              ]
            ]
665 ]
      file-print "\r"
    ]
  file-close

670 file-open "Ready-for-PDE.txt"
      file-print "All yours!"
    file-close

675 set-current-directory (word DIRECTORY "\\ABM-History")
      set counter 1
      while [file-exists? (word "Cell-Locations-" counter ".txt")] [set counter counter +
1]
      file-open (word "Cell-Locations-" counter ".txt")
680 ;file-print "Cell-ID Node-1x Node1y Node-2x Node-2y Node-3x Node-3y Node-4x Node-4y
Node-5x Node-5y Node-6x Node-6y Node-7x Node-7y Node-8x Node-8y\r"
      foreach sort-on [cell-ID] nucleus [
        ask ? [
          file-type(word Cell-ID " ")
685 foreach sort out-cytos-neighbors [
              ask ? [
                file-type(word (round((xcor + max-pxcor) * 10) / 10) " " (round((ycor + max-
pycor) * 10) / 10) " "))
              ]
            ]
690 ]
      file-print "\r"
    ]
  file-close

695 file-open(word "sVEGFR1-production-" counter ".txt")
      foreach sort-on [cell-ID] nucleus [
        ask ? [
          file-type(word Cell-ID " ")
700 file-type(word (round(sVEGFR1-production * 1e19) / 1e19) " ")
          foreach sort out-cytos-neighbors [
            ask ? [
              file-type(word polarity " ")
            ]
          ]
705 ]
      ]
    file-print "\r"
  ]

```

```

]
file-close
710
file-open(word "mVEGFR1-production-" counter ".txt")
;file-print "Cell-ID mVEGFR1-production Polarity Matrix\r"
  foreach sort-on [cell-ID] nucleus [
    ask ? [
715    file-type(word Cell-ID " ")
    file-type(word (round(mVEGFR1-production * 1e19) / 1e19) " ")
    foreach sort out-cytos-neighbors [
      ask ? [
720        file-type(word polarity " ")
      ]
    ]
  ]
  file-print "\r"
]
725 file-close

file-open(word "VEGFR2-production-" counter ".txt")
;file-print "Cell-ID VEGFR2-production Polarity Matrix\r"
  foreach sort-on [cell-ID] nucleus [
730    ask ? [
    file-type(word Cell-ID " ")
    file-type(word (round(VEGFR2-production * 1e19) / 1e19) " ")
    foreach sort out-cytos-neighbors [
735      ask ? [
        file-type(word polarity " ")
      ]
    ]
  ]
  file-print "\r"
740 ]
file-close

file-open "Ready-for-PDE.txt"
file-print "All yours!"
745 file-close

end

750 to Input-From-PDE
  while [not file-exists? "pVEGFR1.txt"] [wait 0.1]
  file-open "pVEGFR1.txt"
  while [not file-at-end?][
    let current-cell file-read
755    ask nucleus with [cell-id = current-cell] [
      ;set mVEGFR1-activity file-read
      foreach sort out-cytos-neighbors [
        ask ? [set mVEGFR1-activity file-read ]
      ]
760    ]
  ]
  file-close
  file-delete "pVEGFR1.txt"

765 while [not file-exists? "pVEGFR2.txt"] [wait 0.1]
  file-open "pVEGFR2.txt"
  while [not file-at-end?][
    let current-cell file-read
    ask nucleus with [cell-id = current-cell] [
770      ;set VEGFR2-activity file-read
      foreach sort out-cytos-neighbors [
        ask ? [set VEGFR2-activity file-read]
      ]
    ]
  ]

```

```

    ]
  ]
775 ]

file-close
file-delete "pVEGFR2.txt"
780
end

to Calculate-Rates
ask nucleus [
785   set VEGFR2-activity sum [VEGFR2-activity] of out-cytos-neighbors
   set mVEGFR1-activity sum [mVEGFR1-activity] of out-cytos-neighbors

   ;let kVEGFR 1e13
   let max-DLL4 1e-14
790   let min-DLL4 1e-16
   VEGFR2-activity))
   set DLL4-production Delta-ODE DLL4-production VEGFR2-activity
ask out-cytos-neighbors [
795   set Dll4-activity [Dll4-production] of myself / 8
]

ask nucleus[

800   ;let kVEGFR 1e13
   ;let kNOTCH 1e13

   ask out-cytos-neighbors[
805     set NOTCH-activity sum ([Dll4-activity] of cell-to-cells-neighbors) * DLL4-TO-
     NOTCH-FACTOR
   ]
   set NOTCH-activity NOTCH-ODE NOTCH-activity sum ([NOTCH-activity] of out-cytos-
     neighbors)

810   let max-VEGFR2-production 1e-14
   let min-VEGFR2-production 1e-16
   let max-mVEGFR1-production 1e-14
   let min-mVEGFR1-production 1e-16
815   let max-sVEGFR1-production 1e-14
   let min-sVEGFR1-production 1e-16

   set VEGFR2-production (min-VEGFR2-production + (max-VEGFR2-production - min-
     VEGFR2-production) * (exp( - kNOTCH * (NOTCH-activity))))

820   set mVEGFR1-production (min-mVEGFR1-production + (max-mVEGFR1-production - min-
     mVEGFR1-production) * (1 - exp( - kNOTCH * NOTCH-activity)))
   set sVEGFR1-production (min-sVEGFR1-production + (max-sVEGFR1-production - min-
     mVEGFR1-production) * (1 - exp( - kNOTCH * NOTCH-activity)))
825 ]

end

830 to-report Delta-ODE [DLL4in pr2in]
  let kDLL4 .1
  let kr2 .1
  let kdegDLL4 .1
835 let maxDLL4 1e-14

  let DLL4 DLL4in

```

```

let pR2tot pR2in
repeat time[
840   let pR2 (pR2tot)
      let dDLL4 (kDLL4 * (maxDLL4) + kR2 * pR2 - kdegDLL4 * DLL4)
      set DLL4 (DLL4 + dDLL4)
]
845 report DLL4

end

to-report NOTCH-ODE [NOTCHin DLL4in]
850   let kDLL4 .1
      let kNOTCH* .1
      let kdegNOTCH .1
      let maxNOTCH 1e-14

855   let NOTCH* NOTCHin
      let DLL4tot DLL4in
      repeat time[
        let DLL4 (DLL4tot)
        let dNOTCH (kNOTCH* * (maxNOTCH ) + kDLL4 * DLL4 - kdegNOTCH * NOTCH*)
860       set NOTCH* (NOTCH* + dNOTCH)
      ]
      report NOTCH*
end

865 to make-gradient
      if remainder ticks 1 = 0 [
        let numpatch (count patches / 2)
        ask n-of numpatch patches [
870           let current-VEGF VEGF
              set VEGF (current-VEGF + (random-float 0.5 + 0.75) * VEGF-Production-Rate * 1e-7)
        ]
        ]
        diffuse VEGF 0.5

875 ask patches [
        set VEGF (VEGF - sVEGFR)
        if VEGF < 0 [set VEGF 0]
        ;set pcolor scale-color yellow VEGF 0 (10 * VEGF-Production-Rate * 1e-7)
880     ]

      ask nucleus [
        ask out-cytos-neighbors [
885           set VEGFR2 (VEGFR2 + ([VEGFR2-production] of myself * (random-float 0.5 +
0.75))) / 8]
        ]

      ask turtles with [breed = tip-cell or breed = follower] [
890         let receptors [VEGFR2] of self
          ifelse [VEGF] of patch-here >= receptors
            [set VEGFR2-activity receptors
              ask patch-here [set VEGF (VEGF - receptors)]]
            [set VEGFR2-activity ([VEGF] of patch-here)
              ask patch-here [set VEGF 0 ]]

895         set sVEGFR1 (sVEGFR1 + ([sVEGFR1-production] of one-of in-cytos-neighbors / 8))
          ask patch-here [set sVEGFR [sVEGFR1] of myself]
          set sVEGFR1 0

900       ]
        diffuse sVEGFR 0.25
end

```

```

to importSproutLocations
905   file-open "M1Q1sproutLocationsABM"
      while [not file-at-end?][
        let currentX file-read
        let currentY file-read

910     ask patch currentX currentY [ask patches in-radius 5 [set trueSproutLocation 1]]
      ]
      file-close
end

915 to exportTruePositives
      file-open "M1Q1truePositives"
      let truePositiveSprouts count nucleus with [leader-state = 1 and
[trueSproutLocation] of patch-here = 1]
      file-write truePositiveSprouts
920   file-close
end

to importGenAlgParameters
925   file-open "ParametersForABM"
      set DLL4-TO-NOTCH-FACTOR file-read
      set VEGF-Tolerance file-read
      set VEGF-Production-Rate file-read
      set kNotch file-read
      set kVEGFR file-read
930   file-close

end

```

## APPENDIX IV

### NetLogo Code for Retinal Angiogenesis Simulations

```
patches-own [astrocyte branchPoint EC PC VEGF tipCell NOTCH DLL4 VEGF_VEGFR1
VEGF_sVEGFR1 VEGFR1 VEGF_VEGFR2 VEGFR2 sVEGFR1 DLL4-input VEGFR2-production sVEGFR1-
production mVEGFR1-production originalColor]
globals [ECcount PCcount listOfECs listOfPCs leadingEdge listOfContacts
5 listOfNotchLevels listOfPhosphoR2 listOfDLL4Levels listOfTipCells maxVEGF
outputFileName VEGFR2list Pinsert VEGF_VEGFR1list]

;1 patch = sqrt(5) um x sqrt(5) um = 5 um^2

10 to setup
  instantiateVariables

  MakeAstrocyteTemplate
  MakeGradient
15 seedEC
  foreach listOfECs[repeat 5 [ECmove ?]]
  repeat 5 [
    MakeGradient
    maintainCellContacts
20 newReceptorBinding
    cellSignaling
  ]
  reset-ticks

25 end

to instantiateVariables
  clear-all
  set ECcount 0
30 ask patches [
  set astrocyte 0
  set branchPoint 0
  set EC 0
  set tipCell 0
35 set NOTCH 0
  set DLL4 0
  set VEGFR1 0
  set VEGFR2 0
  set VEGF_VEGFR2 0
40 set sVEGFR1 0
  set DLL4-input 0
  set VEGFR2-production 0
  set mVEGFR1-production 0
  set sVEGFR1-production 0
45 ]
  set listOfTipCells [ ]
  set listOfPCs [ ]
  set maxVEGF max [VEGF] of patches
end

50 to Go
  ;tip cells move more than non-tip cells
  set maxVEGF max [VEGF] of patches
  foreach listOfECs[
55 ifelse any? patches with [EC = ? and tipCell = 1]
    [repeat 4 [ECmove(?)] ;increased from 5 to 7
    [repeat 2 [ECmove(?)]]
```

```

]
maintainCellContacts
60 newReceptorBinding
cellSignaling

if ticks mod 2 = 0[makeGradient]
65 ask patches with [EC = 0 and PC = 0][
    set pcolor scale-color green VEGF 0 maxVEGF
]
ask patches with [tipCell = 1][set pcolor yellow]
ask patches with [EC != 0 and tipCell = 0][set pcolor originalColor]
70
set listofTipCells [ ]
foreach listofECs[
    if [tipCell] of one-of patches with [EC = ?] = 1
75 [set listofTipCells lput ? listofTipCells]
]

addNewCells

tick
80
if OutputData [updateOutputFile]
end

to MakeAstrocyteTemplate
85 ask n-of numberOfStartingBranches patches with [pycor = min-pycor] [sprout 1 [set
heading 0 + (random 90 - 45)]]
while [any? turtles] [
ask turtles [
90
    moveAndDraw 1
    if random 100 < branchProbability [
        hatch 1 [set heading heading + 20]
        set heading heading - 20
95
    ]
]
end

to seedEC
100 let startingPositions (list 5 15 25)
foreach startingPositions [
ask patches with [pycor = min-pycor + ? and remainder pxcor 5 = 0 and pxcor !=
max-pxcor][
105
    if remainder pxcor 20 = 0 [makeEC]
    ;if (not (remainder pxcor 22 = 0)) and (? = 5 or ? = 15) [ifelse random 100 <
25 [makeEC][makePC]]
]
]
foreach [10 20][
110
ask patches with [pycor = min-pycor + ? and remainder pxcor 10 = 0 and not
(remainder pxcor 20 = 0) and pxcor != max-pxcor][
    ifelse random 100 < 25 [makeEC]
    [
115
        if StartingCellLayout = "ECs" [makeEC]
        if StartingCellLayout = "ECandPC" [makePC]
        if StartingCellLayout = "SparseECs" [ ]
    ]
]
]
120
foreach listofECs [
    if not any? patches with [EC = ? and astrocyte = 1][

```

```

    ask patches with [EC = ?][
      set EC 0
125     set pcolor black
      set VEGFR1 0
      set VEGFR2 0
    ]
    set listOfECs remove ? listOfECs
130  ]
  ]
  foreach listOfPCs [
    if not any? patches with [PC = ? and any? neighbors with [EC != 0]][
      ask patches with [PC = ?][
135         set PC 0
          set pcolor black
        ]
        set listOfPCs remove ? listOfPCs
      ]
140  ]
end

to moveAndDraw [movement]
  repeat movement [
145    if patch-ahead 1 = NOBODY [die]
    if [pcolor] of patch-ahead 1 = blue [die]
    if [pycor] of patch-ahead 1 = max-pycor [die]
    ;if [pycor] of patch-ahead 1 = round (.25 * max-pycor) [die]
    ;if [pycor] of patch-here = round (.25 * max-pycor) [die]
150    ask patch-here [set pcolor blue set astrocyte 1]
    if random 100 < 25 [set heading heading + (random 40 - 20)]
    forward 1
  ]
155 end

to makeEC
  set ECcount ECcount + 1
  if listOfECs = 0 [set listOfECs (list 1)]
160  set listOfECs lput ECcount listOfECs
  set listOfECs remove-duplicates listOfECs
  let colorOfThisCell 12 + random-float 6
  set pcolor colorOfThisCell set EC (ECcount)
  let x pxcor
165  let y pycor
  ask patches with [pxcor < (x + 5) and pxcor > (x - 6) and pycor < (y + 5) and pycor
> (y - 6)][set pcolor colorOfThisCell set EC ECcount]
  ask patches with [EC = ECcount][
    set originalColor colorOfThisCell
170    set VEGFR2 100
    set VEGFR1 100
  ]
end

175 to makePC
  set PCcount PCcount + 1
  if listOfPCs = 0 [set listOfPCs (list 1)]
  set listOfPCs lput PCcount listOfPCs
  set listOfPCs remove-duplicates listOfPCs
180  let colorOfThisCell 102 + random-float 6
  set pcolor colorOfThisCell set PC (PCcount)
  let x pxcor
  let y pycor
  ask patches with [pxcor < (x + 5) and pxcor > (x - 6) and pycor < (y + 5) and pycor
185 > (y - 6)][set pcolor colorOfThisCell set PC PCcount]
  ask patches with [PC = PCcount][set originalColor colorOfThisCell]
end

```

```

to addNewCells
190   ask patches with [pycor = min-pycor + 5][
      let x pxcor
      let y pycor
      if not any? patches with [pxcor < (x + 5) and pxcor > (x - 6) and pycor < (y + 5)
and pycor > (y - 6) and (EC != 0 or PC != 0)][
195     ifelse random 100 < 50 [makeEC]
      [
        if StartingCellLayout = "ECs" [makeEC]
        if StartingCellLayout = "ECandPC" [makePC]
        if StartingCellLayout = "SparseECs" []
200     ]
      ]
    ]
end
205

to ECmove [ECnumber]
;Find patches that are adjacent to the EC border, then pick the one with highest
VEGF concentration to move to:
210   set leadingEdge patches with [EC = ECnumber and count neighbors with [EC = ECnumber]
=> 5 and any? neighbors with [EC = 0 and PC = 0]]
      let destination max-one-of patches with [any? neighbors with [member? self
leadingEdge] and EC = 0 and PC = 0][VEGF]
215     if is-patch? destination [
        let origin max-one-of patches with [EC = ECnumber][distance destination]

        if is-patch? origin
          [swapPatches origin destination]
220       ]
      ;Fill any gaps generated by EC movement:
      if any? patches with [EC = 0 and count neighbors with [EC = ECnumber] = 8][
        set destination one-of patches with [EC = 0 and count neighbors with [EC =
225       ECnumber] = 8]
        let origin max-one-of patches with [EC = ECnumber][distance destination]
        swapPatches origin destination
      ]
    end

230   to MakeGradient
      ask patches with [astrocyte = 1] [set VEGF VEGF + 1 ] ;VEGF production rate 5e-5
molecules/um^2 per second
      ask patches [
235         let kDegVEGF 0.001 ;VEGF solube degradation rate
        let dVEGF (- (VEGF * kDegVEGF))
        set VEGF VEGF + dVEGF
      ]
      repeat 5 [diffuse VEGF 0.4]
      set maxVEGF max [VEGF] of patches
240     if ShowVEGF[
        ask patches with [EC = 0 and PC = 0][
          set pcolor scale-color green VEGF 0 maxVEGF
        ]
      ]
245   end

to astroExport
set-current-directory("/Users/josephwalpole/Desktop/John Retinal
Model/astrocyteNetworkImages/Branching")
250   let num 1
      while [file-exists? (word "branchProb" branchProbability "astroImage" num ".png")]
[set num num + 1]

```

```

    export-view (word "branchProb" branchProbability "astroImage" num ".png")
end
255
to maintainCellContacts
  ;reinforce cell-cell contacts

  foreach listOfECs [
    let currentEC ?
    let contacts patches with [EC = ? and any? neighbors with [(EC != ? and EC != 0)
or PC != 0]]
    set listOfContacts ([EC] of patches with [any? neighbors with [EC = ?] and (EC !=
0 or PC != 0) and EC != ?])
265    set listOfContacts remove-duplicates listOfContacts

    foreach listOfContacts[
      let neighboringEC ?
      repeat 5 [
270        if count contacts with [any? neighbors with [EC = neighboringEC]] < 5 [
          ask contacts with [any? neighbors with [EC = neighboringEC]] [
            if any? neighbors with [EC = 0 and PC = 0][
              let destination min-one-of neighbors with [EC = 0 and PC = 0][distance
myself]
275              let origin max-one-of patches with [EC = currentEC and not any?
neighbors with [EC != currentEC and EC != 0]][distance destination]
              swapPatches origin destination
            ]
          ]
        ]
      ]
    ]
  ]

285  foreach listOfPCs[
    let currentPC ?
    let contacts patches with [PC = ? and any? neighbors with [EC != 0]]
    set listOfContacts ([EC] of patches with [any? neighbors with [PC = ?] and EC !=
0])
290    set listOfContacts modes listOfContacts

    repeat 5 [

      foreach listOfContacts[
295        let neighboringEC ?
          if count contacts with [any? neighbors with [EC = neighboringEC]] < 20 [
            ask contacts with [any? neighbors with [EC = neighboringEC]] [
              if any? neighbors with [EC = 0 and PC = 0][
                let destination min-one-of neighbors with [EC = 0 and PC = 0][distance
300 myself]
                let origin max-one-of patches with [PC = currentPC and not any?
neighbors with [EC = neighboringEC]][distance destination]
                swapPatches origin destination
              ]
            ]
          ]
        ]
      ]
    ]
  ]
  ; while [objects? currentPC > 1][
310  ;   ask one-of patches with [PC = 0 and EC = 0 and count neighbors with [PC =
currentPC] > 4][
  ;
  ;   let destination self
  ;   let origin one-of neighbors with [PC = currentPC]
315  ;   swapPatches origin destination
  ;
  ; ]

```

```

;    ]
]
320   ;Kill any ECs that are no longer in contact with the network:
      foreach listOfECs [
        if not any? patches with [EC = ? and any? neighbors with [EC != ? and (EC != 0 or
325   PC != 0)]]
          [ask patches with [EC = ?]
            [
              set EC 0
              set pcolor scale-color green VEGF 0 maxVEGF
              set EC 0
330             set DLL4 0
              set NOTCH 0
              set VEGF_VEGFR2 0
              set VEGFR2 0
              set VEGFR1 0
335             set tipCell 0
              set VEGFR2-production 0
              set sVEGFR1-production 0
              set mVEGFR1-production 0
              set originalColor 0
340             set TipCell 0
            ]
            set listOfECs remove ? listOfECs
          ]
        ]
345   end

to cellSignaling
  set listOfNotchLevels (list 0)
350   set listOfPhosphoR2 (list 0)
  set listOfDLL4Levels (list 0)
  set VEGFR2list (list 0)
  set VEGF_VEGFR1list (list 0)

355   foreach listOfECs[
    let currentEC ?
    let contacts patches with [EC != currentEC and EC != 0 and any? neighbors with [EC
= currentEC]]
    let neighboringCells ([EC] of contacts)
360     set neighboringCells remove-duplicates neighboringCells ;make a list of ECs that
are in contact with the current cell

    let currentDLL4-Input (list 0)

365     foreach neighboringCells[
      set currentDLL4-Input lput [DLL4] of one-of patches with [EC = ?] currentDLL4-
Input
    ]
    set currentDLL4-Input sum currentDLL4-Input
370     ask patches with [EC = currentEC][
      set DLL4-Input currentDLL4-Input
    ]

  ]
375   foreach listOfECs[
    let DLL4-Input* [DLL4-Input] of one-of patches with [EC = ?]
    let Notch* [Notch] of one-of patches with [EC = ?]

    set Notch* (DLL4-Input* * ALPHA - (Notch* * .4))
380     ;Previously used NOTCH-ODE to determine new Notch. Now use a simpler transfer
function that is linearly dependent on alpha.

```

```

    let DLL4* [DLL4] of one-of patches with [EC = ?] ;* gets the current DLL4 state of
the cell
385   let VEGF_VEGFR2* sum [VEGF_VEGFR2] of patches with [EC = ?] ;* is the cumulative
VEGF_VEGFR2 signal

    set DLL4* DLL4* + VEGF_VEGFR2* - (DLL4* * .4); DLL4 is degraded by 10% of its
current value, while adding an amount based VEGF_VEGFR2
390

    ;Previously used Delta-ODE to determine new DLL4 state.
ask patches with [EC = ?][
    ;Set the amount of NOTCH and DLL4 signal in the cells
    set NOTCH NOTCH*
395    set DLL4 DLL4*

]
ask one-of patches with [EC = ?][
    set listOfNotchLevels lput (sum [NOTCH] of patches with [EC = ?])
400 listOfNotchLevels
    set listOfPhosphoR2 lput (sum [VEGF_VEGFR2] of patches with [EC = ?])
listofPhosphoR2
    set listOfDLL4Levels lput (sum [DLL4] of patches with [EC = ?]) listOfDLL4Levels
    set VEGFR2list lput (sum [VEGFR2] of patches with [EC = ?]) VEGFR2list
405    set VEGF_VEGFR1list lput (sum [VEGF_VEGFR1] of patches with [EC = ?])
VEGF_VEGFR1list
]
]

410 foreach listOfECs [
    ask one-of patches with [EC = ?][
        ifelse (sum [VEGF_VEGFR2] of patches with [EC = ?]) > Beta
        [ask patches with [EC = ? ][set tipCell 1]]
        [ask patches with [EC = ? ][set tipCell 0]]
415    ]
]
end

to-report NOTCH-ODE [NOTCHin DLL4in]
420   let kDLL4 .1
   let kNOTCH .1
   let kdegNOTCH .1
   let maxNOTCH 1e-14
   if NOTCHin > maxNotch [set NOTCHin maxNotch]
425

   let dNOTCH ((1 - NOTCHin / maxNOTCH) * kDLL4 * DLL4in - kdegNOTCH * NOTCHin)
   report (NOTCHin + dNOTCH)
end

430 to-report Delta-ODE [DLL4in pR2in]
   let kDLL4 .1
   let kR2 .1
   let kdegDLL4 .1
   let maxDLL4 1e-14
435

   if DLL4in > maxDLL4 [set DLL4in maxDLL4]

   let dDLL4 ((1 - DLL4in / maxDLL4) * kR2 * pR2in - kdegDLL4 * DLL4in)
440   report (DLL4in + dDLL4)
end

to changeViewMode [viewMode]
445   if viewMode = "ECs"
   [
       foreach listOfECs
       [

```

```

    ask patches with [EC = ?][set pcolor originalColor]
  ]
450  foreach listofPCs
    [
      ask patches with [PC = ?][set pcolor originalColor]
    ]
  ]
455  ]
  if viewMode = "DLL4"
  [ifelse max [DLL4] of patches > 0
    [let big max [DLL4] of patches ask patches [set pcolor scale-color red DLL4 0
big]]]
460  [ask patches [set pcolor black]]
  ]
  if viewMode = "Notch"
  [ifelse max [NOTCH] of patches > 0
    [let big max [NOTCH] of patches ask patches [set pcolor scale-color red NOTCH 0
465  big]]]
  [ask patches [set pcolor black]]
  ]
  if viewMode = "VEGF_VEGFR2"
  [ifelse max [VEGF_VEGFR2] of patches > 0
470  [let big max [VEGF_VEGFR2] of patches ask patches [set pcolor scale-color red
VEGF_VEGFR2 0 big]]]
  [ask patches [set pcolor black]]
  ]
  if viewMode = "R2production"
475  [ifelse max [VEGFR2-production] of patches > 0
    [let big max [VEGFR2-production] of patches ask patches [set pcolor scale-color
red VEGFR2-production 0 big]]]
  [ask patches [set pcolor black]]
  ]
480  ]
end

to-report objects? [PCid]
  let Ex 0
485  let In 0
  ask patches with [pxcor > min-pxcor and pycor > min-pycor][
    let cornerCount 0
    if [PC] of self = PCid [set cornerCount cornerCount + 1]
    if [PC] of patch-at 1 0 = PCid [set cornerCount cornerCount + 1]
490  if [PC] of patch-at 0 -1 = PCid [set cornerCount cornerCount + 1]
    if [PC] of patch-at 1 -1 = PCid [set cornerCount cornerCount + 1]

    if cornerCount = 3 [set Ex Ex + 1]
    if cornerCount = 1 [set In In + 1]
495  ]
  report abs (Ex - In) / 4
end

to swapPatches [origin destination]
500
  ask destination [
    set pcolor [pcolor] of origin
    set EC [EC] of origin
    set PC [PC] of origin
505  set DLL4 [DLL4] of origin
    set NOTCH [NOTCH] of origin
    set VEGF_VEGFR2 [VEGF_VEGFR2] of origin
    set VEGFR2 [VEGFR2] of origin
    set VEGFR1 [VEGFR1] of origin
510  set tipCell [tipCell] of origin
    set VEGFR2-production [VEGFR2-production] of origin
    set sVEGFR1-production [sVEGFR1-production] of origin

```

```

    set mVEGFR1-production [mVEGFR1-production] of origin
    set originalColor [originalColor] of origin
515   set VEGF_VEGFR1 [VEGF_VEGFR1] of origin
    set VEGF_VEGFR2 [VEGF_VEGFR2] of origin
  ]

  ask origin [
520     set pcolor scale-color green VEGF 0 maxVEGF
    set EC 0
    set PC 0
    set DLL4 0
525     set NOTCH 0
    set VEGF_VEGFR2 0
    set VEGFR2 0
    set VEGFR1 0
    set tipCell 0
    set VEGFR2-production 0
530     set sVEGFR1-production 0
    set mVEGFR1-production 0
    set originalColor 0
    set VEGF_VEGFR1 0
    set VEGF_VEGFR2 0
535   ]

end

540 to makeOutputFile
    let fileCounter 1
    let date date-and-time
    repeat 16 [set date remove-item 0 date]
    while [file-exists? (word "RetinaModel_" StartingCellLayout "_A" ALPHA "B" BETA "_")
545 filecounter]][set fileCounter fileCounter + 1]
    set outputFileName (word "RetinaModel_" StartingCellLayout "_A" ALPHA "B" BETA "_")
    filecounter)
    file-open outputFileName
    file-print "Step, TipCells, ECs, meanNotch, stdNotch, meanDLL4, stdDLL4"
550   file-close

end
to updateOutputFile
    file-open outputFileName
555   file-type word ticks ", "
    file-type word length listOfTipCells ", "
    file-type word length listOfECs ", "
    file-type word mean listOfNotchLevels ", "
    file-type word standard-deviation listOfNotchLevels ", "
560   file-type word mean listOfDll4Levels ", "
    file-print standard-deviation listOfDll4Levels
    file-close
end

565 to newReceptorBinding
    let kint 2.8e-4 ;internalization of VEGF Receptors
    let sR 100 * kint;insertion rate of VEGF Receptors, set to balance with kint for
    steady state of 100 VEGFR2 on a patch

570   ;NOTE: at "steady state" the insertion and internalization rates are equal. Notch
    activity will reduce the insertion rate of new receptors. VEGFR1 is assumed to be
    maintained as a steady state concentration.

575   let R2_kon 1e7
    let R2_koff 1e-3
    let R1_kon 3e7
    let R1_koff 1e-3

```

```

let sR1_kon 3e7
let sR1_koff 1e-3
580

let C (6.022e23 * 2.5e-15) ; converts pM to molecules

585 ask patches with [EC != 0 and VEGF >= 2 and (VEGFR2 > 0 or VEGF_VEGFR2 > 0)][
  let ronR2 (R2_kon / C) * VEGF * VEGFR2
  let ronR1 (R1_kon / C) * VEGF * VEGFR1

  let roffr2 R2_koff * VEGF_VEGFR2
590 let roffr1 R1_koff * VEGF_VEGFR1

  let dt (1 / (ronR2 + roffr2) * log (1 / random-float 1) 10) ;time step in seconds

595 repeat (20)[ ;Assume a 10 minute time step

  let p random-float 1

  let Pr2 ronR2 / (ronR2 + roffr2)
600 let Pr1 ronR1 / (ronR1 + roffr1)

  if p <= Pr2 and p > Pr1 and VEGFR2 > 0 and VEGF_VEGFR1 > 0[
    set VEGFR2 VEGFR2 - 1
    set VEGF_VEGFR2 VEGF_VEGFR2 + 1
605
    set VEGFR1 VEGFR1 + 1
    set VEGF_VEGFR1 VEGF_VEGFR1 - 1
  ]

610 if p <= Pr1 and p > Pr2 and VEGF_VEGFR2 > 0 and VEGFR1 > 0 [
  set VEGFR2 VEGFR2 + 1
  set VEGF_VEGFR2 VEGF_VEGFR2 - 1

  set VEGFR1 VEGFR1 - 1
615 set VEGF_VEGFR1 VEGF_VEGFR1 + 1
]

if p <= Pr2 and p <= Pr1 and VEGFR2 > 0 and VEGFR1 > 0 and VEGF >= 2[
620 set VEGF VEGF - 2

  set VEGFR2 VEGFR2 - 1
  set VEGF_VEGFR2 VEGF_VEGFR2 + 1

  set VEGFR1 VEGFR1 - 1
625 set VEGF_VEGFR1 VEGF_VEGFR1 + 1
]

if p > Pr1 and p > Pr2 and VEGF_VEGFR2 > 0 and VEGF_VEGFR1 > 0[
630 set VEGF VEGF + 2

  set VEGFR2 VEGFR2 + 1
  set VEGF_VEGFR2 VEGF_VEGFR2 - 1

  set VEGFR1 VEGFR1 + 1
635 set VEGF_VEGFR1 VEGF_VEGFR1 - 1
]
]
]

640 ;Now, either add or subtract 1 VEGFR2 from each patch
ask patches with [EC != 0][
  let rinsert sR

```

```

        if Notch > 0 [set rinsert (sR - sR * Notch / [Notch] of max-one-of patches
645 [Notch])]
        let rintern (kint) * (VEGFR2 + VEGF_VEGFR2)

        ;let dt (1 / (rinsert + rintern) * log (1 / random-float 1) 10) ;time step in
seconds
650
        repeat 10[
            ifelse rinsert = 0 [set Pinsert 0][set Pinsert rinsert / (rinsert + rintern)]

655
            let p random-float 1

            ;if removing receptors, equal chance to remove bound or unbound, unless there are
none to remove
660
            if p <= Pinsert [
                let p2 random-float 1

                if VEGFR2 = 0 and VEGF_VEGFR2 >= 5 [set VEGF_VEGFR2 VEGF_VEGFR2 - 5]
665
                if VEGF_VEGFR2 = 0 and VEGFR2 >= 5 [set VEGFR2 VEGFR2 - 5]

                if VEGFR2 >= 5 and VEGF_VEGFR2 >= 5[
                    ifelse p2 <= 0.5 [set VEGFR2 VEGFR2 - 5][set VEGF_VEGFR2 VEGF_VEGFR2 - 5]
670
                ]
            ]

            if p > Pinsert [
675
                set VEGFR2 VEGFR2 + 5
            ]
        ]
    end

680
to exportImages
    let ImageFileName outputFileName
    let big max [VEGF_VEGFR2] of patches ask patches [set pcolor scale-color red
VEGF_VEGFR2 0 big]
685
    export-view (word ImageFileName "_pVR2image.png")
    set big max [VEGF] of patches ask patches [set pcolor scale-color red VEGF 0 big]
    export-view (word ImageFileName "_VEGFimage.png")
    set big max [DLL4] of patches ask patches [set pcolor scale-color red DLL4 0 big]
    export-view (word ImageFileName "_DLL4image.png")
690
    set big max [NOTCH] of patches ask patches [set pcolor scale-color red NOTCH 0 big]
    export-view (word ImageFileName "_NOTCHimage.png")
    ask patches [set pcolor scale-color green VEGF 0 maxVEGF]
    foreach listofECs [ask patches with [EC = ?][set pcolor originalColor]]
    foreach listofPCs [ask patches with [PC = ?][set pcolor originalColor]]
695
    export-view (word ImageFileName "_Cellimage.png")
    ask patches [set pcolor black]
    foreach listofECs [ask patches with [EC = ?][set pcolor blue]]
end

```